POLITECNICO DI TORINO

Master of science in Mechatronic Engineering

Master Degree Thesis

Modelling of mobile vehicles for simulation and control

Supervisor
Prof. Marina Indri

Candidate
Dario Pasini

Supervisor at COMAU S.p.A.
Ing. Ivan Lazzero

December 2019

Contents

Chapter 1

Introduction

This thesis starts from a project of COMAU S.p.a., whose goal is the realization of a differential drive wheeled mobile robot for industrial application. The robot purpose is the material handling in industrial environments and warehouses and it is able to move around on its own without the need of onboard operator or driver. These robots are called Automated Guided Vehicles and are becoming very popular in the branch of collaborative robots. Indeed, they can work autonomously with human operators since they are aware of the surrounding environment. They are able to detect obstacles and to avoid collisions, using systems like laser scanners. These robots allow also to improve the modularity of industrial productions. Indeed, they can move products from one working station to another one to perform subsequent processing. In this way, the same station can be used for different products and the production lines can be changed just changing the robot paths. The name of the new wheeled mobile robot of COMAU S.p.a is Agilino and in this thesis its dynamic model is developed. Dynamic models are fundamental in all the robot design phases. Both mechanical and control software design phases need a model to proceed. Of course different design goals need different models to be used. The last statement lays on the awareness that a general model including all the robot dynamical aspects can be difficult to realize and also useless with respect to the effort needed to find it. Of course, more general the model is, better it is but also more complex. Therefore, some dynamical aspects are usually simplified or neglected depending on the model purpose.
In this thesis three models for three different purposes are investigated:

1. The first model goal is to be as general as possible in order to be used instead of the real wheeled mobile robot until the first prototype is built. To take into account many dynamical aspects in an easy and intuitive way, the multi body programme Adams was chosen to develop this model. The following two mathematical models will be refined using this first one as the reference.

2. The second model is less general than the previous one, because it is built

computing the robot dynamic equations. It is needed to translate into mathematical equations the first model results in order to get a better understanding of the robot. It will be used in the motors choice and to plan safe trajectories for the robot. Safe trajectories stand for trajectories where the non-sliding and non-slipping constraints are respected at the robot driving wheels.

3. The third and last model is a mathematical model as the second one but simpler, since its purpose is to be used as the basis for the design of a control algorithm to drive the motors. All the dynamical aspects that will be neglected will be considered as disturbances and the control algorithm should be robust enough to deal with them.

Therefore, the final thesis purpose is to control the robot motion so that it follows the desired trajectories. The control of the robot motion can be divided into two actions. The first action follows the common sense rule that prevention is better than cure. Indeed, it consists in finding the velocity and acceleration limits of the trajectories to avoid both the longitudinal slip and the lateral slide. This action is performed offline, so that the controller will never provide a trajectory that for sure cannot be travelled by the robot. These limits can be be found both when the robot is travelling on its own and when it is pulling a library. The second action is the online control of the robot driving motors. The robot trajectory is described by the time evolution of the motor shafts angular velocities. The controller compares the ideal angular velocities with the ones measured by the encoders at the motors shaft and tries to let the error between them converge to zero as quick as possible. The controller action is fundamental to make the robot follow the desired trajectory, taking care also of the unexpected situations, as the possible reduction of the friction coefficient at the wheel-ground contact point. In these cases, the controller recovers the longitudinal slip or lateral slide that occur due to events that are not predictable a priori.

This thesis starts with the introduction of the Automated Guided Vehicle world in Chapter 2. The main AGV categories used at this moment are described and examples of existing robots are given. The Agilino robot is introduced and the category it belongs to, which is the one of differential drive robots, is compared to the other categories with respect to its working goals. Chapter 2 ends with the description of differential drive robot kinematic model. Then, in Chapter 3, the first robot model on the multi body programme Adams is built. In Chapter 4, the relevant dynamic aspects of the robot are analysed and the robot mathematical model for safe trajectories computation is developed. The robot task is to pull tracks, therefore also a track model is developed. In this way, safe trajectories with the maximum payloads can be investigated. In Chapter 5, the Adams model and the mathematical model are simulated together to make a comparison that allows to tune the mathematical model parameters. In Chapter 6, the mathematical model results are compared with the measures taken on the real prototype. In Chapter

7, the third and last model is developed. It is a simpler mathematical model whose purpose is the design of the control algorithm that drives the two motors. A decentralized control strategy is implemented and tested with the Adams model. In Chapter 8, future works that will evolve from this thesis are presented.

Chapter 2

State of the art

A general definition for the Automated Guided Vehicles is the following:
An Automated Guided Vehicle is a wheeled mobile robot able to move materials in a facility without the need of an onboard operator or driver. This general definition allows to categorize the AGVs from two different points of view. The first one is the wheel configuration, while the second one refers to the technological solutions used by the robot to move autonomously.

2.1 Wheels' types

Before analysing the wheel configurations, different types of wheels have to be presented. There are two main wheels' groups, the first one including omni-wheels and mecanum wheels and the second one including the conventional wheels. An omni wheel (Figure 2.1a) has small rollers on its circumference whose axes are perpendicular to the wheel plane. Also a mecanum wheel (Figure 2.1b) has small rollers around its circumference, but the rollers axes form an angle of 45° with respect to the wheel plane. Conventional wheels can be divided into fixed wheels and orientable wheels. A fixed wheel can rotate only around its main axis that is perpendicular to the wheel plane and passes through the wheel centre. Instead, an orientable wheel can rotate around both the main axis and a secondary axis that is perpendicular to the main one. In centred orientable wheel the secondary axis passes through the wheel centre, while in off-centred orientable wheel does not. The off-centred wheels with the secondary axis on the wheel plane are called castor wheels (Figure 2.1c). They can be actuated or not since they are self-aligning due to the distance between the secondary axis and the wheel centre. Instead centred wheels are always actuated. In order to reduce the friction torque opposition to their orientation, centred wheels can be substituted with wheels having the secondary axis not in the wheel plane.

(a) *Omni wheel [1]*

(b) *Mecanum wheel [2]*

(c) *Castor wheel [3]*

Figure 2.1: Wheels' types

2.2 Kinematic parameters

As described in paper [4], depending on the number and types of wheels used in the configuration, the motion capabilities of a wheeled mobile robot change and can be described by three parameters called degree of mobility δ_m, degree of steer-ability δ_S and degree of manoeuvrability δ_M [1].

The three parameters are analysed assuming that the robot motion is planar and that the wheels are rigid. Due to these assumptions, the wheel plane is always perpendicular to the ground, having the main axis horizontal and the secondary axis, if present, vertical. In addition the contact between each wheel and the ground reduces to a point. In a planar motion, the robot posture is described by three Cartesian coordinates $\xi = [x, y, \theta]$, where x and y describe the position of the robot local frame origin in the inertial frame and θ the robot orientation with respect to the inertial frame z axis.

Depending on the wheel configuration, the three posture coordinates can be varied independently one with respect to the others or not. The posture variation from a fixed initial state is described by the posture velocity $\dot{\xi} = [\dot{x}, \dot{y}, \omega]$. Most robots are not capable of controlling these three posture coordinates independently due to the presence of non-holonomic constraints at the wheels contact points.

Conventional wheels are subject to the kinematic constraints that impose null velocity with respect to the ground to each wheel contact point. Contact point velocity can be decomposed into two components called lateral and longitudinal velocities. Lateral velocity is perpendicular to the wheel plane while the longitudinal one is parallel. Zero lateral velocity guarantees no wheel lateral slide, while zero longitudinal velocity no longitudinal slip. Omni wheels and mecanum wheels have only one component of the contact point velocity that must be zero and it is the one on the direction parallel to the axis of the roller that is in contact with the ground.

Due to the planar motion assumption, the robot motion can be described at each instant as a rotation around an instantaneous centre of rotation (ICR). If the ICR goes to infinity, it means that the robot is just translating without rotating. Not to violate the lateral slide constraint of a fixed or centred orientable wheel, the ICR has to belong to the primary axis of that wheel. Castor wheels are not mentioned since they are self-aligning, orienting themselves with their axes passing through the ICR defined by the other wheels. So at each instant, the axes of the fixed and centred wheels have to intersect in the same point that is the ICR, as shown in Figure 2.2.

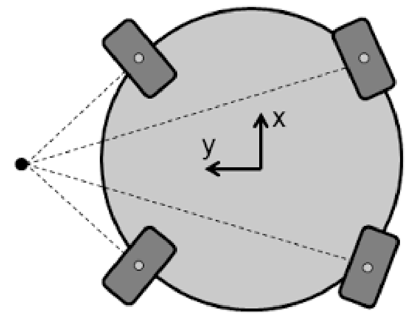

Figure 2.2: Image from [5]

The degree of mobility δ_m corresponds to the degree of the plane subspace plus one, where it is possible to move the ICR instantaneously without steering the centred wheels. Practically, it corresponds to the number of wheels whose angular velocities can be set independently.

- When $\delta_m = 1$, the ICR position cannot be changed instantaneously.
- When $\delta_m = 2$, the ICR can be moved instantaneously along an axis.
- When $\delta_m = 3$, the ICR can be placed instantaneously wherever in the plane. This means that neither fixed nor centred wheels are present in the wheel configuration.

The degree of steer-ability δ_S corresponds to the number of centred wheels whose orientations can be changed independently from one another to fix the position of the ICR in the plane. If more centred wheels than δ_S are present, their main axes have to pass at each instant through the ICR.

- When $\delta_S = 0$, no centred wheels are present in the wheel configuration.
- When $\delta_S = 1$, one centred wheel can be independently orientated.
- When $\delta_S = 2$, two centred wheels can be independently orientated.

At the end, the degree of manoeuvrability $\delta_M = \delta_m + \delta_S$ is a synthesis between the previous two parameters. It corresponds to the total number of degrees of freedom (DOFs) that can be controlled independently in the robot.

- When $\delta_M = 2$, the robot has two independent degrees of freedom.
- When $\delta_M = 3$, the robot has three independent degrees of freedom therefore the ICR can be placed wherever in the plane.

2.3 AGV kinematic analysis

Based on this three parameters that come out from a kinematic discussion, the main groups of AGVs are listed in the following.

1. Omni-directional robots,
   (a) with omni or mecanum wheels, or
   (b) with active steerable wheels,
2. Synchronous drive robots,
3. Differential drive robots,
4. Car-like robots.

All the omnidirectional robots are characterized by $\delta_M = 3$ since at each instant they can move the ICR wherever in the plane. These robots can change the three posture coordinates $\xi = [x, y, \theta]$ independently from one another.

The first omni-directional robots analysed are equipped with omni wheels or mecanum wheels. The wheels displacement depend on the wheel type used.
With omni-wheels, two main configurations are used. The first one in Figure 2.3a has three wheels while the second one in Figure 2.3b has four. In both cases, each omni-wheel is mounted with its main axis passing through the robot centre and at the same distance from the robot centre. The wheels are shifted with an angular displacement of 120° in the three wheels robot and 90° in the four wheels one. With mecanum wheels, again two four wheel configurations are used. In both cases, the wheels are displaced at the vertices of a rectangle and have parallel planes. The two configurations are defined X and O, depending on the direction of the wheels rollers

in contact with the ground. The X one can be seen in Figure 2.4. The maximum manoeuvrability $\delta_M = 3$ is obtained with $\delta_m = 3$ and $\delta_S = 0$. This means that at each instant the ICR can be placed instantaneously wherever in the plane by acting on the wheels angular velocities.

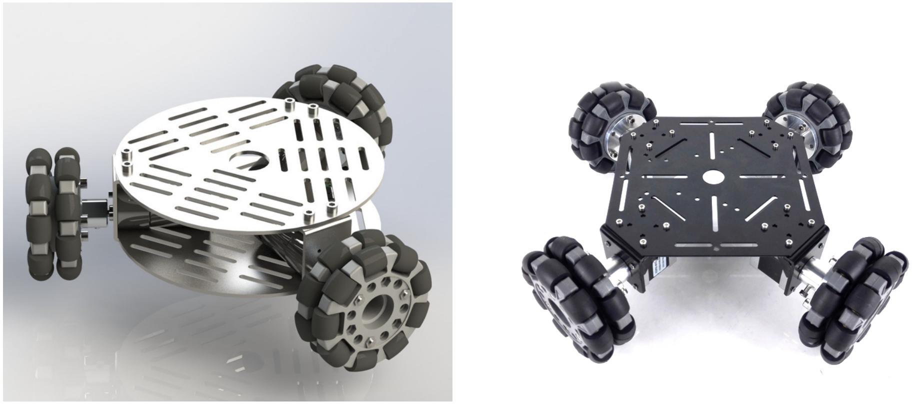

(a) *Three omni wheels robot from [6]* (b) *Four omni wheels robot from [7]*

Figure 2.3: Omni wheels robots

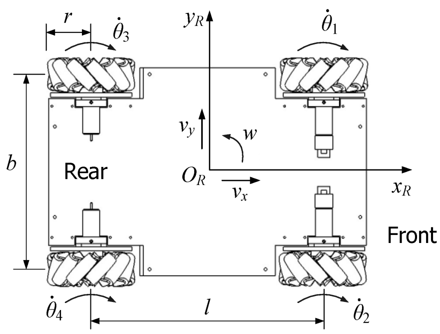

Figure 2.4: Mecanum wheels robot from [8]

The second omnidirectional robots analysed are equipped with active steerable wheels. These robots have no fixed wheels and at least two active orientable wheels. If more than two orientable wheels are present, two are oriented independently to fix ICR position wherever in the plane, while the other ones have to be oriented so that the main axes passes through the fixed ICR. The maximum manoeuvrability $\delta_M = 3$ is obtained with $\delta_m = 1$ and $\delta_S = 2$. Therefore, the ICR can be placed wherever in the plane but not instantaneously since re-orientation of orientable wheels has to be performed. The three independent controllable DOFs are the orientation angles of two orientable wheels and the angular velocity of one of them. The most common configurations are two. The first one has two front active orientable centred wheels and one rear self-aligning castor wheel. The second one has four active orientable centred wheels, two independent and two dependent displaced in rectangular form.

Differential drive robots, synchronous drive robots and car-like robots are characterized by $\delta_M = 2$ since only two posture coordinates can be controlled independently at each instant.

Differential drive robots have a wheel configuration made of at least two fixed wheels having the same main axis and no centred wheels. The most used configurations are two. The first one has two front fixed wheels and one rear castor wheel, while the second one two rear fixed wheels and one front castor wheel. The manoeuvrability $\delta_M = 2$ is obtained with $\delta_m = 2$ and $\delta_S = 0$. The ICR position can be changed instantaneously on the main axis of the fixed wheels. The two independent controllable DOFs are the angular velocities of two fixed wheels. If a configuration with more than two fixed wheels is needed, the additional fixed wheels must have the same main axis of the first two and their angular velocities depend on the ICR position. $\delta_m = 2$ results from the fact that the robot velocity component on the wheels main axis is always zero, therefore the lateral movement is not possible.

Car-like robots have a wheel configuration made of one or more fixed wheels having the same main axis and at least one centred wheel not belonging to the main axis of the fixed wheels. The simplest configuration is the one with two rear fixed wheels and one front centred wheel, while the most used has two front orientable wheels instead of one. The manoeuvrability $\delta_M = 2$ is obtained with $\delta_m = 1$ and $\delta_S = 1$. The ICR position can be changed on the main axis of fixed wheels varying the orientation of the centred wheels. They have the same manoeuvrability of differential drive robots but the ICR is not changed instantaneously because re-orientation of orientable wheels must be performed. The two independent controllable DOFs are the orientation angle of one orientable wheel and the angular velocity of one wheel. The angular velocities of the other wheels depend on the ICR position. With two or more orientable wheels, one fixes the position of the ICR while the others must be oriented so that their axes passes though the ICR.

Synchronous drive robots have a wheel configuration made of only orientable wheels. The most common configuration is the one with three orientable wheels placed at the vertices of an equilateral triangle. The manoeuvrability $\delta_M = 2$ is obtained with $\delta_m = 1$ and $\delta_S = 1$ as for car-like robots. One wheel is oriented independently ($\delta_S = 1$), while the others are oriented so that their axes are parallel to the independent wheel axis. In this way the ICR goes to infinity and the robot can only translate in the direction of the wheels. Even though the same parameters characterize car-like and synchronous robots, a huge difference is present. In car-like robots the null velocity component of the robot is the one along the direction between the robot centre and the ICR. In synchronous robots, the null velocity component of the robot is its angular velocity, since the robot orientation cannot be changed.

2.4 AGV purpose analysis

This comparison between the different groups of wheeled mobile robots is made only from a kinematic point of view and returns the mobility capabilities of the robots. Dynamical aspects concerning masses, inertias, forces and torques must be taken into account in order to choose the best robot configuration for the desired purposes. The AGV needed must be able to pull trucks and libraries and it has to be as compact as possible. Therefore, the robot should have a low number of motors for a compact form, good traction capabilities to pull tracks and libraries, systems that guarantee always the contact between the traction wheels and the ground, the maximum degree of manoeuvrability that the previous points allow. Good traction capabilities means that the wheel configuration must have as much as traction motors inside its wheel configuration. Motors can be divided depending on their use into traction motors in charge of traction wheels rotation and orientation motors that change the orientation angles of orientable wheels. It would be better to have a configuration with maximum three traction wheels, indeed if more than three actuated wheels have to be in contact with the ground, technological solutions such as shock absorbers or more deformable wheels have to be considered. This would oppose the simplicity and compact structure goals. The absence of these solutions limits the robot work in flat ground. This is acceptable since these robots are going to work in factories or warehouses.
Now a brief analysis of the wheel configuration previously mentioned is carried out.

1. Three omni-wheel robot.
   The three posture coordinates $\xi = [x, y, \theta]$ can be varied independently by acting on the three controllable DOFs $[\dot{\phi}_1, \dot{\phi}_2, \dot{\phi}_3]$ representing the wheels' angular velocities. This robot is not redundant, needs three traction motors and has good traction capabilities. Two considerations have to be done:
   - The omni wheel structure allows to fully exploit the motor torque applied to the wheel, indeed the omni wheel rollers axes are perpendicular to the wheel main axis and lay in the wheel plane. An actuated omni wheel can exert its traction force only along the direction of the rollers' axes. Therefore, since the applied torque is perpendicular to the rollers' axes, it is completely translated into the traction force at the wheel-ground contact point. For this reason, omni wheels behave as conventional wheels from this point of view.
   - Despite the good traction capabilities, a part of the traction force is wasted in robot translation. The three traction forces are shifted of

120/60° therefore the force components perpendicular to the translation direction cancel each other out.

Three wheels allow in first approximation not to use shock absorbers on a flat ground since three points define precisely a plane.

2. Four omni-wheel robot.
The three posture coordinates $\xi = [x, y, \theta]$ can be varied independently by acting on the four controllable DOFs $[\dot{\phi}_1, \dot{\phi}_2, \dot{\phi}_3, \dot{\phi}_4]$ representing the wheels' angular velocities. This robot is redundant, needs four traction motors for the four wheels and has good traction capabilities. Again the omni wheel structure allows to fully exploit the torque applied to each wheel but an improvement is present with respect to the previous case. Indeed, the robot does not waste part of the total traction force during neither translation nor rotation. Due to the wheels' angular shift of 90°, the opposite wheels have the same main axis and therefore parallel traction forces. Therefore, the two couples of opposite wheels have perpendicular traction directions that allow to built easily the total traction force that must be applied to the robot. If a pure translation is required without changing the robot orientation, each wheel of one couple provides half of the corresponding force component. Shock absorbers could be needed to assure the contact of all four wheels with the ground even though it is flat.
3. Four mecanum-wheel robot.
The three posture coordinates $\xi = [x, y, \theta]$ can be varied independently by acting on the four controllable DOFs $[\dot{\phi}_1, \dot{\phi}_2, \dot{\phi}_3, \dot{\phi}_4]$ representing the wheels' angular velocities. As the previous one, also this robot is redundant and needs four traction motors for the four wheels. It has good traction capabilities but two negative aspects have to be considered:

   - First, the mecanum wheel structure does not allow to fully exploit the torque applied to each wheel. Indeed, mecanum wheel rollers have the axes tangent to the wheel circumference but at 45° with respect to the wheel main axis. For this reason, since only the torque component perpendicular to the rollers axes is translated into traction force, the torque component parallel to the rollers axes results into the rollers rotation. Therefore, not all the wheel torque is exploited to move the robot and the wheel rollers always rotate.
   - A part of the traction force of each wheel is wasted in both translation and rotation. Considering for example the longitudinal translation, the traction forces components perpendicular to the desired robot motion direction cancel each other out.

   Shock absorbers are needed to assure that all the four actuated wheels are in contact with the flat floor.
4. Four active orientable wheels.

The three posture coordinates $\xi = [x, y, \theta]$ can be varied independently by acting on the eight controllable DOFs that are the four angular velocities $[\dot{\phi}_1, \dot{\phi}_2, \dot{\phi}_3, \dot{\phi}_4]$ and the four orientation angles $[\psi_1, \psi_2, \psi_3, \psi_4]$. Only two orientation angles and one angular velocity are independently tunable and therefore the robot is redundant. It uses an orientation motor and a traction motor for each wheel therefore eight total motors are needed. It has great traction capabilities due to the presence of four traction motors and due to the use of conventional wheels that allow to fully exploit the applied torques and that have a larger contact area than omni and mecanum wheels. Also in this case, shock absorbers are needed.

5. Car-like robot with two front orientable wheels and two rear fixed wheels.
   It has two independent DOFs therefore the three posture coordinates $\xi = [x, y, \theta]$ cannot be varied independently. The controllable DOFs are the two orientation angles $[\psi_1, \psi_2]$ and the four angular velocities $[\dot{\phi}_1, \dot{\phi}_2, \dot{\phi}_3, \dot{\phi}_4]$. Only one orientation angle and one angular velocity are independently tunable. In this robot, an orientation motor and a traction motor are present for each orientable wheel. The two rear fixed wheels just provide the vehicle weight stabilization. It has good traction capabilities and shock absorbers are needed.
6. Three wheels synchronous drive robot.
   It has two independent DOFs but six controllable DOFs that are the three orientation angles $[\psi_1, \psi_2, \psi_2]$ and three angular velocities $[\dot{\phi}_1, \dot{\phi}_2, \dot{\phi}_3]$. As for car-like robots only one orientation angle and one angular velocity are independently tunable. The orientation angles have to be fixed so that the three wheels have parallel directions. It has one traction motor for each wheel and usually only one orientation motor that drives all the three orientation angles with a mechanical transmission. It has good traction capabilities and shock absorbers are not needed in first approximation on a flat ground.
7. Differential drive robot with two fixed wheels and one castor wheel.
   It has two independent DOFs and two controllable DOFs that are the two fixed wheels' angular velocities $[\dot{\phi}_1, \dot{\phi}_2]$. It is a not redundant configuration and requires only two traction motors to move. It has good traction capabilities and shock absorbers can be avoided in first approximation for flat ground work.

2.5 AGV comparison

The groups characterized by only two DOFs are differential drive robots, synchronous drive robots and car like robots. The simplest and potentially most compact configuration among them is the differential drive one, indeed it requires only two traction motors and does not need shock absorbers to work on flat ground.

The other two configurations requires four motors and the synchronous one must be provided with a mechanical transmission to orientate the three orientable wheels with just one motor.

Comparing the differential drive robot with the omni-directional robots having omni or mecanum wheels, from the traction capabilities point of view the conventional wheels are more performant than the omni and mecanum ones, due to the wider area of contact. As explained before, in three omni wheels robots and four mecanum wheels robots, part of the traction force is wasted, while in differential drive and four omni wheels ones it is fully exploited. Four omni wheel robot has four traction motors while the differential drive one has only two and does not need shock absorbers. Again the differential drive robot can be potentially the most compact and exploits the whole driving torques and traction forces even though it has one DOF less.

Considering the four steerable wheels robot, it is less compact than the differential drive one since it requires eight motors. With four traction motors it has great traction capabilities but requires shock absorbers. If the robot has to pull heavy trucks, it must be able to exert high traction forces. To apply a high traction force at each wheel-ground contact point without running into the slipping phenomena, the maximum static friction force between the wheel and the ground must be high enough. Therefore, the normal reaction force at the wheel contact point must be high. But in four orientable wheels robots, the traction wheels are also steering wheels, therefore a high normal force results into a higher vertical friction torque that opposes the wheel re-orientation. It follows that a stronger orientation motor must be used. It's clear that the orientation task would prefer a not too high weight on the wheel, while the traction task the opposite. A compromise has to be researched.

2.6 Agilino robot

Agilino is a differential drive robot. It has two central driving wheels and four castor wheels, two castor wheels in the front and two in the back. In this way, Agilino is a mix of the front castor wheel configuration with the rear castor wheel one. Agilino tries to cancel the two following configurations' problems.

1. In front castor wheel configuration, during longitudinal acceleration phases the contact normal force of the ground on the castor wheel reduces for two main reasons. The first one is due to the motors reaction torques on the robot base that try to make the robot base rotate in the opposite direction of the wheels. The second reason is due to the position of the robot mass centre that is situated at a vertical distance from the ground greater than the

driving wheels axis one. Indeed, this fact results into a moment of the inertial force that lights the front castor wheel. Not to loose the front castor wheel contact with the ground, in the mechanical design phases two precautions can be taken. First, the castor wheel can be placed not too close to the main axis of the two driving wheels. Second, the mass centre of the robot can be placed closer to the castor wheel. In this way, the longitudinal distance of the mass centre from the main axis is the arm of the weight force momentum that opposes the lightening of the front castor. If the castor wheel looses contact with the ground, the robot can capsize. Even though the previous case does not occur, when the acceleration phase finishes, the castor wheel impacts the ground causing undesirable motions.

2. In rear castor wheel configuration, the same problem occurs but during the deceleration phase. This configuration is better than the previous one since the castor wheel is pulled instead of being pushed.
3. The fact that the robot mass centre cannot be placed on the driving wheels but has to be moved toward the front or rear castor wheel has two bad consequences.
   (a) The first is that more far is the mass centre from the main axis, lower is the weight force on the driving wheels and therefore lower is the maximum traction force that each wheel can exert before slippage occurs.
   (b) The traction forces have to participate actively to oppose the non null momentum of the centrifugal force. Instead, if the mass centre is placed on the driving axis, that momentum is null.

Agilino mechanical design wants to maximize the traction forces that can be exerted before slippage occurs by placing the robot mass centre ideally on the driving axis, practically close to it. To do this, at least two castor wheels have to be used one in the front and one in the back. In this way, during the acceleration phases the motors reaction torques are opposed by the rear wheel, while during deceleration phases by the front one. Three contact points with the ground are always guaranteed. Agilino uses four castor wheels just because on the longitudinal axis where they should have been placed, the laser scanner are mounted.

2.7 Differential drive robot kinematic model

The first model studied is the kinematic one, that is the easiest since it neglects the mass and inertia properties of the robot and the forces that cause the movement. This model requires the assumption of planar motion of the robot that can be described by the posture coordinates (q_1, q_2, q_3), where q_1 and q_2 describe the position of the robot in the plane while q_3 its orientation. The model requires the definition of two reference frames that are listed in the following.

- The inertial reference frame R_0, that is fixed in the plane where the robot moves.
- The robot reference frame R_1, that has the origin in the midpoint of the segment connecting the two wheels centres, the x axis on the robot longitudinal axis, the y axis on the driving wheels main axis and the z axis perpendicular with respect to the ground.

The position vector t_1^0 and the orientation matrix R_1^0 of the reference system R_1 with respect to R_0 are listed in (2.1).

$$t_1^0 = \begin{bmatrix} q_1 \\ q_2 \\ 0 \end{bmatrix} \qquad R_1^0 = \begin{bmatrix} \cos(q_3) & -\sin(q_3) & 0 \\ \sin(q_3) & \cos(q_3) & 0 \\ 0 & 0 & 1 \end{bmatrix} \tag{2.1}$$

The velocities of interest that the kinematic model links exploiting the non holonomic constraints equations are listed below.

- v_R is the translational longitudinal velocity of the right wheel.
- v_L is the translational longitudinal velocity of the left wheel.
- $\dot{\phi}_R$ is the angular velocity of the right wheel.
- $\dot{\phi}_L$ is the angular velocity of the left wheel.
- v is the translational longitudinal velocity of the whole robot.
- $\omega = \dot{q}_3$ is the robot orientation rate of change around the inertial frame z axis.

$$\begin{cases} v = \frac{v_R + v_L}{2} \\ \omega = \frac{v_R - v_L}{2L} \end{cases} \tag{2.2}$$

$$\begin{cases} v_R = r \cdot \dot{\phi}_R \\ v_S = r \cdot \dot{\phi}_S \end{cases} \tag{2.3}$$

$$\begin{cases} \dot{q}_1 \cdot \cos(q_3) + \dot{q}_2 \cdot \sin(q_3) + \dot{q}_3 \cdot L = \dot{\phi}_R \cdot r \\ \dot{q}_1 \cdot \cos(q_3) + \dot{q}_2 \cdot \sin(q_3) - \dot{q}_3 \cdot L = \dot{\phi}_L \cdot r \\ \dot{q}_2 \cdot \cos(q_3) - \dot{q}_1 \cdot \sin(q_3) = 0 \end{cases} \tag{2.4}$$

The equations (2.2) come out from trivial geometric considerations due to the existence of the instantaneous centre of rotation as it can be seen in Figure 2.5. The value L is the distance between the two wheels centres. Then, from the longitudinal non slip constraint, relations (2.3) between the wheels angular velocities and the wheels longitudinal velocities is found, where r is the wheel radius. The two non-holonomic constraints related to the longitudinal and the lateral slip for each wheel are listed in (2.4). The lateral constraints of the wheels are of course equal since the two wheels have the same main axis.

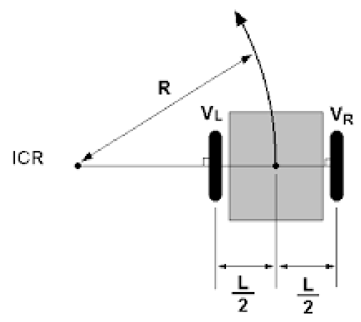

Figure 2.5: Differential drive robots instantaneous centre of rotation from [9]

The pure kinematic model is not sufficient when the robot can be subject to mass variations. For example when the robot is carrying a load both the inertia moments and the centre of mass position change. These variations can affect the traction properties causing the slippage of the wheels.

Chapter 3

Adams modelling

The first part of the work consists in looking for a computer programme that allows to create in an easy and intuitive way a general model, containing almost all the robot dynamical aspects, simplifying or neglecting as less as possible. This first model has to be as general as possible, because it will be used as a replica of the real robot until the first prototype is realized. It will be the reference for the next mathematical models that will be developed.

The chosen programme is Adams from MSC Software Corporation. It provides an intuitive graphic interface that allows the graphic construction of the robot model. The basic solid shapes are provided and the CAD files of the robot parts can be imported with their masses and inertias descriptions. Adams is chosen for two main reasons.

1. The first one is the mathematical model that allows to schematize the contact between bodies. This contact model returns the forces and torques exchanged and it is needed to describe the wheel-ground interaction.
2. The second reason is the friction mathematical model at the revolute joints.

To gain a deeper understanding of the programme, the theoretical study of the mathematical contact model and of the revolute joint friction model is performed. Then, some simulations with simpler systems than the whole robot are performed to understand how the models' parameters can be tuned.

3.1 Adams contact model

As explained in the Adams materials [10], the contact force is divided into two main components:

1. The normal reaction force F_n that is the force component perpendicular to the contact surface between the two bodies.

2. The friction force F_a that is the force component that lays on the contact surface.

The mathematical models that return the two contact force components are explained in the following once at a time.

3.1.1 Normal contact force

The function that describes the normal reaction force F_n is the impact function, based on the Contact Hertzian Theory. The normal force F_n is equivalent to the one returned by a non linear spring-damper system. The function has four tunable parameters that are the spring stiffness k, the non linear spring exponent e, the maximum damping coefficient $c_{\max}$ and the damping ramp-up distance d. Being q the distance between the two bodies, $\dot{q}$ the relative velocity between the two bodies and q_0 the minimum distance at which the interaction starts, the impact function (3.1) is reported below.

$$F_n = \begin{cases} k \cdot (q_0 - q)^e - c_{\max} \cdot \dot{q} * STEP\,(q, q_0 - d, 1, q_0, 0) & \text{se } q \leq q_0 \\ 0 & \text{se } q > q_0 \end{cases} \tag{3.1}$$

The spring is non-linear due to the presence of the exponent e and its force contribution is reported in (3.2).

$$F_{\text{spring}} = k \cdot (q_0 - q)^e = k_{\text{eq}} \cdot (q_0 - q) \tag{3.2}$$

Using an exponent value higher that 1, the spring equivalent stiffness k_{eq} increases exponentially with the penetration depth $p = (q_0 - q)$. Instead, the force contribution coming from the damper is reported in (3.3).

$$F_{\text{damper}} = -c_{\max} \cdot \dot{q} \cdot STEP\,(q, q_0 - d, 1, q_0, 0) \tag{3.3}$$

The usual damper force is $F_{\text{damper}} = -c_{\max} \cdot \dot{q}$ while the $STEP$ function is introduced not to have an instantaneous variation of the normal force when the impact occurs. Indeed the $STEP$ function changes smoothly between zero and one when the penetration depth $p = (q_0 - q)$ changes from zero to d, as shown in Figure 3.1.

Even though k, e and $c_{\max}$ depend on materials properties and contact geometry, the correlation with them is not straightforward, therefore a trial and error procedure is preferred to choose them. The damping ramp-up distance d is not a physical parameter. It is a mathematical trick not to have step variations of the normal force when an impact occurs. Before starting with the robot modelling, simulations of easier subsystems are performed in order to get familiar with these parameters that do not have precise physical meaning, since they summarize many aspects of the phenomena. The general guidelines for their tuning suggested by Adams [10] are listed below.

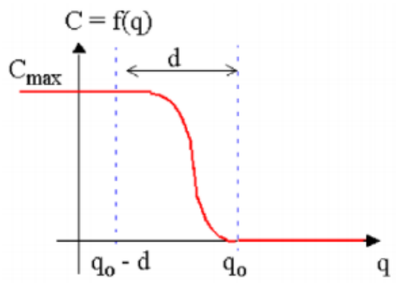

Figure 3.1: Image from [10]

- The spring stiffness k has to be high enough to prevent large penetration but not too high otherwise numerical problems can occur.
- The spring exponent e can be chosen equal to 1.1 for soft material as rubber.
- The maximum damping coefficient c_{max} should be set almost equal to one percent of the spring stiffness value.
- The damping ramp-up distance d must be chosen smaller than the desired penetration so that the damping coefficient can reach its maximum value c_{max}.

3.1.2 Contact friction force

The contact friction force uses the Coulomb approximation. The user has to fix the friction static coefficient, the friction dynamic coefficient, the stiction transition velocity and the friction transition velocity. The stiction transition velocity is the relative velocity between the two bodies that are in contact at which the friction coefficient is maximum and equal to the static one. Instead, the friction transition velocity is the relative velocity at which the friction becomes constant and equal to the dynamic one. Since the wheeled mobile robot usually works on industrial floors and their wheels have an external layer of polyurethane, the static coefficient is chosen equal to 0.6. The dynamic one is set equal to 0.01. The friction coefficient Coulomb approximation with respect to the relative velocity is shown in Figure 3.2b.

3.2 Adams joint friction model

Agilino has only revolute joints, one for each fixed wheel and two for each castor wheel. Adams allows to insert the friction effect at each revolute joint.
The formula used to compute the revolute joint friction torque T_{friction} is the following:

$$\begin{aligned} T_{\text{friction}} = &\mu \cdot [R_{\text{arm}} \cdot F_{\text{axialreaction}} + R_{\text{pin}} \cdot F_{\text{rotationalreaction}} + \\ &+ (R_{\text{pin}}/R_{\text{bending}}) \cdot T_{\text{bending}} + (1/\mu_s) \cdot T_{\text{preload}}] \end{aligned} \tag{3.4}$$

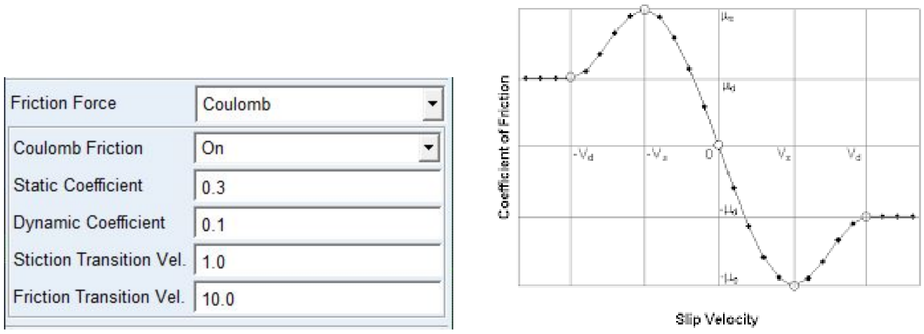

(a) *Friction parameters graphic interface* (b) *Coulomb friction curve*

Figure 3.2: Friction parameters. Images from [10].

The input forces that can be selected to compute the friction torque are the joint reaction forces that include the axial reaction force $F_{\text{axialreaction}}$ and the rotational reaction force $F_{\text{rotationalreaction}}$, then the bending moment T_{bending} and the torque preload T_{preload}. The torque preload allows to take into account the mechanical interference in the assembly of the joint. For Agilino model, only the joint reaction forces will be considered, therefore the interesting parameters are the friction arm R_{arm} and the pin radius R_{pin}. Adams allows also to set the maximum friction torque at the joint. Then, all the parameters needed by Adams to compute the effective friction coefficient μ have to be set. First, the user has to choose one of the three possible friction models. The first model includes both stiction and sliding effects while the other two only stiction effect or sliding effect. The parameters that must be set are listed in Table 3.1. The maximum stiction deformation is the maximum

Table 3.1: Revolute joint friction parameters

Parameters	Symbol	Unit measure
Static friction coefficient	μ_s	-
Dynamic friction coefficient	μ_d	-
Stiction transition velocity	v_s	cm/s
Transition velocity coefficient	m	-
Maximum stiction deformation	Δ_{max}	deg

angular displacement that can occur in a joint once the friction force enters the stiction regime.

3.3 Test simulations

As said before, some tests with simple subsystems are performed to check how parameters affect the different models analysed before. The goal is to check the contact forces exchanged between a wheel and a plane. This is the most important aspect, since it is the origin of the robot motion. In the student version of Adams it is possible to represent all the components as rigid bodies. The feature that allows to model them as flexible bodies is available but it was not used to model Agilino wheels, since in the list of materials the polyurethane was not present. Therefore, the wheel will be schematized with a cylinder having the radius equal to the real wheel radius. Since the robot motion can be approximated with a planar motion, the most relevant friction components exchanged between each wheel and the floor are the longitudinal friction force, the transversal friction force and the vertical friction torque. The longitudinal friction force is parallel to the wheel plane while the transversal friction force is perpendicular. The specific goal of the following tests is to check the dependency of each friction component on the contact parameters and on the wheel cylinder length. The parameters that will not change in the following preparatory tests are the ones related to the wheel physical description that are listed in Table 3.2. Approximating the wheel as a cylinder, moments of

Table 3.2: Wheel physical description values

Parameters	Symbol	Unit measure	Value
mass	M	Kg	10
radius	R	m	0.1
average width	h	m	0.04
axial inertia moment	I_a	$Kg \cdot m^2$	0.05
radial inertia moment	I_r	$Kg \cdot m^2$	0.026

inertia can be computed with (3.5) and (3.6), where the width average value h is equal to the cylinder length.

$$I_r = \frac{M \cdot (3R^2 + h^2)}{12} \tag{3.5}$$

$$I_a = \frac{M \cdot R^2}{2} \tag{3.6}$$

Vertical friction torque

The vertical friction torque exerted on the wheel is the first friction component to be investigated. The system is made of a wheel and a plane and it is shown in Figure 3.3. A cylindrical joint is used to limit the wheel motion allowing only rotation and translation along the vertical axis. The vertical translation must be free so that the wheel can penetrate the plane surface moving down under its weight. The penetration activates the spring-damper contact system that generates the normal reaction force. If it were zero also the contact friction force would be zero. The vertical rotation must be free because it is the movement that triggers the vertical friction torque. The other motions are constrained so that the wheel does not risk falling laterally while rotating. The wheel is schematized with a cylinder that has a rod coming out of it radially in the vertical direction. The rod is inserted just to apply the cylindrical joint. Indeed, the mass and inertia description of the wheel is not influenced by its presence. The wheel mass centre is still placed in the cylinder centre and the mass and moments of inertia are equal to the wheel's ones. The contact friction parameters are set equal to static friction $\mu_s = 0.7$, dynamic friction $\mu_d = 0.3$, stiction transition velocity $v_s = 0.1\ m/s$ and friction transition velocity $v_d = 0.01\ m/s$. The test consists in simulating the wheel behaviour when an initial

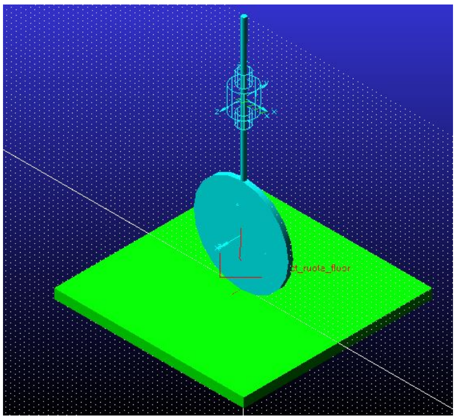

Figure 3.3: Test system

vertical angular velocity is applied. In each simulation, the vertical friction torque, the vertical angular velocity and the wheel-plane penetration length are measured. The expected behaviour is the reduction of the angular velocity down to zero due to the friction effect. It is important to choose an initial vertical angular velocity high enough, so that the vertical friction torque is initially in the dynamic range and then move to the static one due to the angular velocity reduction.

Test one In the first test, an arbitrary cylinder length is chosen as $L = 1\ cm$ and the friction torque dependency on the four contact parameters is studied. The exponent e and the damping ramp-up distance d are kept constant at $e = 1.1$ and $d = 0.01\ cm$ respectively. The maximum damping coefficient $c_{\max}$ and the stiffness values k can be varied independently. Three simulations are performed keeping constant the maximum damping coefficient at $c_{\max} = 10\ N/(cm/s)$ and assigning the stiffness k the following three values:

- Simulation 1: $k_1 = 1 * 10^3\ N/cm^{\mathrm{e}}$
- Simulation 2: $k_2 = 5 * 10^2\ N/cm^{\mathrm{e}}$
- Simulation 3: $k_3 = 1 * 10^2\ N/cm^{\mathrm{e}}$

All the three simulations start with an initial vertical angular velocity of $\theta_0 = 2000$ deg/s and last $t_{\mathrm{tot}} = 5s$. The time step used in the solver is $\Delta T = 0.001s$. The measures of interest that will be extracted from Figures 3.4 are the dynamic vertical friction torque T_d, the static vertical friction torque T_s, the time at which the transition between dynamic and static friction torque occurs t_1, the time at which the maximum static friction torque is present t_2, the vertical angular velocity at t_1 that is indicated with w_{v1}, the vertical angular velocity at t_2 that is w_{v2} and the penetration between the two bodies p. To give a rule for the choice of t_1, it is the time at which the vertical friction torque is 5% greater than the dynamic friction torque. All these quantities are listed in Table 3.3. Using an infinite stiffness value,

Table 3.3: Measured values in Test 1

Quantity	Unit measure	Simulation 1	Simulation 2	Simulation 3
T_d	$N \cdot cm$	-19.5	-22.8	-32.5
t_1	s	2.280	2.256	1.980
w_{v1}	deg/s	1161.3	882.7	330.7
T_s	$N \cdot cm$	-45.5	-53.2	-75.9
t_2	s	3.596	3.219	2.453
w_{v2}	deg/s	116.1	98.8	69.1
DD	cm	9.88	9.77	9.02

the distance DD between the wheel centre and the ground is equal to the wheel radius $R = 10\ cm$. Decreasing the stiffness value, the distance DD decreases, since bodies penetration occurs as it can be seen in Figure 3.4c. The higher penetration results into a higher vertical friction torque as reported in Figure 3.4b and therefore in a higher deceleration. The angular velocity in simulation 3 decreases faster than in simulation 1, as visible in Figure 3.4a.

Test two In the second test, four contact parameters are chosen and the friction torque dependency on the cylinder length is studied.

The four contact parameters are fixed equal to exponent $e = 1.1$, damping ramp-up distance $d = 0.01\ cm$, stiffness $k = 500\ N/cm^{\mathrm{e}}$ and maximum damping coefficient $c_{\max} = 10\ N/(cm/s)$. Two simulations will be performed assigning to the cylinder length L two values:

- Simulation 1: $L_1 = 1\ cm$
- Simulation 2: $L_2 = 8\ cm$

As in test 1, the two simulations start with an initial vertical angular velocity of

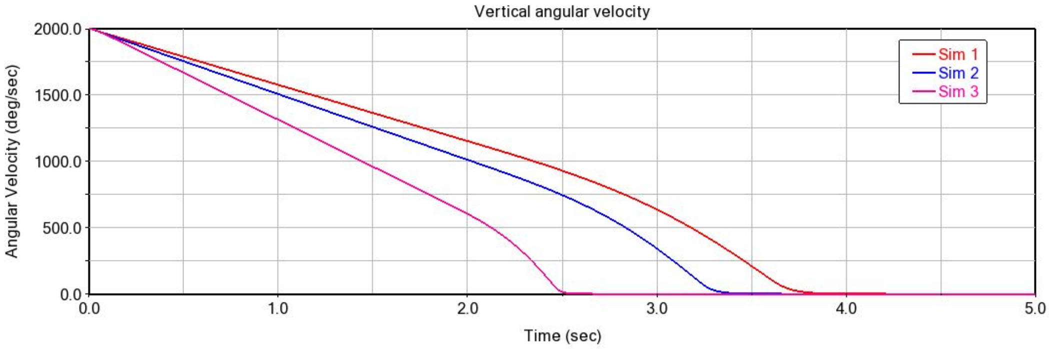

(a) *Angular velocity*

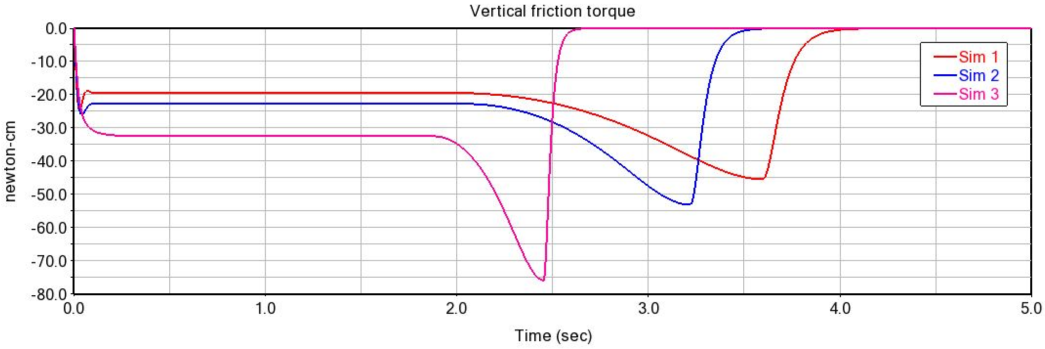

(b) *Vertical friction torque*

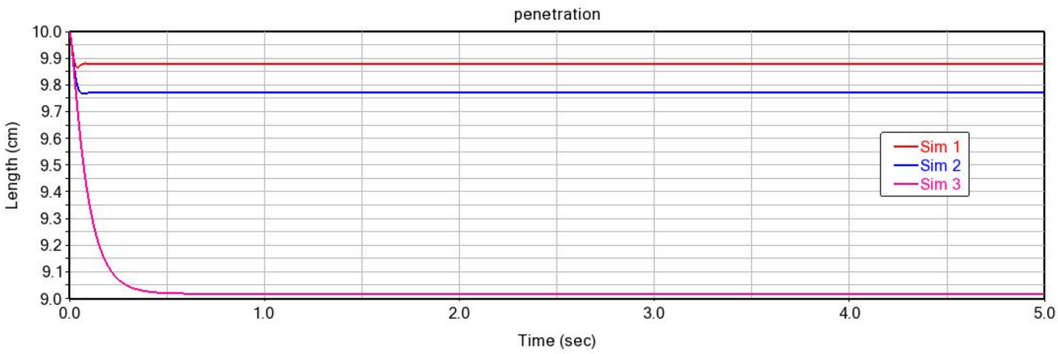

(c) *DD distance*

Figure 3.4: Measures Test 1

$\theta_0 = 2000\ deg/s$, last $t_{\text{tot}} = 5s$ and the time step used in the solver is $\Delta T = 0.001s$. The same measures done in test 1 are performed also in test 2 and are listed in Table 3.4. The distance DD does not change from simulation 1 to simulation 2 as expected, since it depends only on the four contact parameters that are not changed (Figure 3.5c). Greater is the cylinder length, greater is the vertical friction torque (Figure 3.5b) and therefore the deceleration. In simulation 2 the vertical

Table 3.4: Measured values in Test 2

Quantity	Unit measure	Simulation 1	Simulation 2
T_d	$N * cm$	-22.8	-64.5
t_1	s	2.256	1.209
w_{v1}	deg/s	882.7	312.3
T_s	$N * cm$	-53.2	-150.4
t_2	s	3.219	1.329
w_{v2}	deg/s	-98.8	35.6
DD	cm	9.77	9.77

angular velocity goes to zero much faster than in simulation 1 (Figure 3.5a).

Conclusions The final result is that both decreasing the spring stiffness and/or increasing the cylinder length, the vertical friction torque increases. Agilino wheels are quite rigid and therefore the wheel contact area on the ground is small. This results into a small vertical friction torque. For this reason, the Agilino wheels will be schematized with a cylinder having the same wheel radius but a different length in order to represent the small contact area. About the contact stiffness and the maximum damping coefficient, they must be tuned firstly to have a smooth normal contact reaction force. Smooth means with peaks whose amplitude is negligible with respect to the expected normal force. It must be remembered that the peaks are normal in a spring-damper system that continuously has to reach a new equilibrium depending on the robot whole motion. Therefore, the stiffness is reduced to reach a smooth contact normal reaction force, while the cylinder length is reduced as well to limit the vertical friction torque. The tuning of these two parameters will be performed later on when the final Agilino model will be built. Of course the tuning will be based on the trial and error procedure up to when the desired vertical friction torque is obtained. The specific values tried in the previous tests will be meaningless in the different Agilino model. The little oscillations that can be seen at the first instants on the vertical friction torque are due to the adjustment time needed by the the spring-damper system to reach equilibrium.

Longitudinal friction force

The longitudinal friction force exerted on the wheel is the second friction component to be investigated. Again the system is made of a wheel and a plane, but a planar joint is used in order to limit the wheel motion allowing only the vertical and longitudinal translations and the rotation around its main axis. An initial angular velocity along the main axis is imposed to the wheel and the longitudinal friction force is measured. The initial angular velocity has to be high enough, so that the

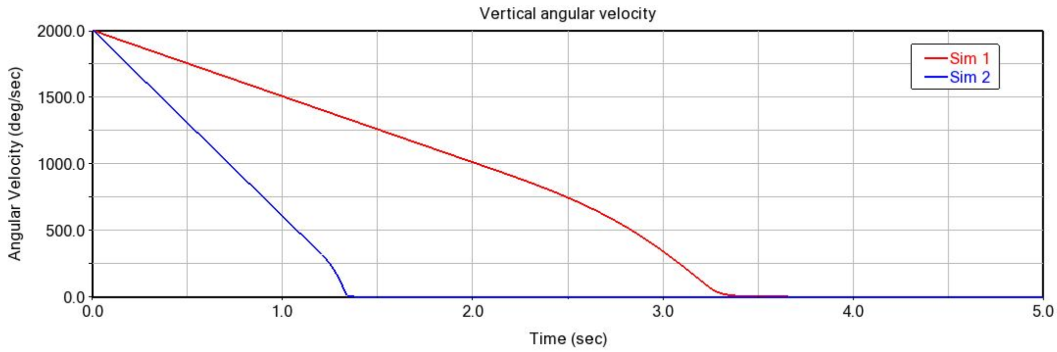

(a) *Angular velocity*

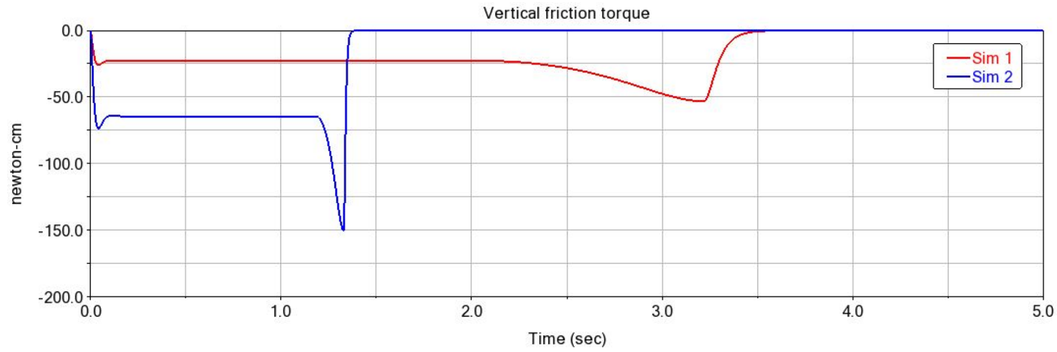

(b) *Vertical friction torque*

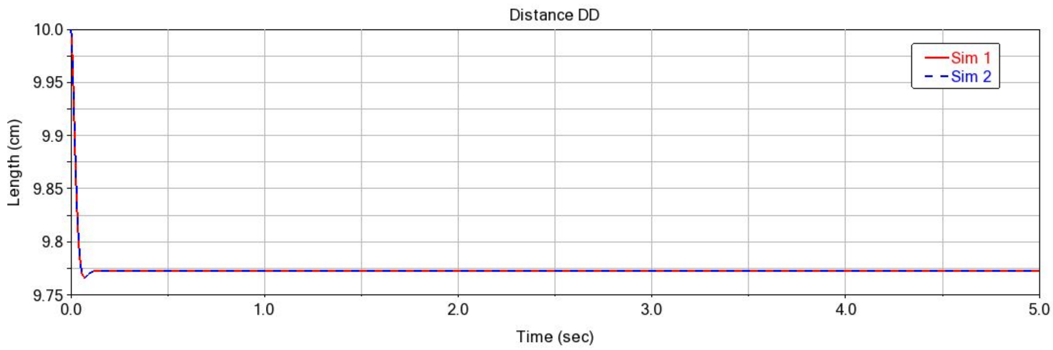

(c) *DD distance*

Figure 3.5: Measures Test 2

friction force starts in the dynamic range.

First test In this test, the cylinder length is $L = 1$ cm, the exponent $e = 1.1$ and the damping ramp-up distance $d = 0.01$ cm. Two simulations are performed to study the longitudinal friction force dependency on the stiffness k and on the maximum damping coefficient $c_{\max}$.

- Simulation 1: $c_{\max} = 50\ Ns/cm$ and $k = 5000\ N/cm^{e}$.
- Simulation 2: $c_{\max} = 15\ Ns/cm$ and $k = 500\ N/cm^{e}$.

Both the parameters are changed to guarantee a fast stabilization of the spring-damper contact with small oscillations. The initial angular velocity is fixed at $\omega_0 = -500\ deg/s$. In this test, the dynamic friction coefficient was reduced at the value of $\mu_d = 0.1$, while the static one at $\mu_s = 0.3$. This change results into a longer time needed by the wheel to transit from the initial slipping motion to the pure rolling motion. In this way, the transition occurs when the spring-damper system is adjusted and it is possible to appreciate it without the influence of eventual oscillations of the normal reaction force. The longitudinal friction force pushes the wheel forward increasing the translational velocity while reducing the angular velocity until the rolling motion is reached. The wheel reaches a potentially endless rolling motion, because neither the rolling friction nor the air viscous friction are modelled. The impossibility of modelling these two aspects is not a problem. Indeed, Agilino low speeds make the viscous friction negligible while its quite rigid wheels allow to not consider the rolling friction. Better always be aware of the simplifications performed even though they look right. The two simulations have almost the same longitudinal friction forces (Figure 3.6b) and translational velocities (Figure 3.6a). The steady state normal reaction forces are equal, while the transitions are different due to the change of the spring-damper parameters. Of course, the simulation with the smaller stiffness is characterized by a deeper penetration. In both simulations, the dynamic friction force and the maximum static friction force are equal to their expected values.

$$F_s^{\max} = \mu_s \cdot F_n = 29.43N$$

$$F_d = \mu_d \cdot F_n = 9.81N$$

The contact parameters does not affect the longitudinal friction force.

Second test Changing the wheel length form $L = 1\ cm$ to $L = 10\ cm$, nothing changes in both the simulations performed in the previous paragraph.

Conclusions Neither the contact parameters nor the cylinder length directly affect the longitudinal friction force. The contact parameters can affect it indirectly through the normal reaction force. Indeed they affect the transients of the normal force, allowing a variation more or less quick and with or without oscillations.

Tangential friction force

The transversal friction force exerted on the wheel is the third and last friction component investigated. Again the system is made of a wheel and a plane. Two translational joints are used in couple in order to allow only the vertical and transversal translations. An initial translational velocity along the main axis is imposed to the

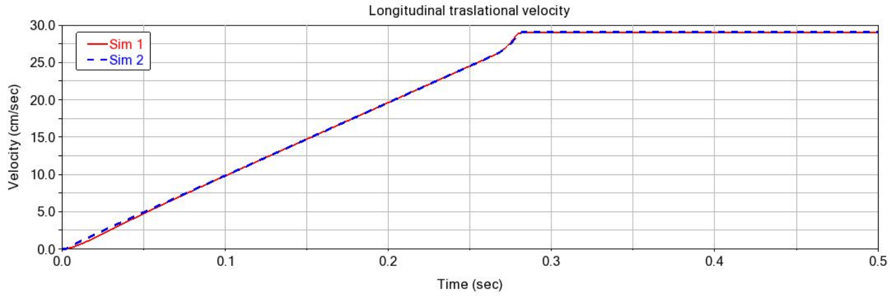

(a) *Longitudinal translational velocity*

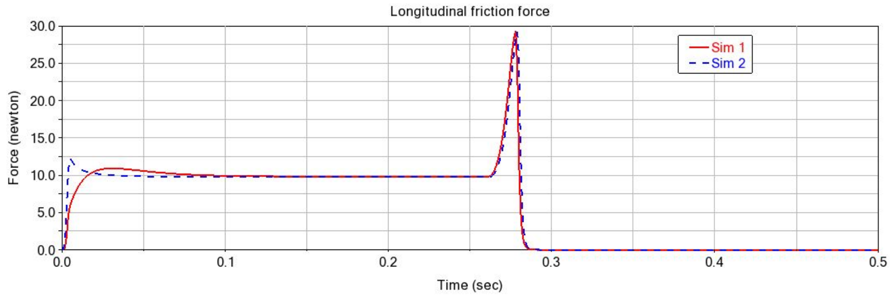

(b) *Longitudinal friction force*

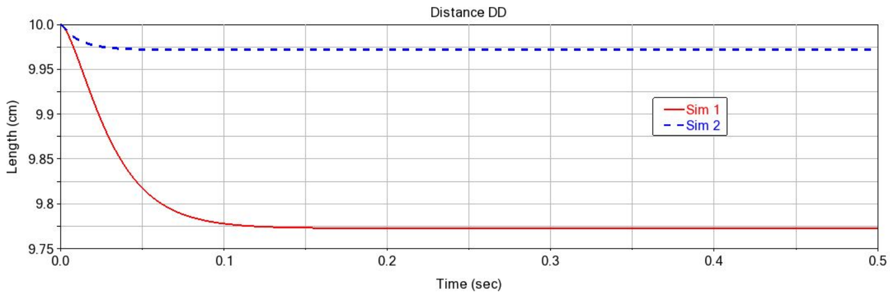

(c) *DD distance*

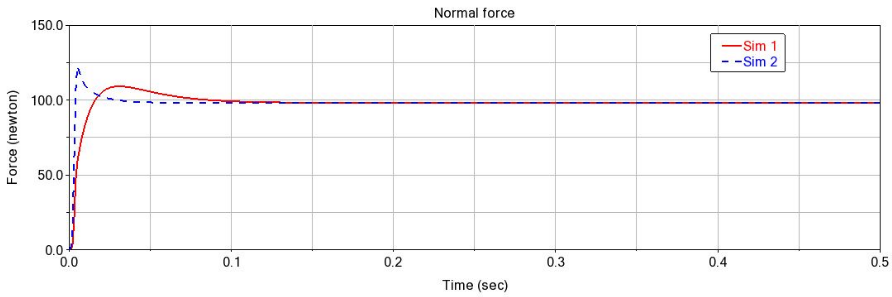

(d) *Normal reaction force*

Figure 3.6: Measures Test 2.1

wheel and the transversal friction force is measured. The initial transversal velocity has to be high enough so that the sliding motion is appreciable. The friction force decelerates the wheel translation until the wheel stops. As for the longitudinal friction forces, neither the contact parameters nor the cylinder length affect directly the transversal friction force and the contact parameters can affect it indirectly through the normal reaction force. In Figure 3.7 the transversal force and velocity are shown.

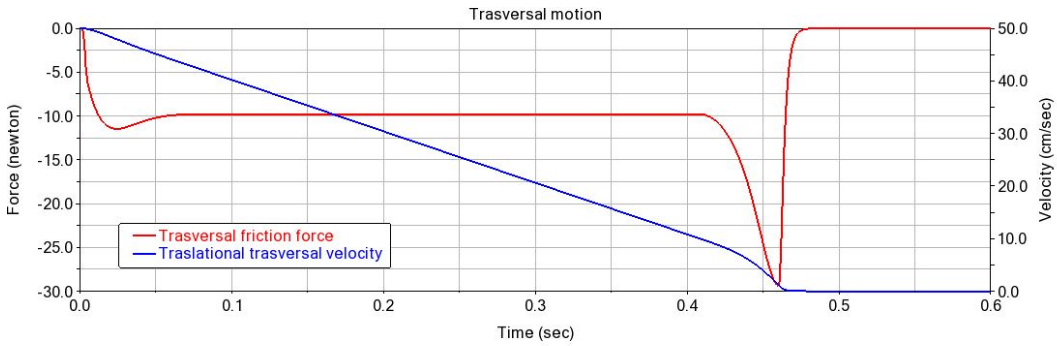

Figure 3.7: Test system

Final conclusions

It is possible to conclude that the choice of the contact parameters is important to fix the transients of the normal force variations. Their choice would be performed with trial and error procedure in Agilino model in order to have fast and smooth variations without oscillations. An example of normal force variation is when the robot enters a turn. Indeed, the inner wheel normal force decreases while the outer wheel one increases. Instead the cylinder length will be chosen to obtain the real vertical friction torques at the wheels. Longitudinal and lateral friction forces are not directly influenced by these parameters. They only depend on the four friction parameters.

3.4 Agilino model

Three models have been developed, increasing every time the model complexity. The last one will be used for the mathematical model refinement. For the Agilino models, the robot is divided into three main layers. These are the wheels' layer, the base layer and the upper volume layer.

The wheels layer is equal in all the three models. As said before, the Agilino robot has two fixed wheels and four castors, two in the front and two in the back. Both front and rear castors are symmetrical with respect to the robot longitudinal axis. For this reason, each couple is substituted in the model with just one castor placed on the longitudinal axis and at the same distance from the robot logic centre. It is an acceptable approximation. The two castor wheels are slightly shifted above vertically with respect to their real positions to guarantee that during simulations only one at a time is in contact with the ground. The wheels are modelled with cylinder solid shape available in Adams. Each cylinder will match the corresponding wheel characteristics that are its radius, centre of mass, mass and inertia matrix. As said before, the cylinder length must be tuned according to the vertical friction torque that is desired at each wheel contact point. It could be said that the cylinder length represents somehow the wheel footprint on the ground. Therefore, the driving wheel cylinder will be thicker than the castor one. Indeed, the mechanical design puts most of the weight on driving wheels. In Table 3.5 the mechanical parameters of the driving wheels are listed. In Table 3.6 the castor ones can be found. The mass centre of each wheel is placed in the wheel centre. For the castors, this is an approximation due the presence of the arm containing the vertical joint. The inertia moments of each wheel are computed with respect to the reference frame having its origin in the mass centre, z and x axes in radial directions and y axis on the wheel main axis. In the planar motion approximation, the z axis is the vertical one. For castor wheels, the chosen reference frame is not the principal one, nevertheless the inertia matrix is considered diagonal to simplify its computation. Both the castor wheel approximations are acceptable since its contribution to the robot total mass and inertia is negligible. The wheels inertia moments are computed exploiting the cylinder formulas. The longitudinal axis inertia moment I_a and the radial inertia moment I_r are reported in the following.

$$\begin{cases} I_a = \frac{mr^2}{2} \\ I_r = \frac{mr^2}{4} + \frac{mh^2}{12} \end{cases}$$

where m is the cylinder mass, r the cylinder radius and h the cylinder length. In the castor wheels the radial inertia moment with respect to the vertical axis z is increased of 10%, to take into account the presence of the castor wheel arm.

Table 3.5: Driving wheels description

Quantity	Symbol	Unit measure	Value
mass	m_w	Kg	0.8
radius	r_w	cm	10.0
width	h_w	cm	5.0
cylinder length	s_w	cm	5.0
main axis inertia moment	J_{wy}	$Kg \cdot cm^2$	40.0
radial inertia moments	$J_{\mathrm{wx}}, J_{\mathrm{wz}}$	$Kg \cdot cm^2$	21.67

Table 3.6: Castor wheels description

Quantity	Symbol	Unit measure	Value
mass	m_c	Kg	0.2
radius	r_c	cm	1.75
width	h_c	cm	2.7
approximating cylinder length	s_c	cm	1.0
arm	b_c	cm	1.5
main axis inertia moment	J_{cy}	$Kg \cdot cm^2$	0.31
horizontal radial axis inertia moment	J_{cx}	$Kg \cdot cm^2$	0.27
vertical radial axis inertia moment	J_{cz}	$Kg \cdot cm^2$	0.3

The base layer includes only the robot base. It is the platform where all the components are directly or indirectly connected to. In the first two models, the robot base has the shape of a thin cylinder. The relevant part is not the shape but its mechanical description. Therefore, the mass centre position, the mass value and the inertia matrix components. The mechanical description is found importing the base CAD geometry into Adams. Indeed, the user just has to select the desired component material and Adams will compute autonomously everything. The base material is aluminium. The base description can be found in Table 3.7.

Table 3.7: Robot base description

Quantity	Symbol	Unit measure	Value
mass	m_b	Kg	5.7
vertical inertia moment	J_{bz}	$Kg \cdot cm^2$	3382
longitudinal inertia moment	J_{bx}	$Kg \cdot cm^2$	1480
transversal inertia moment	J_{by}	$Kg \cdot cm^2$	1902

The upper volume layer contains all the components needed by the robot to move autonomously. The upper volume total mass is equal to the sum of all the components masses, while its centre of mass position and its inertia matrix can be found knowing the spatial distribution of the components. In the first model, the upper volume was schematized with a unique body visually described by a cube solid shape. In Adams, the approximation of the upper volume with a unique body makes the model less versatile. Indeed, if the components position is changed, the mass centre location and the inertia matrix have to be computed again to provide Adams cube the new proper description. Instead, it would be better to exploit more Adams that autonomously take care of the different components positions. It is done in the second model whose picture can be seen in Figures 3.8a, 3.8b, 3.8c, 3.8d where the components having the biggest masses are considered autonomously and schematized with point masses. All the other components are incorporated into the robot bearing structure, that is modelled with an hollow cylinder shape.

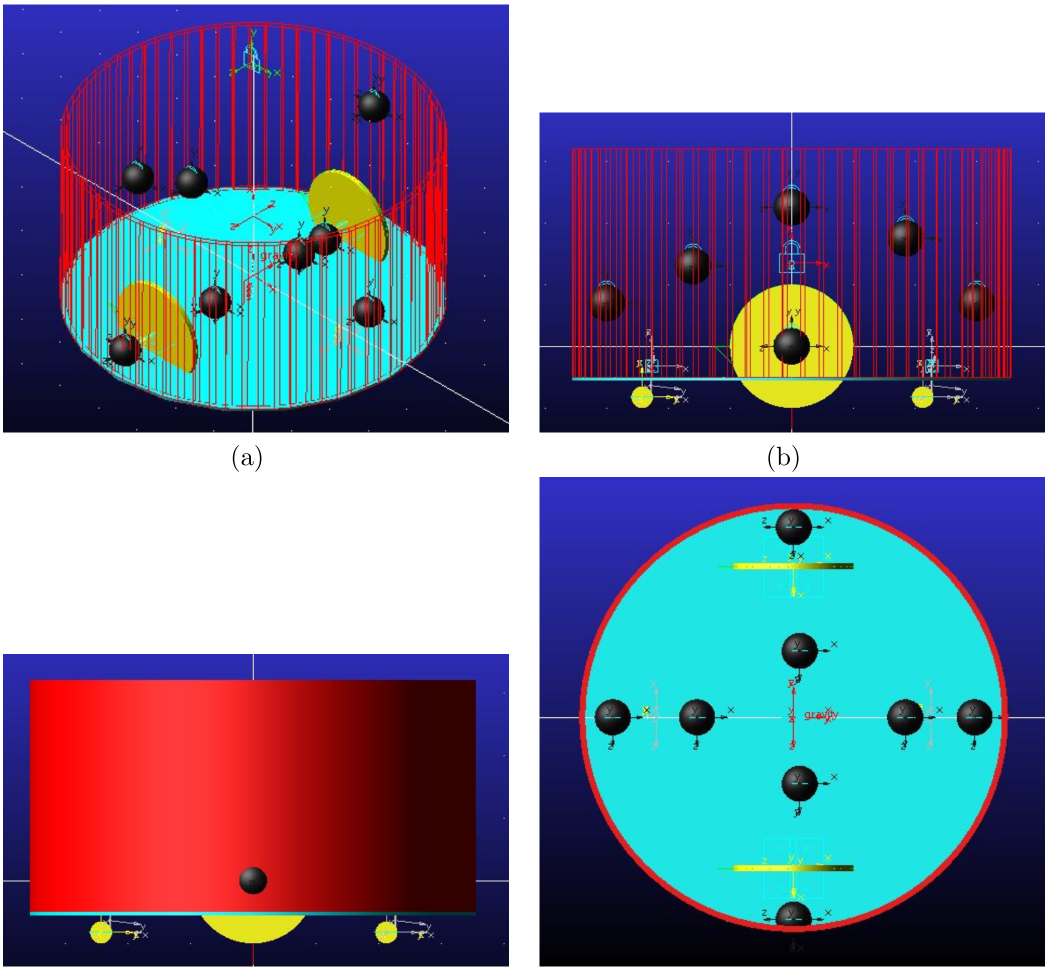

(a) (b) (c) (d)

Figure 3.8: Agilino model in Adams second version

The allow cylinder solid shape is chosen for two reasons. The first one is the axial symmetry with respect to its longitudinal axis while the second one is that it is empty inside. These two characteristics make it similar to the real bearing structure, that is a shell that supports all the robot components and that is almost symmetrical with respect to the z axis of the logic centre reference frame R_a. The allow cylinder longitudinal axis coincides with the z axis of R_a. The allow cylinder geometry is described by a medium radius r and a length L whose values are chosen to resemble the real bearing structure geometry. The mass m is extracted from the CAD files imported in Adams. The allow cylinder formulas are used to compute the bearing structure inertia moments with respect to its mass centre. The longitudinal inertia moment I_a and the radial inertia moment I_r formulas with respect to the allow cylinder centre are reported in the following.

$$\begin{cases} I_a = mr^2 \\ I_r = \frac{mr^2}{2} + \frac{mh^2}{12} \end{cases}$$

The allow cylinder parameter are listed in Table 3.8.

Table 3.8: Allow cylinder description of the bearing structure

Quantity	Symbol	Unit measure	Value
mass	m_{BS}	Kg	23
medium radius	R_{BS}	cm	33
length	L_{BS}	cm	37.2
longitudinal inertia moment	I_{BSz}	$Kg \cdot m^2$	2.5
radial inertia moment	$I_{\mathrm{BSx}}, I_{\mathrm{BSy}}$	$Kg \cdot m^2$	1.5

Therefore, the chosen modelling procedure for the main components of the upper volume is the following.

1. Select the components of the upper volume that have the biggest masses. These are the two laser scanners, the two motors, the two reducers, the PLC, the battery and the charge base plate.
2. Look for the previous components' masses on their data sheets. The masses values are listed in Table 3.9.
3. Locate approximately the mass centre on each component.
4. Find each mass centre position (COM) in the robot using the robot CAD assembly file. Each vector position is described with respect to the reference frame that has the origin in the robot logic centre, the x axis on the robot longitudinal axis and the y axis on the robot transversal axis. This reference frame from now on will be called the logic centre reference frame. The vectors are listed in Table 3.9.
5. Built the Adams model of the upper volume, approximating each main component with a small sphere located at the component mass centre position. Its mass is equal to the component's mass while the inertia moments are set so small to be negligible. In this way each component is effectively approximated as a point mass.

As said before, Adams takes care autonomously of the components positions but it does not return the centre mass position, the total mass and the inertia moments of the upper volume. The user has to compute them on its own. These three information are needed later for the mathematical model, therefore they will

Table 3.9: Upper volume components masses and mass centres positions

Quantity	Symbol	Unit measure	Value
motor mass	m_M	Kg	5.1
laser scanner mass	m_{LS}	Kg	1.45
battery mass	m_B	Kg	8.0
reducers mass	m_R	Kg	5.3
PLC mass	m_{PLC}	Kg	1
charge plate mass	m_{CP}	Kg	2.2
bearing structure (BS) mass	m_{BS}	Kg	23.0
motors COM	r_M	cm	[18.5; 0.0; 17.5]
first laser scanner COM	r_{LS1}	cm	[30.0; 0.0; 7.0]
second laser scanner COM	r_{LS2}	cm	[-30.0; 0.0; 7.0]
battery COM	r_B	cm	[-16.0; 0.0; 13.0]
first reducer COM	r_{R1}	cm	[1.0; 11.0; 0.0]
second reducer COM	r_{R2}	cm	[1.0; -11.0; 0.0]
PLC COM	r_{PLC}	cm	[0.0; 31.5; 22.5]
charge plate COM	r_{CP}	cm	[0.0; -33.5; 0.0]
bearing structure COM	r_{BS}	cm	[0.0; 0.0; 16.8]

be computed now exploiting the modelling approximations done here. The upper volume total mass M_m is computed summing all the components' masses in (3.7). The upper volume mass centre position r_{m0} is computed in (3.8) with respect to the logic centre reference frame R_a. The upper volume inertia moment I_{mzz} with respect to a vertical axis passing through its mass centre is computed in (3.9). The inertia moment of each point mass is equal to the mass value m multiplied for the square of its distance d from the axis. Instead, the inertia moment of the bearing structure is computed exploiting the parallel axis theorem. It is equal to $I_{\text{BSz}} + m_{\text{BS}} * d_{\text{BS}}^2$, where I_{BSz} is the inertia moment with respect to the vertical axis passing through the bearing structure mass centre and d_{BS}^2 is the distance between the previous axis and the vertical axis passing through the upper volume mass centre. The values can be found in Table 3.10. It can be seen that the mass centre is placed in the front from the longitudinal point of view, $x_{\text{m0}} = 1.23\ cm$ and shifted a little to the right from the transversal point of view, $y_{\text{m0}} = -0.73\ cm$.

$$M_m = m_M + 2 \cdot m_{\text{LS}} + m_B + 2 \cdot m_R + m_{\text{PLC}} + m_{\text{CP}} + m_{\text{BS}} \tag{3.7}$$

$$\begin{aligned} r_{\text{m0}} = (&m_M \cdot r_M + m_{\text{LS}} \cdot r_{\text{LS1}} + m_{\text{LS}} \cdot r_{\text{LS2}} + m_B \cdot r_B + m_R \cdot r_{\text{R1}} + \\ &+ m_R \cdot r_{\text{R2}} + m_{\text{PLC}} \cdot r_{\text{PLC}} + m_{\text{CP}} \cdot r_{\text{CP}} + m_{\text{BS}} \cdot r_{\text{BS}})/M_m \end{aligned} \tag{3.8}$$

Table 3.10: Upper volume relevant parameters

Quantity	Symbol	Unit measure	Value
upper volume mass	M_m	Kg	57.9
upper volume COM	r_{m0}	cm	[1.23; -0.73; 12.29]
vertical inertia moment	I_{mzz}	$Kg \cdot m^2$	3.78

$$I_{\mathrm{mzz}} = m_M \cdot d_M^2 + m_{\mathrm{LS}} \cdot d_{\mathrm{LS1}}^2 + m_{\mathrm{LS}} \cdot d_{\mathrm{LS2}}^2 + m_B \cdot d_B^2 + m_R \cdot d_{\mathrm{R1}}^2 + \\ + m_R \cdot d_{\mathrm{R2}}^2 + m_{\mathrm{PLC}} \cdot d_{\mathrm{PLC}}^2 + m_{\mathrm{CP}} \cdot d_{\mathrm{CP}}^2 + m_{\mathrm{BS}} \cdot d_{\mathrm{BS}}^2 + I_{\mathrm{BSz}} \quad (3.9)$$

In the third and last model in Adams (Figures 3.9a, 3.9b, 3.9c, 3.9d), the bearing structure is not schematized with an allow cylinder but it is realized importing the real CAD geometries and assigning to them the aluminium material. The main robot components supported by the bearing structure are still described as point masses since this methodology makes the model update very quick. Indeed, if a component position is changed, just the vector position of the corresponding sphere must be changed. Or if a component is added, a new sphere is introduce in the position of the component mass centre. The simulations result will be less precise but it is acceptable. Of course approximations are acceptable only when the modelling engineer is aware of them.

Performing simulations and using the trial and error procedure, the contact and friction parameters of the wheel-ground interaction are set and the values are reported in Table 3.11.

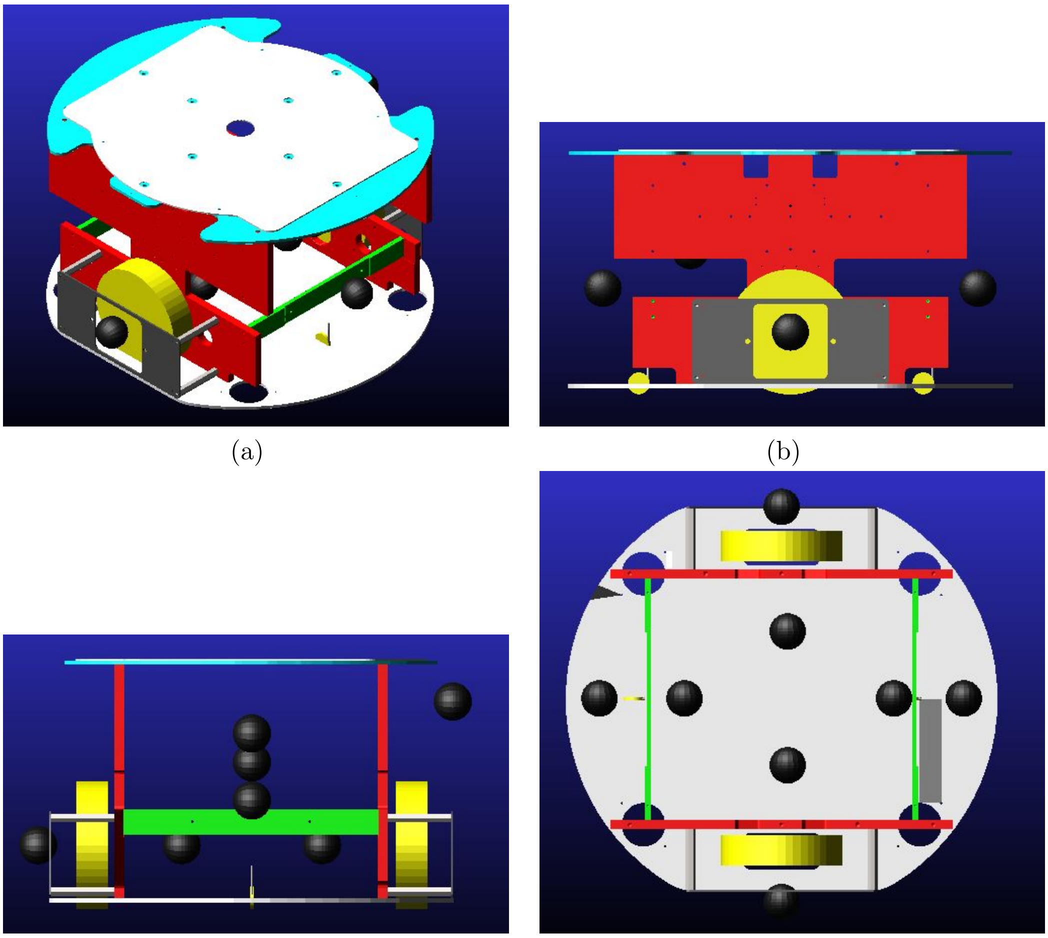

(a) (b) (c) (d)

Figure 3.9: Agilino model in Adams third and final version.

Table 3.11: Contact and friction parameters

Quantity	Symbol	Unit measure	Value
driving wheel spring stiffness	k	N/cm^e	10^4
driving wheel spring exponent	e	–	1.1
driving wheel maximum damping coefficient	$c_{\max}$	$N/(cm/s)$	10^2
driving wheel damping ramp-up distance	d	cm	0.01
driving wheel static friction coefficient	μ_s	–	0.6
driving wheel dynamic friction coefficient	μ_d	–	0.1
driving wheel stiction transition velocity	v_s	cm/s	1.0
driving wheel friction transition velocity	v_d	cm/s	10.0
castor wheel spring stiffness	k	N/cm^e	900
castor wheel spring exponent	e	–	1.1
castor wheel maximum damping coefficient	$c_{\max}$	$N/(cm/s)$	10
castor wheel damping ramp-up distance	d	cm	0.01
castor wheel static friction coefficient	μ_s	–	0.2
castor wheel dynamic friction coefficient	μ_d	–	0.1
castor wheel stiction transition velocity	v_s	cm/s	1.0
castor wheel friction transition velocity	v_d	cm/s	10.0

Chapter 4

Robot dynamic model

After having created the Adams model, the robot mathematical equations must be found. The two modelling techniques available are the Lagrange approach and the Euler-Newton approach. The literature on modelling differential drive robots is not poor, therefore many scientific papers that are present in the bibliography have supported this work. The goal is to find in literature an existing model that can work for this thesis purposes or extend an existing model with new information.

In [11] the most used dynamic model for the description of differential dynamic robots was introduced. Its simplicity makes it suitable for control purposes when motors control algorithms have to be developed. The goal of the thesis is to develop a little more complex and general dynamic model for both the safe trajectories planning and the mechanical components choice. On safe trajectories the robot does not slip longitudinally or slide laterally ever.

For the following considerations, the robot structure is considered as a unique body characterized by a mass m and an inertia matrix J. The model in [11] approximates the robot motion with a planar one described by the three posture parameters $\xi = [x_a, y_a, \theta_z]$ with respect to the absolute inertial frame that has the x and y axes on the plane and the z axis perpendicular to it. Therefore, the mathematical model equations derive only from the forces' and torques' balances related to the three posture parameters. The forces' balances on the x and y directions and the moments' balance on the z direction:

$$\begin{cases} F_x = m\ddot{x} \\ F_y = m\ddot{y} \\ M_z = J_z\ddot{\theta}_z \end{cases} \tag{4.1}$$

Instead, the new model considers all the six forces' and torques' balances. Therefore, the robot motion should be described by six variables $\xi = [x_a, y_a, z_a, \theta_x, \theta_y, \theta_z]$. The two rotation angles $[\theta_x, \theta_y]$ around the x and y axes of the inertial frame can be replaced with the roll and pitch angles $[\theta_r, \theta_p]$ of the robot about its longitudinal and transversal axes respectively, keeping the posture description valid. Since it's easier to deal with a planar motion, the three variables $[z_a, \theta_r, \theta_b]$ are supposed to be constant and their velocities and accelerations are set to zero in the equations. These approximations assume that the robot base is always parallel to the plane thanks to the presence of the rear and front castor wheels. This approximation allows also to easily solve the inverse dynamic problem, where the posture variables and their first and second derivatives are the inputs while the forces the outputs. It is straightforward to assign the time evolution to the three parameters $[x_a, y_a, \theta_z]$ according to the desired planar trajectory. Instead, the other three possible parameters $[z_a, \theta_r, \theta_b]$ cannot be assigned as inputs since their time evolution depends on the dynamic evolution of the whole system. They should have been considered outputs as the forces. So it is better to suppose them constant for simplicity. Therefore, the new model mathematical equations come from the six balance equations.

$$\begin{cases} F_x = m\ddot{x} \\ F_y = m\ddot{y} \\ F_z = m\ddot{z} \quad = 0 \\ M_r = J_r\ddot{\theta}_r \quad = 0 \\ M_b = J_b\ddot{\theta}_b \quad = 0 \\ M_z = J_z\ddot{\theta}_z \end{cases} \tag{4.2}$$

where r and b are the rolling and pitch robot directions. Summarizing, the previous model approximates the robot as if it is a paper sheet without thickness moving on a plane. Instead, the new model starts considering the robot in all its three dimensions, adding the one perpendicular to the ground plane.

4.1 Features of the developed dynamic model

The dynamical aspects that have been taken into account in the robot modelling are listed in the following.

1. This mathematical model equations are exploited for the solution of the inverse dynamic problem. The goal is to solve the inverse dynamic problem obtaining the contact forces exerted on each driving wheel by the ground. Each driving wheel-ground interaction is described by three forces that are the normal reaction force $f_{\text{cz1}}, f_{\text{cz2}}$, the longitudinal traction force $f_{\text{cx1}}, f_{\text{cx2}}$ and the lateral force $f_{\text{cy1}}, f_{\text{cy2}}$, where the subfix 1 refers to the left wheel and the subfix 2 to the right one.
   - The reaction normal forces at the wheels' contact points f_{cz1} and f_{cz2} appear in the model and allow to know how the robot weight is split among the wheels contact points during motion. For example, in a turn

the robot weight moves partially from the inner driving wheel to the outer one. During acceleration, the weight moves partially to the rear castor wheel lightening the driving ones. The knowledge of the reaction normal forces at the contact points is the key information that allows to discover if lateral slide and/or longitudinal slip constrains are violated or not at the driving wheels.

- The longitudinal forces f_{cx1} and f_{cx2} are the active traction forces that must be exerted to follow the desired trajectory.
- The lateral forces f_{cy1} and f_{cy2} are the passive forces that points to the instantaneous centre of rotation ICR when the robot is performing a curve in its trajectory. It opposes the centrifugal force avoiding the robot lateral slide.

The longitudinal and lateral forces values returned by the inverse dynamic problem are the ones that ideally allow the robot to follow the desired trajectory given in input. But only a wheel-ground interaction model will tell the user if the desired trajectory is safe or not.

(a) The simplest model of wheel-ground interaction is the one where the contact occurs in a point. The total friction force f_c exerted by the ground on each wheel must be lower or equal to the maximum static friction force $f_s^{\max}$ present every instant at that wheel, in order to avoid slip or slide effects. The total friction force at each wheel f_c is equal to the module of the vectorial sum of f_{cx} and f_{cy}. Since the two components are perpendicular, the Pythagorean theorem can be used. The maximum static friction force $f_s^{\max}$ is equal to the normal force f_{cz} multiplied for the static friction coefficient μ_s that depends on the wheel and ground materials. The ground is an industrial floor, while the driving wheels external layers are made of polyurethane, so the static friction coefficient chosen is equal to $\mu_s = 0.6$. The contact normal force f_{cz} at each wheel changes during motion.

$$\begin{cases} f_c = \sqrt{f_{\text{cx}}^2 + f_{\text{cy}}^2} \\ f_s^{\max} = \mu_s \cdot f_{\text{cz}} \\ f_c \leq f_s^{\max} \end{cases} \tag{4.3}$$

(b) More complex models can be used where the deformation of the wheels are taken into account. For example, it is possible to compute the wheel deformation under the known weight force f_{cz} and the wheel contact area with the ground. From these information, the maximum friction force the ground can exert on the wheel before slip/slide occurs can be determined. If it is lower than the one required by the model to follow a desired trajectory, slip occurs. Of course these models are too complex for this thesis purposes. Further detail can be found in [12].

As it can be seen, the robot model and the wheel-ground interaction model are supposed to be independent. Of course it is an approximation that seems to be valid at the wheeled mobile robot velocities and accelerations. Indeed, the contact forces at the driving wheels are computed from the robot model and then the contact forces are analysed with the interaction model. This is an advantage, because it is not necessary to decide an a-priori model of the wheel-ground interaction, since the three forces come out of the robot model independently. The introduction of the vertical dynamics also helps in the choice of the motors and reducers, which need to have a maximum radial weight they can withstand higher than the one relative to the worst case of repartition of the robot weight among the wheels.

2. The castor wheels, that were not considered in the model of paper [11], enters the new one. Their presence allows the robot weight balance, indeed only two wheels do not allow the static positioning of the robot on a plane. Their interaction with the ground is not considered in the model. This means that the influence of the castor friction force on the robot motion is neglected. As already said, Agilino has four castor wheels, two in the front and two in the rear part of the robot. They are placed in a symmetrical way with respect to both the longitudinal and transversal axes. In order to simplify the equations, the two front wheels have been merged in one wheel and the same have been done for the rear wheels. The same simplification characterizes the Adams model. Since the castor wheels are usually quite rigid, it is supposed that only one is in contact with the ground at each instant. In this way the system is not hyper static, because the robot has three contact points at a time and three points define a plane that is the ground. The model is made of two sub-models, one with the castor wheel in the front and the other with the castor wheel in the back. Since the two castors have the same distance from the robot logic centre, when the castor normal force of one model is positive the one of the other model is equal in module but opposite in sign. The normal reaction force f_{c3z} at the castor wheel contact point is an output of the inverse dynamic problem of each sub-model, therefore it can be monitored continuously. The inverse dynamic problems of both the sub-models are solved simultaneously and at each instant the total model solution coincides with the one of the sub model whose castor is in contact with the ground, therefore that has f_{c3z} greater than zero.
3. In the model of paper [11], the centre of mass belongs to the longitudinal axis of the robot base and the only meaningful information is its distance from the robot logic centre. The logic centre is the middle point of the driving wheels' axis. In the developed model, two new features are introduced.

   - The centre of mass of the upper volume can be placed everywhere on the robot base, therefore the robot can be also longitudinally not symmetrical. This aspect is important because makes the robot more general. A symmetrical robot needs the same torques τ_1 and τ_2 applied to the driving wheels to go straight during an acceleration phase, while a robot that is not symmetrical no. If the centre of mass does not lay on the longitudinal axis, the normal reaction force of one of the two wheels will be higher than the other one.

- The vertical distance of the upper volume centre of mass from the robot base z_m influences deeply the robot dynamics. Greater is the distance from the robot base, greater is the moment of the inertial force during the acceleration phases and greater is the moment of the centrifugal force during the turns. This results in normal forces changes at the driving wheels contact points.

4. In the previous model every part is considered rigid, while in the new one the upper body is connected to the robot base through three springs $[k_x, k_y, k_z]$. In this way the rigidity of the structure above the base of the robot can be tuned. Its modelling is interesting, because during acceleration and deceleration phases the position of the centre of mass of the upper volume can slightly change, changing the repartition of the total weight on the contact points.
5. In the previous model the friction at the bearings of the driving wheels was not modelled. In the new one it is. It allows the inverse dynamic problem to return more realistic values of the torques τ_1 and τ_2 that the motors have to deliver in order to follow the desired trajectory. More realistic torques values allow to perform a good and precise choice of the motors and reducers without overestimating them too much to play safe. The bearing friction torque is modelled similarly to the one in Adams. The friction arm is set equal to $R_{\text{arm}} = 4.8$ *cm* that is the radius at which the balls centres of the reducers bearings are placed, while the pin radius is set equal to $R_{\text{pin}} = 1.25$ *cm*, that is the radius of the reducer shaft.

$$T_{\text{friction}} = \mu \cdot [R_{\text{arm}} \cdot F_{\text{axialreaction}} + R_{\text{pin}} \cdot F_{\text{rotationalreaction}}] \tag{4.4}$$

The friction coefficient μ is related to the robot wheel angular speed $\dot{\theta}$ through the Coulomb approximation. Therefore both the stiction and sliding effects are considered. The mathematical formulas used to link μ with $\dot{\theta}$ are the following. First, the dynamic friction coefficient $\mu_d = \hat{\mu}_1 = 0.1$ and the static friction coefficient $\mu_s = \hat{\mu}_2 = 0.2$ are set. The two angular velocities v_t and v_{sp} are tuned to fix the desired stiction transition velocity equal to 0.001 rad/s and the friction transition velocity equal to 0.0035 rad/s. They have been set equal to $v_t = 0.001\ rad/s$ and $v_{\text{sp}} = 0.001\ rad/s$.

$$\begin{cases} \mu_{\text{c1}} = \hat{\mu}_1 \cdot \tanh(\dot{\theta}/v_t) \\ \hat{\mu}_3 = \hat{\mu}_2 - \hat{\mu}_1 \cdot \tanh(v_{\text{sp}}/v_t) \\ g = (\dot{\theta}/v_{\text{sp}}) \cdot \exp\Big(-\Big(\frac{\dot{\theta}}{v_{\text{sp}} \cdot \sqrt{2}}\Big)^2 + \frac{1}{2}\Big) \\ \mu_{\text{c2}} = \hat{\mu}_3 \cdot g \\ \mu = \mu_{\text{c1}} + \mu_{\text{c2}} \end{cases} \tag{4.5}$$

6. The previous model is constrained on an horizontal planar motion. Instead the new one can be generalized to a generic inclined plane motion just changing the components of the gravity acceleration vector g. This is very important because on an inclined plane the total robot weight is split into two components, one perpendicular and one parallel to the plane. Therefore, the normal reaction forces at the driving wheels f_{cz1} and f_{cz2} reduce limiting more the robot motions in order to avoid lateral slide or longitudinal slip.
7. In the new model, the point where a truck or a library is connected can be placed wherever on the robot base, fixing also its vertical distance from the robot base $[x_L, y_L, z_L]$. Greater is the vertical distance z_L, greater is the moment of the reaction forces $(f_{\text{tLx}}, f_{\text{tLy}})]$ exerted on the robot by the truck it is pulling. The risk is that a high acceleration together with a long arm z_L can lighten the driving wheels normal forces f_{cz1} and f_{cz2} moving the weight to the rear castor wheel and resulting into wheels slippage.
8. In this new model it is possible to know when a driving wheel is no more in contact with the ground just looking at the sign of the normal reaction force f_{cz1} and f_{cz2}. If it becomes negative, the robot has fallen apart.

4.2 Equations development

The equations of the mathematical model have been found using the Newton-Euler approach. The equations are written with respect to the robot longitudinal v and angular ω velocities and not with respect to the posture coordinates values and derivatives. The posture coordinates time evolution will be computed from the two significant velocities v and ω, supposing an initial position $[q_{10}; q_{20}]$ and orientation q_{30}. The robot is ideally divided into four parts that are the robot base, the two driving wheels and the robot upper volume. Each part motion can be divided into two rotations that occur simultaneously. The first rotation considers all the robot masses concentrated in the robot logic centre and occurs around the vertical axis passing through the instantaneous centre of rotation. The second rotation considers the different parts mass centres placed in the real positions and occurs around the vertical axis passing through the logic centre. The two rotations are characterized by the same angular velocity ω and acceleration $\dot{\omega}$. Indeed, they are two sides of the same coin and occur simultaneously. The first rotation describes the logic centre motion, while the second one the fact that at each instant the robot longitudinal axis has to be tangent to the trajectory described by the first rotation. The equations development is performed into non-inertial reference frames since the dependency on the posture coordinates is not relevant. The apparent forces related to the two rotations will be computed independently and then summed up. For each rotation, two apparent forces must be considered that are the centrifugal force F_{cf} and the inertial force F_i. The centrifugal force is present since a circular trajectory is performed. Instead, the inertial force is taken into account since the tangential acceleration is non null being the circular motion accelerated. The equations of the two forces are:

$$\begin{cases} F_{\text{cf}} = m \cdot (\omega \times (\omega \times r')) \\ F_i = m \cdot (\dot{\omega} \times r') \end{cases} \tag{4.6}$$

Considering the first rotation, the chosen non-inertial reference frame R_{ICR} has the origin in the instantaneous centre of rotation and is integral with the logic centre, where all the masses are supposed to be concentrated. Since R_{ICR} is integral with the logic centre, its angular velocity with respect to the inertial reference frame, that has the same origin, is equal to the logic centre angular velocity $\omega = [0; 0; \omega]$ around the ICR. The logic centre is located at $r_{\text{RICR}} = [0; -r; 0]$ with respect to the R_{ICR} reference frame, where r is the turn radius. Using (4.6), the inertial acceleration a_0 and the centripetal acceleration a_C are computed and listed below:

$$a_0 = \begin{bmatrix} r \cdot \dot{\omega} \\ 0 \\ 0 \end{bmatrix} = \begin{bmatrix} \dot{v} \\ 0 \\ 0 \end{bmatrix} \quad a_C = \begin{bmatrix} 0 \\ r \cdot \omega^2 \\ 0 \end{bmatrix} = \begin{bmatrix} 0 \\ v \cdot \omega \\ 0 \end{bmatrix} \tag{4.7}$$

They are expressed in the R_{ICR} reference frame and written in function of the robot longitudinal and angular velocities and accelerations $v, \dot{v}, \omega, \dot{\omega}$, since these are the variables that will be used to set the robot trajectories. The tangential acceleration coincides with the robot longitudinal acceleration $\dot{v}$.

For the second rotation, the chosen non-inertial reference frame R_a has the origin in the robot logic centre, the x axis on the robot longitudinal axis and the y axis on the wheels' main axis. It is integral with the robot and rotates of $\omega = [0; 0; \omega]$ with respect to an inertial reference frame having the same origin. Now, the parts mass centres are considered in their real positions, expressed in (4.8) with respect to R_a. Vector r_b refers to the robot base mass centre position in R_a, r_{rw} to the right wheel, r_{rf} to the left wheel and r_{uv} to the upper volume. The geometric parameters values that define the parts positions are listed in Appendix and shown in Figures 4.1a and 4.1b where stylized drawings of the robot are given.

$$r_b = \begin{bmatrix} d \\ 0 \\ 0 \end{bmatrix} \quad r_{\text{rw}} = \begin{bmatrix} 0 \\ -b_1 \\ 0 \end{bmatrix} \quad r_{\text{fw}} = \begin{bmatrix} 0 \\ b_1 \\ 0 \end{bmatrix} \quad r_{\text{uv}} = \begin{bmatrix} d + x_m \\ y_m \\ z_m \end{bmatrix} \tag{4.8}$$

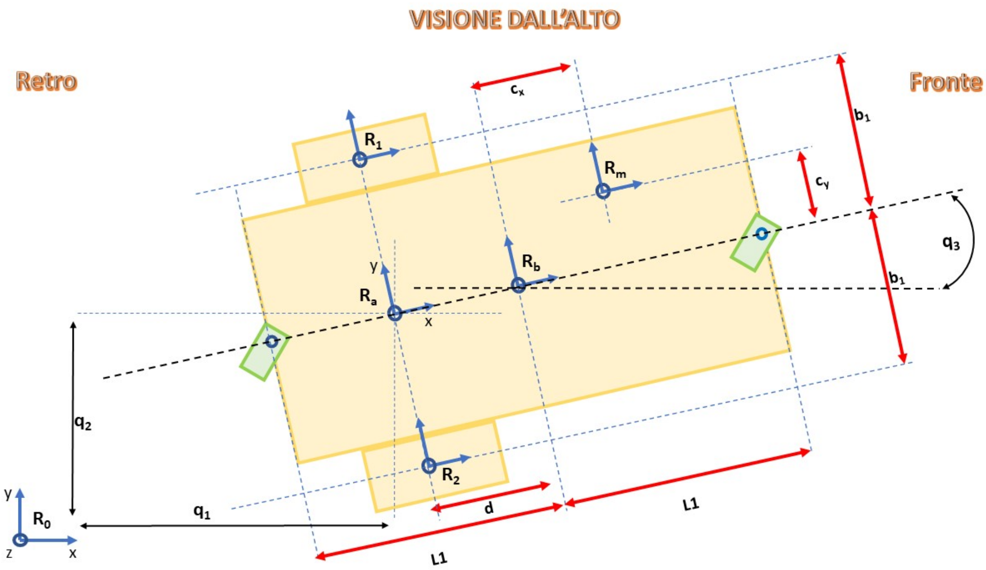

(a) *Robot view from above*

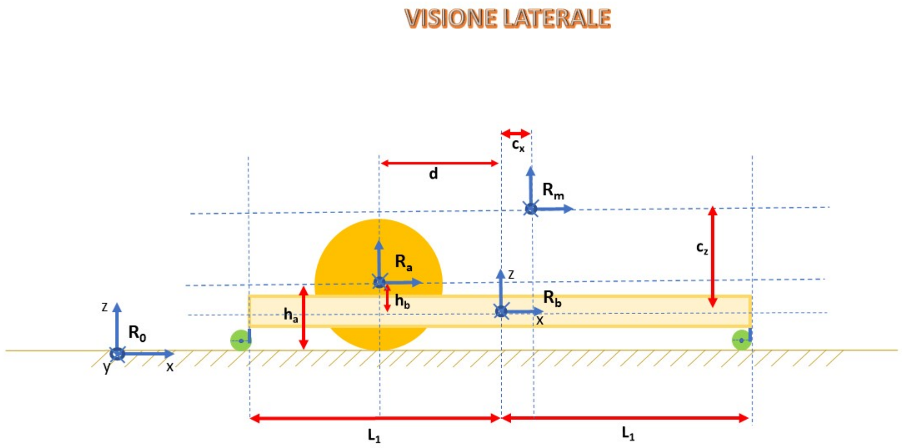

(b) *Robot lateral view*

Figure 4.1: Robot views

Therefore, the centripetal and inertial accelerations of each part can be computed and expressed in the R_a reference frame as follows:

$$a_{\mathrm{Cb}} = \begin{bmatrix} -d \cdot \omega^2 \\ 0 \\ 0 \end{bmatrix} \quad a_{0\mathrm{b}} = \begin{bmatrix} 0 \\ d \cdot \dot{\omega} \\ 0 \end{bmatrix} \tag{4.9}$$

$$a_{\mathrm{Cuv}} = \begin{bmatrix} -(d + x_m) \cdot \omega^2 \\ -y_m \cdot \omega^2 \\ 0 \end{bmatrix} \quad a_{0\mathrm{uv}} = \begin{bmatrix} -y_m \cdot \dot{\omega} \\ (d + x_m) \cdot \dot{\omega} \\ 0 \end{bmatrix} \tag{4.10}$$

$$a_{\mathrm{Crw}} = \begin{bmatrix} 0 \\ b \cdot \omega^2 \\ 0 \end{bmatrix} \quad a_{0\mathrm{rw}} = \begin{bmatrix} 0 \\ b \cdot \dot{\omega} \\ 0 \end{bmatrix} \tag{4.11}$$

$$a_{\mathrm{Cfw}} = \begin{bmatrix} 0 \\ -b \cdot \omega^2 \\ 0 \end{bmatrix} \quad a_{0\mathrm{fw}} = \begin{bmatrix} 0 \\ -b \cdot \dot{\omega} \\ 0 \end{bmatrix} \tag{4.12}$$

Reference frames R_1 and R_2 are parallel since the two rotations occur simultaneously with the same angular velocity ω, therefore the total acceleration acting on each part is computed by summing the two contributions coming from the first rotation with the two contributions of the second rotation. Then, multiplying the total acceleration for the corresponding mass the apparent forces are found.

$$a_b = \begin{bmatrix} \dot{v} - d \cdot \omega^2 \\ \omega \cdot v + d \cdot \dot{\omega} \\ 0 \end{bmatrix} \quad a_{\mathrm{uv}} = \begin{bmatrix} \dot{v} - (d + x_m) \cdot \omega^2 - y_m \cdot \dot{\omega} \\ \omega \cdot v - y_m \cdot \omega^2 + (d + x_m) \cdot \dot{\omega} \\ 0 \end{bmatrix} \tag{4.13}$$

$$a_{\mathrm{fw}} = \begin{bmatrix} \dot{v} - b \cdot \dot{\omega} \\ \omega \cdot v - b \cdot \omega^2 \\ 0 \end{bmatrix} \quad a_{\mathrm{rw}} = \begin{bmatrix} \dot{v} + b \cdot \dot{\omega} \\ \omega \cdot v + b \cdot \omega^2 \\ 0 \end{bmatrix} \tag{4.14}$$

The reference frame chosen to compute the moments balance equations of each part is integral with the considered part and centred in its mass centre. In this way, the inertial forces have null arm and do not appear in the equations. All the vectors referring to the torques, forces, forces' arms and the part angular velocity have to be expressed into the chosen reference frame. Of course, also the inertia matrix refers to the chosen reference frame and for this reason the principal reference frame is the best choice to have a diagonal inertia matrix.

4.3 Mechanical transmission line

Between each driving motor and the corresponding wheel an angular gearbox is present. The transmission line is characterized by a total inertia moment (J_{tot}) that includes the rotor inertia of the motor (J_{mot}), the gearbox inertia (J_{rid}) and the inertia of the wheel (J_w). Both the motor and the gearbox can be modelled as concentrated elements. This technique allows to distinguish the three aspects that mainly characterize each of them. The first aspect is the ideal behaviour, the second one is the inertia description, while the third one refers to the inner friction. The gearbox model has the friction (τ_{ag}) and inertia (J_{rid}) elements connected to the input shaft of the ideal gearbox element. Therefore, friction and inertia values refer to the input shaft side. The inertia value at its input shaft is equal to $J_{\text{rid}} = 1.387 \cdot 10^{-4}\ Kg \cdot m^2$. The motor model has the motor friction (τ_{am}) and inertia (J_{mot}) elements connected to the output shaft of the ideal motor element. The inertia moment at its output shaft is equal to $J_{\text{mot}} = 1.890 \cdot 10^{-4}\ Kg \cdot m^2$.

The wheel inertia element is connect to the output shaft of the ideal gearbox and is equal to $J_w = 40 \cdot 10^{-4}\ Kg \cdot m^2$. The model of the whole transmission line system is shown in Figure 4.2, where τ_m is the torque provided by the ideal motor. The value of the torque τ_m is equal to the product of the motor stator current and the motor torque constant.

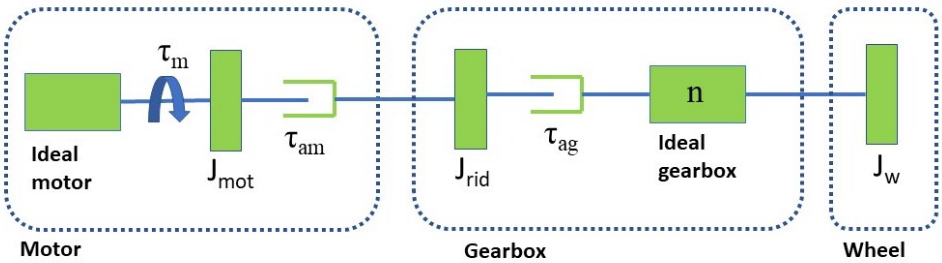

Figure 4.2: Transmission line

In order to compute the total inertia, the three inertia elements have to be placed at the same side of the ideal gearbox element. The goal is to move all the friction and inertia blocks to the ideal gearbox output shaft, therefore their values must be corrected taking into account the gearbox ratio n. The transmission line with all the elements moved at the gearbox output shaft is shown in Figure 4.3.

In order to perform this translation, a brief description of an ideal gearbox is required. An ideal gearbox has unitary efficiency and no backlash. Unitary efficiency means that no losses occur inside the reducer and therefore that the input mechanical power (P_{in}) is equal to the output one P_{out}, where T_{in} and T_{out} are the torques respectively at the input and output shafts. The gearbox input

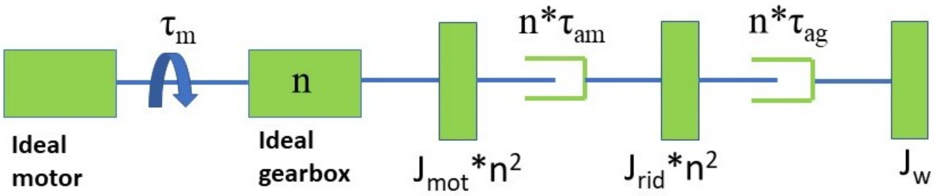

Figure 4.3: Transmission line

shaft angular speed $\dot{\phi}_{\text{in}}$ is equal to the motor shaft angular speed $\dot{\theta}_m$, while the one of the output shaft is equal to the corresponding wheel angular speed $\dot{\theta}$.

$$P_{\text{in}} = T_{\text{in}} \cdot \dot{\phi}_{\text{in}} = T_{\text{out}} \cdot \dot{\phi}_{\text{out}} = P_{\text{out}} \tag{4.15}$$

If no backlash is present, the tangential velocities of the two gearbox wheels can be considered always equal $v_{\text{in}} = v_{\text{out}} = v_t$. R_{in}, where R_{out} are, respectively, the input wheel radius and the output wheel radius.

$$v_t = \dot{\phi}_{\text{in}} \cdot R_{\text{in}} = \dot{\phi}_{\text{out}} \cdot R_{\text{out}} \tag{4.16}$$

Under these assumptions, the equations in (4.17) represent the relation between the input and output physical quantities, where J_{in} is the value of a generic inertia at the gearbox input shaft and J_{out} the value of the same inertia moved to the output shaft.

$$\begin{cases} n = \frac{R_{\text{in}}}{R_{\text{out}}} = \frac{\phi_{\text{in}}}{\phi_{\text{out}}} = \frac{T_{\text{out}}}{T_{\text{in}}} \\ J_{\text{out}} = J_{\text{in}} \cdot n^2 \end{cases} \tag{4.17}$$

At this point, the total inertia moment J_{tot} and the total friction torque τ_a of the transmission line can be computed as (4.18), thus obtaining the final model in Figure 4.4.

$$\begin{cases} J_{\text{tot}} = J_w + n^2 \cdot J_{\text{mot}} + n^2 \cdot J_{\text{rid}} \\ \tau_a = n \cdot \tau_{\text{am}} + n \cdot \tau_{\text{ar}} \end{cases} \tag{4.18}$$

From Figure 4.4, the equation of the transmission line can be easily written (4.19). Since the wheel is in contact with the ground, the moment of the traction force (f_{cx}) must be considered, since it opposes the wheel rotation. The traction force is the force exerted on the wheel at the wheel-ground contact point along the wheel longitudinal direction. The traction force arm is the wheel radius R.

$$J_{\text{tot}} \cdot \ddot{\theta} = n \cdot \tau_{\text{m}} - \tau_{\text{a}} - R \cdot f_{\text{cx}} \tag{4.19}$$

Substituting the motor torque at the wheel side, $n \cdot \tau_{\text{m}}$, with the value $-\tau_{\text{ty}}$, the equation (4.20) is found and shown in Figure 4.5.

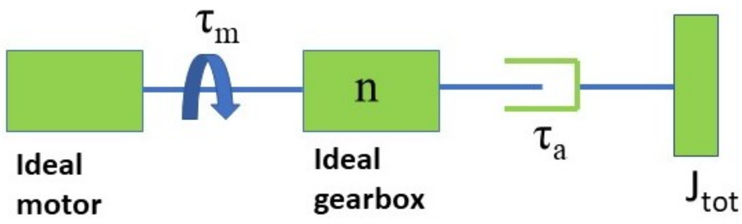

Figure 4.4: Transmission line

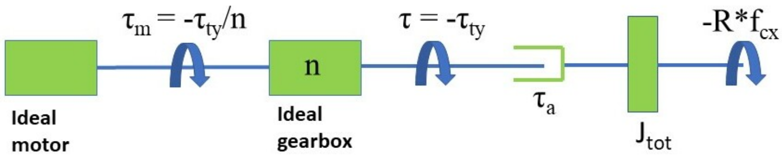

Figure 4.5: Transmission line

$$J_{tot} * \ddot{\theta} = -\tau_{ty} - \tau_a - R * f_{cx} \tag{4.20}$$

Finally substituting the expression of J_{tot} given in (4.18), the final equation (4.21) is found.

$$\{J_w + n^2 \cdot J_{mot} + n^2 \cdot J_{rid}\} \cdot \ddot{\theta} = -\tau_{ty} - \tau_a - R \cdot f_{cx} \tag{4.21}$$

The equations in (4.22) can be seen as the wheels moments balance equations, where the motors and gearboxes inertias have been added to the wheel inertias. Therefore, they will be inserted in the wheels equations.

$$\begin{cases} \{J_w + n^2 \cdot J_{mot} + n^2 \cdot J_{rid}\} \cdot \ddot{\theta}_1 = -\tau_{ty1} - \tau_{a1} - R \cdot f_{cx1} \\ \{J_w + n^2 \cdot J_{mot} + n^2 \cdot J_{rid}\} \cdot \ddot{\theta}_2 = -\tau_{ty2} - \tau_{a2} - R \cdot f_{cx2} \end{cases} \tag{4.22}$$

Since the transmission line is in contact with the robot base, a reaction torque on the base τ_{reac} must be considered. It can be considered equal to the torque of the traction force.

$$\tau_{reac} = -R * f_{fcx} \tag{4.23}$$

4.4 Inverse dynamic problem solution

During simulations, at each time step, the inverse dynamic problem of the robot equations is solved. The equations can be found in Appendix A (A.3), together with the reference frames used to describe the whole system (A.1), the homogeneous matrices linking the different reference frames (A.4), the forces exchanged between the different robot parts and the external forces (A.2). All the reference frames have the z axis perpendicular to the ground plane thanks to the planar motion approximation, and can be seen intuitively in Figures 4.1a and 4.1b.

The kinematic inputs of the inverse dynamic problem are $v, \dot{v}, \omega, \dot{\omega}$ that completely describe the desired robot trajectory. The forces inputs are the bearings friction torques ($\tau_{\mathrm{a1y}}, \tau_{\mathrm{a2y}}$), the vertical contact friction torques ($\tau_{\mathrm{c1z}}, \tau_{\mathrm{c2z}}$) and the forces and torques exchanged with the eventual library the robot is pulling ($f_{\mathrm{tLx}}, f_{\mathrm{tLy}}, \tau_{\mathrm{tLz}}$).

The driving wheels bearings friction torques ($\tau_{\mathrm{a1y}}, \tau_{\mathrm{a2y}}$) and the vertical contact friction torques ($\tau_{\mathrm{c1z}}, \tau_{\mathrm{c2z}}$) are computed using the same Adams model described in Chapter 3. Therefore, each driving wheel contact friction torque computation requires the knowledge of the vertical reaction force ($f_{\mathrm{c1z}}; f_{\mathrm{c2z}}$) at the wheel contact point, while each bearing friction torque computation requires the knowledge of the corresponding axial force ($f_{\mathrm{t1y}}, f_{\mathrm{t2y}}$) and of the radial forces ($f_{\mathrm{t1x}}, f_{\mathrm{t1z}}, f_{\mathrm{t2x}}, f_{\mathrm{t2z}}$) at the revolute joint. The problem is that these forces are outputs of the system. To solve this problem, at each time step, the friction torques are computed using the forces obtained in the previous time step. In this way, a delay is introduced but the results are acceptable.

The forces and torques exchanged with an eventual library pulled by the robot come out from the solution of the library inverse dynamic problem. Simple equations of a library will be found in the next section.

Instead the output force and torques are listed in (4.24).

$$
\begin{aligned}
x = \big[&f_{\mathrm{c1x}}, f_{\mathrm{c1y}}, f_{\mathrm{c1z}}, f_{\mathrm{c2x}}, f_{\mathrm{c2y}}, f_{\mathrm{c2z}}, f_{\mathrm{t1x}}, f_{\mathrm{t1y}}, f_{\mathrm{t1z}}, \\
&\tau_{\mathrm{t1x}}, \tau_{\mathrm{t1y}}, \tau_{\mathrm{t1z}}, f_{\mathrm{t2x}}, f_{\mathrm{t2y}}, f_{\mathrm{t2z}}, \tau_{\mathrm{t2x}}, \tau_{\mathrm{t2y}}, \tau_{\mathrm{t2z}}, \\
&f_{\mathrm{t3z}}, f_{\mathrm{tmx}}, f_{\mathrm{tmy}}, f_{\mathrm{tmz}}, \tau_{\mathrm{tmz}}\big]^T
\end{aligned} \tag{4.24}
$$

Relevant unknowns are for sure the driving torques that have to be applied to the wheels $\tau_1 = -\tau_{\mathrm{t1y}}$ and $\tau_2 = -\tau_{\mathrm{t2y}}$. These two torques ($\tau_1, \tau_2$) are the ones required at the output shafts of the reducers. The friction torques at the reducers bearings are already taken into account into the equations. Therefore, dividing the obtained torques for the reducers ratio n, the torques $\tau_{\mathrm{m1}} = \tau_1/n$ and $\tau_{\mathrm{m2}} = \tau_2/n$ that the motors have to provide at their output shafts are found. The other important unknowns are the contact forces at the wheels contact points ($f_{\mathrm{c1x}}, f_{\mathrm{c1y}}, f_{\mathrm{c1z}}, f_{\mathrm{c2x}}, f_{\mathrm{c2y}}, f_{\mathrm{c2z}}$) that are necessary to check if the robot is sliding or not along the desired trajectory.

The equations (A.3) refer to a differential drive robot having only one castor wheel. If $L1 = 22.75\ cm$, the robot has the castor wheel in the back while if $L1 = -22.75\ cm$, the castor is in the front. The two models are simulated simultaneously and both return the unknown variables. The correct unknown variables are the ones coming from the model that has its castor wheel in contact with the ground. The unknown variable f_{t3z} is the normal reaction force at the castor wheel contact point and allows to know if the castor is or not in contact with the ground. If the force f_{t3z} is positive, the castor is in contact with the ground, otherwise the force is negative. When the force coming from one model is positive, the one from the other model is negative. Checking with a proper function in Simulink, at each time step, the values of $f_{\mathrm{t3z}}^{\mathrm{front}}$ and $f_{\mathrm{t3z}}^{\mathrm{rear}}$, the model returning the correct unknown variables is found.

The key aspect of this model is its modularity in order to simulate systems made of a wheeled mobile robot and a library it is pulling. Now that the robot equations have been found, the equations of the library it has to pull are needed. The first step consists in solving the inverse dynamic model of the library to find the forces and torques needed to pull it along the desired trajectory. In the second step, the previous forces are given to the inverse dynamic model of the robot that is solved. In the third step, from the driving wheels contact forces it can be checked if the robot is slipping/sliding or not along the desired trajectory.

4.5 Library models

In a wheeled mobile robot, castor wheels are usually used when additional contact points with the ground are needed to split the upper weight. In these cases, castor wheels are not actuated. Due to the distance between the vertical secondary axis and the wheel centre, they are self aligning. From a kinematic point of view, the alignment is instantaneous therefore it does not affect the robot motion. From a dynamic point of view, the alignment perturbs the robot motion due to the forces and torques exchanged with the robot base.

In Agilino it is supposed that only one castor is in contact with the ground at each instant. The contact normal forces at the two castors change during motion and the transition from a pure rolling motion to a sliding motion can occur. When the robot accelerates longitudinally, the front castor normal force reduces. Supposing it does not become zero, the front castor remains in contact with the ground, but the maximum static friction force that the ground can exert on the wheel reduces. This can cause the transition to sliding motion and disturb the robot motion. Since Agilino mechanical design tries to place the upper volume mass centre exactly on the vertical axis passing through the logic centre, the castors normal forces are quite small. Indeed, most of the robot weight is sustained by the driving wheels. For this reason the castors are neglected in the mathematical model.

Instead, in differential drive robots that just have the rear or the front castor wheel, the castor equations have to be inserted. Indeed, the castor have to be always in contact with the ground and it must never transit from pure rolling motion to sliding motion. Trajectories that guarantee to the castor wheel a pure rolling motion must be selected and the robot model is fundamental for this selection. The castor equations allow also to understand where it is better to place the wheel on the robot base to reduce the perturbation due to its alignment. For example, increasing the castor distance form the driving axis, the alignment angular velocity increases steeper and consequently the magnitude of the forces needed to bring it into alignment.

As in differential drive robots with just one castor, also in the library model the castor wheels should not be omitted since they must never slide. Using a very simple description, a library is made of a rectangular base on four castor wheels. Since the initial positions of the library castors are not known, a model that takes them into account could help in the choice of an initial trajectory that brings them slowly into alignment, supposing, for example, the worst castor initial orientation that is the one opposite to the motion direction. When neither lateral slide nor longitudinal slip occur, the castor wheel motion can be approximated with two rotations, one around its main axis and the other one around the vertical axis passing through its contact point with the ground.

In this chapter, a very simple model of a library is developed. As said before, its goal is to find the forces that Agilino has to transmit to the library to move it along the desired trajectory. Therefore, the inverse dynamic problem of the library equations has to be solved. To move the library, Agilino goes under its base and extracts a vertical rod that connects to the library base. The connection can be imagined like a rod/hole one. The analysis of the connection mechanical design is out of the purposes of this thesis. The only relevant thing is the number of degrees of freedom that this connection constrains.

The simplest connection is a vertical revolute joint that allows the rotation of the robot cylindrical rod into the library hole. Therefore, only the planar translation is transmitted, while the orientation of the library is decoupled from the one of the robot. Leaving the orientation of the library free to evolve does not seem a good idea. Nevertheless, a library with an axial symmetrical section should be used in this case, so that the library orientation is irrelevant with respect to the occupied size around the robot. For example, a circular or a quadratic section concentric to the robot rod axis can be adopted.

A connection that tries to transmit also the rotation would be better such as a rod with a squared section. This connection results in heavy torsional stresses on the robot rod that must be designed properly. The library model will return the vertical torque transmitted and therefore will help the mechanical engineer to choose the rod material and the dimension of the rod section to make it survive for many fatigue cycles. This connection requires a huge and not practical section for the robot rod, therefore other solution can be studied.

A first solution not to have a torsional stress on the robot rod is to use two cylindrical rods that connect to two library base holes through vertical revolute joints. The first rode transmits the forces that make the library translate, while the two rods together apply the vertical moment that fixes the library orientation with respect to the robot one. In this way, only the bending stress on the two rods is present. The connection complexity reduces but one more motor and one more rack are needed to extract the second rod vertically.

After this simple discussion about the robot-library connection, it is possible to conclude that the study of other solutions can start from the forces and torques, provided by the solution of the library inverse dynamic problem, that must be applied to the library to make it move along the desired trajectory.

Since the library has its own wheels, its weight does not increase the normal reaction forces at the robot driving wheels, while the friction forces at their contact points increase. Therefore, the risk of having the driving wheels slipping or sliding increases. Hence, thanks to a simple library model, it is possible to find the maximum mass that can be transported on the library and the safe trajectories that the robot can follow.

Two library models will be found. In the first model, the planar motion approximation is considered and the vertical dynamic is neglected. In this way, the library is considered a bidimensional object without the vertical dimension, therefore its equations include only the two forces balances on the plane axes and the moment balance around the axis perpendicular to the plane. This first model is the simplest one but maybe the most effective. It considers the system made of the library and its payload described by one mass m_L, one vertical inertia moment I_{Lzz} and one mass centre position $r_{\mathrm{mL}}^{\mathrm{RL}} = (x_{\mathrm{mL}}, y_{\mathrm{mL}})$, expressed in reference frame R_L. Reference frame R_L has the origin in the point where the robot rod is in contact with the library, its x axis is parallel to the robot longitudinal axis while its y axis to the driving wheels main axis. It is listed among the robot reference frames (A.1).

The library castor wheels are supposed to be instantaneously self aligning, therefore the only forces acting on the mass are the ones exchanged with the robot. The equations are given in (4.25) and are written in the reference frame R_{mL}, whose origin is in the library mass centre as shown in Figure 4.6a. Applying the desired trajectory and solving the inverse dynamic problem, the values of the forces that the robot applies to the library $(f_{\mathrm{Lx}}, f_{\mathrm{Ly}}, \tau_{\mathrm{Lz}})$ are found. To find the forces that the library applies to the robot $(f_{\mathrm{tLx}}, f_{\mathrm{tLy}}, \tau_{\mathrm{tLz}})$, equations (4.26) are used.

The apparent forces acting on the library are found easily since it can be considered integral to the robot due to the squared rod connection. Therefore, the library motion can be split in two simultaneous vertical rotations. The first one occurs around the instantaneous centre of rotation and approximates the library mass in the robot logic centre. The second one occurs around the robot logic centre and considers the library mass in its real position $r_{\mathrm{mL}}^{\mathrm{Ra}} = (x_L + x_{\mathrm{mL}}, y_{\mathrm{mL}}, y_L + y_{\mathrm{mL}})$ with respect to the logic reference frame R_a. The coordinates (x_L, y_L) refers to the position of the rod axis with respect to R_a.

$$
\begin{cases}
m_L \cdot \{\dot{v} - (y_L + y_{\mathrm{mL}}) \cdot \dot{\omega} - (x_L + x_{\mathrm{mL}}) \cdot \omega^2\} = f_{\mathrm{Lx}} + g_1 \cdot m_L \\
m_L \cdot \{v \cdot \omega - (y_L + y_{\mathrm{mL}}) \cdot \omega^2 + (x_L + x_{\mathrm{mL}}) \cdot \dot{\omega}\} = f_{\mathrm{Ly}} + g_2 \cdot m_L \\
I_{\mathrm{Lzz}} \cdot \dot{\omega} = \tau_{\mathrm{Lz}} - x_{\mathrm{mL}} \cdot f_{\mathrm{Ly}} + y_{\mathrm{mL}} \cdot f_{\mathrm{Lx}}
\end{cases} \tag{4.25}
$$

$$
\begin{cases}
f_{\mathrm{tLx}} = -f_{\mathrm{Lx}} \\
f_{\mathrm{tLy}} = -f_{\mathrm{Ly}} \\
\tau_{\mathrm{tLz}} = -\tau_{\mathrm{Lz}}
\end{cases} \tag{4.26}
$$

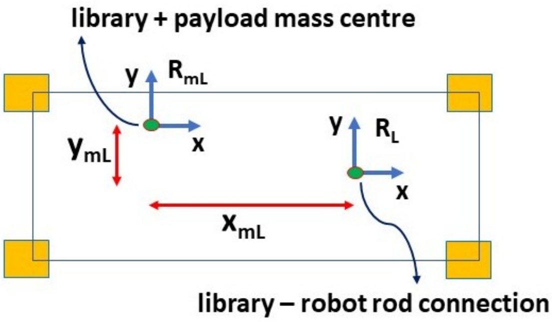

(a) *Library top view with reference frames.*

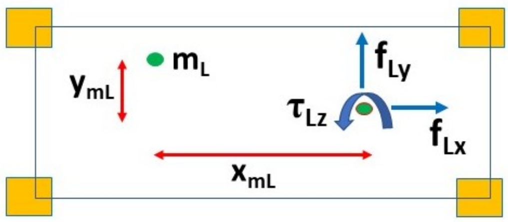

(b) *Library top view with the forces applied by the robot rod.*

Figure 4.6: Library top view.

If the robot rod axis is coincident with the vertical axis passing through the robot logic centre (x_L, y_L) = (0,0) and the library mass centre is close to the connection point $(x_{\mathrm{mL}}, y_{\mathrm{mL}})$ = (0,0), the transversal component of the force f_{tLy} is not actively provided by the robot, indeed the driving wheels oppose naturally the lateral movement of the robot and therefore of the library. Instead, the vertical torque τ_{tLz} and the longitudinal component of the force f_{tLx} are related to the traction forces $(f_{\mathrm{c1x}}, f_{\mathrm{c2x}})$ at the driving wheels, therefore actively provided.

The second model is more complex since it is realized on Adams to be simulated with the Adams model of the robot in the future works after this thesis. The Adams library model is shown in Figures 4.7a and 4.7b.

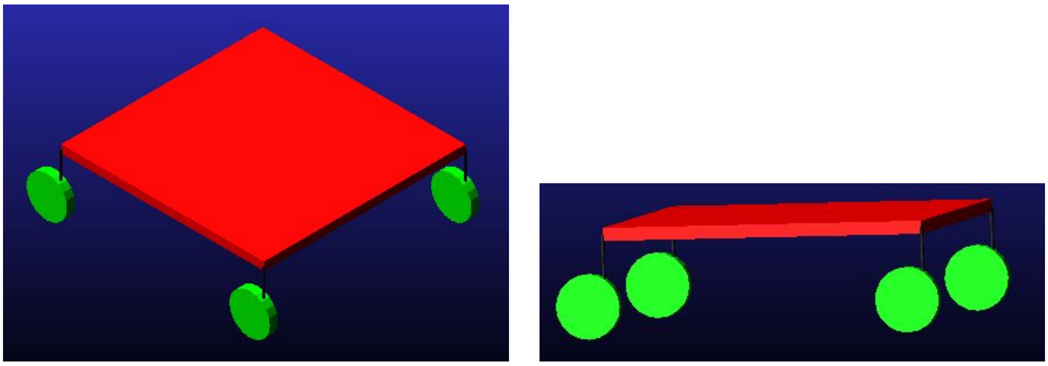

(a) (b)

Figure 4.7: Adams library model

Chapter 5

Comparison with the Adams model

In this chapter, simulations of the models will be performed for some trajectories considered of interest. These trajectories are selected according to the simulations' purposes. The goal is the validation of the mathematical model with respect to the Adams one that is considered the most reliable. The refinement goes on up to when the mathematical model behaviour is with good approximation close to the Adams model one. From that moment on, since the two models act the same, only the mathematical one can be used.

As said in the introduction, the differential mobile robot has a degree of manoeuvrability equal to $\delta_M = 2$, a degree of mobility equal to $\delta_m = 2$ and of course a null degree of steer ability due to the absence of actuated orientable wheels. Therefore, only the time evolution of two velocities must be set to fix a trajectory. These two velocities could be the angular velocities of the two wheels $[\dot{\theta}_1, \dot{\theta}_2]$ or the tangential v and the angular velocities ω of the robot logic centre LC with respect to the instantaneous centre of rotations ICR. The latter solution is chosen since it is straightforward.

5.1 Mathematical model refinement

The mathematical model and the Adams model are simulated together in the Simulink platform. Adams allows to export the model into the Simulink environment. As it can be seen in Figure 5.1, the Simulink file is characterized by three main subsystems: the trajectories generator, the mathematical inverse dynamic model and the Adams direct dynamic model.

In the trajectories generator subsystem, the trajectory is fixed by setting the time evolution of the variables v and ω. The kinematic model of the differential drive robot is exploited to compute the wheels angular velocities $[\dot{\theta}_1, \dot{\theta}_2]$ and accelerations

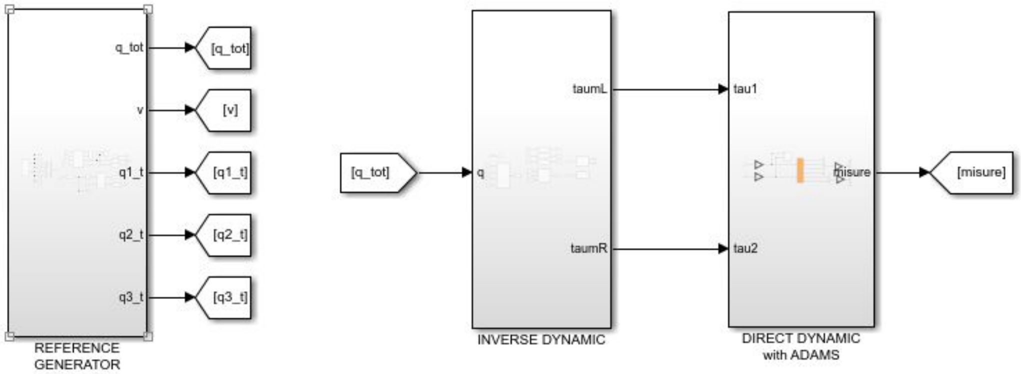

Figure 5.1: Simulink structure for simulations.

$[\ddot{\theta}_1, \ddot{\theta}_2]$ as:

$$\begin{cases} \dot{\theta}_1 = \frac{v - b_1 \cdot w}{R} \\ \dot{\theta}_2 = \frac{v + b_2 \cdot w}{R} \end{cases} \tag{5.1}$$

The kinetic variables $v, \dot{v}, \omega, \dot{\omega}, \dot{\theta}_1, \dot{\theta}_2, \ddot{\theta}_1, \ddot{\theta}_2$ are needed to solve the inverse dynamic problem, therefore they are passed to the mathematical model subsystem.

The robot posture velocities $[\dot{q}_1(t), \dot{q}_2(t), \dot{q}_3(t)]$ are needed to find the evolution of the robot position $[q_1(t), q_2(t)]$ and orientation $q_3(t)$ in the plane, starting from an initial posture that is for simplicity chosen as $[0; 0; 0]$. The robot orientation rate of change $\dot{q}_3(t)$ is equal to the robot angular velocity ω.

$$\begin{cases} \dot{q}_1(t) = v \cdot \cos(q_3(t)) \\ \dot{q}_2(t) = v \cdot \sin(q_3(t)) \\ \dot{q}_3(t) = \omega \end{cases} \tag{5.2}$$

The solution of the inverse dynamic problem returns the torques that must be applied to the driving wheels to follow the ideal desired trajectory. The other important outputs of the mathematical model are the forces exchanged between each wheel and the ground in order to check if the wheels are slipping/sliding or not. Then, the computed torques are given as inputs to the Adams direct dynamic model that returns the position and orientation time evolutions of the robot logic centre during motion. In this way the real motion is compared with the ideal one. If they are different, it means that the mathematical model is not coherent with the Adams one. Indeed, the torques that the mathematical model provides to make the robot follow the ideal path would result into a different path. A refinement work has to be performed looking at the possible differences from the mechanical description point of view (masses and inertia moment), from the friction modelling point of view and of course thinking about the dynamical aspects that could have been neglected in the mathematical model.

In the following, the tests are reported in the order they have been performed. The order is important because it allows to discover what has to be refined step by step.

Test 1 The first test is without motion. In this way the position of the upper volume mass centre in the mathematical model is refined by comparing the normal forces at the wheels contact points. Since the mass centre is in the front part of the robot, the front castor wheel is the one in contact with the ground. In the Adams model, the three normal forces are $f_{\mathrm{c1z}} = 296.72\ N$, $f_{\mathrm{c2z}} = 313.29\ N$, $f_{\mathrm{c3z}} = 33.5\ N$, where 1 refers to the left wheel, 2 to the right wheel and 3 to the castor in contact with the ground at a certain instant. The total weight force is 643.51 N that corresponds to a total mass of 65.6 Kg. The ratios between the normal forces and the total weight are $r_1 = 46.1\%$, $r_2 = 48.7\%$ and $r_3 = 5.2\%$. In the mathematical model, the three normal forces are $f_{\mathrm{c1z}} = 296.3\ N$, $f_{\mathrm{c2z}} = 312.8\ N$, $f_{\mathrm{c3z}} = 30.75\ N$. The total weight force is 639.85 N so the total mass is 65.2 Kg. The 0.4 Kg lag between the Adams model and the mathematical one is due to the absence of the two castor wheels weight in the mathematical one. Indeed, each castor weight is 0.2 Kg. The ratios are $r_1 = 46.3\%$, $r_2 = 48.9\%$ and $r_3 = 4.8\%$. Comparing the ratios, it can be seen that the longitudinal distance of the mathematical model mass centre from the logic centre is lower than the one of the Adams model. Of course, the difference is acceptable.

Test 2 and 3 The second and the third tests check the straight motion. The robot angular velocity ω_{nom} is always zero while the longitudinal velocity v_{nom} has a trapezoidal shape. The trapezoidal shape of the velocity results into a discontinuous longitudinal acceleration $\dot{v}_{\mathrm{nom}}$ that is characterized by step variations. It is not a real profile that the controller will try to follow but it can be tuned easily and in a fast way. A 2-1-2 profile for the velocity would be more realistic but its tuning is slower, since also the jerk must be set and the conditions not to have a bang bang trajectory in the accelerations must be considered. This profile will not be used even though the acceleration is continuous having a trapezoidal shape. In test 2, v_{nom} changes from 0 m/s to 0.1 m/s with an acceleration of $\dot{v}_{\mathrm{nom}} = 0.25\ m/s^2$, stays at 0.1 m/s for a predefined period of time $\Delta t = 6s$ and then goes back to zero with a deceleration of $\dot{v}_{\mathrm{nom}} = -0.25\ m/s^2$. In test 3, the only difference is that the longitudinal velocity v_{nom} that the robot has to reach changes from 0.1 m/s to 1.0 m/s.

As it can be seen in Figures 5.2a and 5.2b, the Adams model motion is not perfectly straight but the error is negligible. Indeed, in test 2 the final posture of the robot is $(q_1, q_2) = (1.8, -12 \cdot 10^{-4})m$, while in test 3 is $(q_1, q_2) = (18, -0.05)m$. In both tests, the final posture coordinate q_2 is negligible with respect to q_1. Some

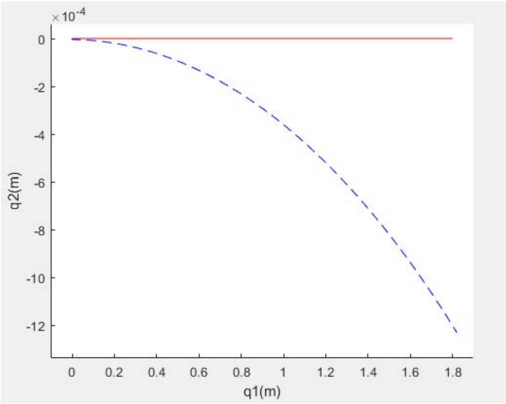

(a) *Test 2: the red line is the nominal trajectory while the blue one the real trajectory that the Adams model makes.*

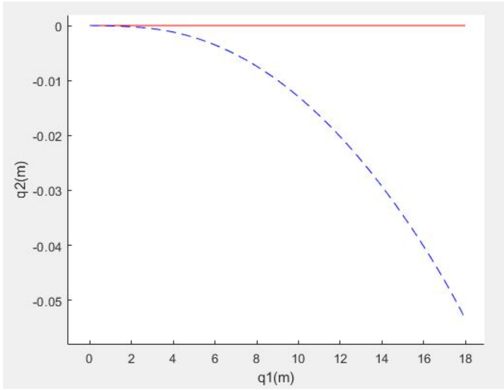

(b) *Test 3: the red line is the nominal trajectory while the blue one the real trajectory that the Adams model makes.*

Figure 5.2: Test 2 and 3

considerations will be done referring to the results of test 3 simulations, but the same assertions are valid for test 2 as well. The longitudinal velocity measured in Adams v_{mis} and the ideal profile generated in Simulink v_{nom} are compared in Figure 5.3a. These two tests confirm again that the upper volume mass centre is well placed in the mathematical model. Indeed, to drive the robot straight, the right torque τ_2 must be greater than the left one τ_1, as shown in Figure 5.3c, in order to compensate during the acceleration phase the negative vertical moment created by the arm $y_{\text{m}} = -7.3\ mm$ with the inertial force $M_m \cdot \dot{v}$. As can be seen in Figure 5.3d, the traction forces are zero in the constant phase since the driving torques just have to compensate the bearings friction torques without accelerating the robot. As can be seen in Figure 5.3b, the driving wheels normal forces increase in the acceleration phase while the normal force on the front castor reduces. The weight moves to the back during the acceleration phase but the front castor remains in contact with the ground even if lightened.

Test 4 In the fourth test, the dynamic behaviour in a turn is investigated. The trajectory used in this test is made of nine subsequent phases. Both the longitudinal velocity v_{nom} and the angular velocity ω_{nom} have a trapezoidal shape.

1. No motion phase: both v and ω are zero.
2. Longitudinal acceleration phase: v_{px} increases linearly from zero to $v_{\max} = 1.0$ m/s with a longitudinal acceleration of $\dot{v} = 0.25\ m/s^2$, while ω is zero.
3. First constant longitudinal velocity phase: v is constant at $v_{\max}$ while ω is still zero.
4. Angular acceleration phase: v is constant at $v_{\max}$ while ω linearly increases from zero to $\omega_{\max} = 0.35\ rad/s$ with a constant acceleration equal to $\dot{\omega} = 0.35$

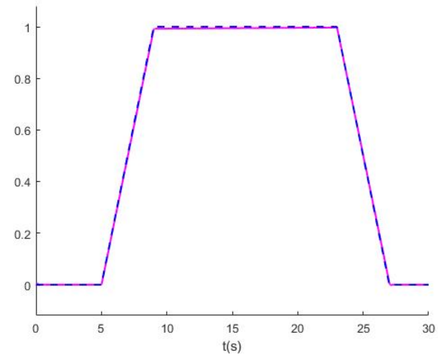

(a) *Test 3: longitudinal velocity v expressed in m/s. The blue line is the nominal longitudinal velocity v_{nom} while the magenta line is the measured one v_{mis}.*

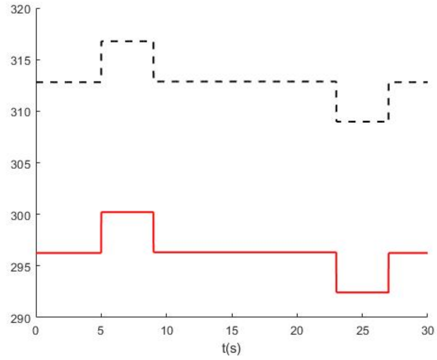

(b) *Test 3: normal forces at the driving wheels computed by the mathematical model and expressed in N. The black line refers to the right wheel normal force f_{c2x}, while the red one to the left wheel normal force f_{c1x}.*

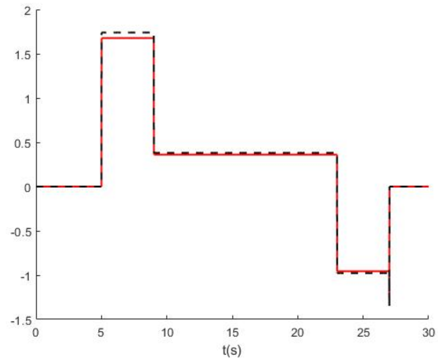

(c) *Test 3: driving torques at the wheel side computed by the mathematical model and expressed in $N * m$. The black line refers to the right wheel torque τ_2, while the red one to the left wheel torque τ_1.*

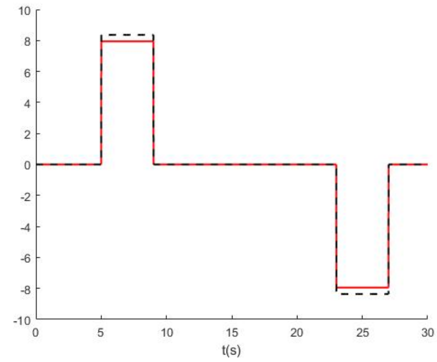

(d) *Test 3: traction forces computed by the mathematical model and expressed in N. The black line refers to the right wheel traction force f_{c2x}, while the red one to the left wheel traction force f_{c1x}.*

Figure 5.3: Test 3

rad/s^2.

5. Constant velocities phase: v and ω are both constant at $v_{\max}$ and $w_{\max}$ respectively. The turn radius is constant at the value $r_{\text{turn}} = v_{\max}/w_{\max}$.
6. Angular deceleration phase: v is constant at $v_{\max}$ and ω linearly decreases to zero with a constant deceleration equal to $\dot{\omega} = -0.35\ rad/s^2$.
7. Second constant longitudinal velocity phase: v is constant at $v_{\max}$ and ω is zero.
8. Longitudinal deceleration phase: v decreases linearly to zero with a constant deceleration of $\dot{v} = -0.25\ m/s^2$ while ω is zero.

9. Again a no motion phase.

Table 5.1: Test 4 velocities profile parameters

Quantity	Symbol	Unit measure	Value
maximum longitudinal velocity	$v_{\max}$	m/s	1.0
longitudinal acceleration/deceleration	$\dot{v}$	m/s^2	0.25
maximum angular velocity	$\omega_{\max}$	rad/s	0.35
angular acceleration/deceleration	$\dot{\omega}$	rad/s^2	0.35

In these trajectories the acceleration and deceleration phases of the longitudinal velocity v and of the angular velocity ω are kept separated. This is important in order to be able to understand in which phase the mathematical model behaviour differs from the Adams one. Indeed, many dynamical aspects that are hidden during the straight motion are triggered during a robot turn, such as the vertical friction torque at the wheels. Figure 5.4a shows that the torques computed by the mathematical model do not allow the Adams model to follow the desired trajectory.

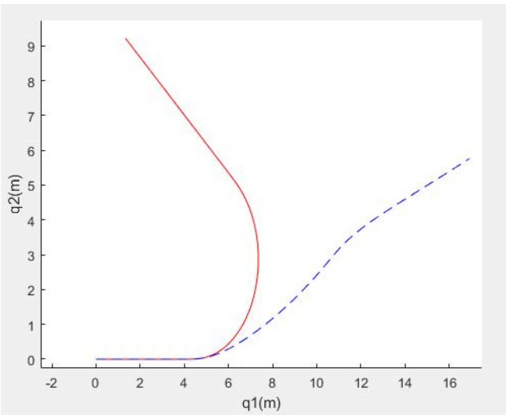

(a) *Test 4: the red line is the nominal trajectory while the blue one the real trajectory that the Adams model makes.*

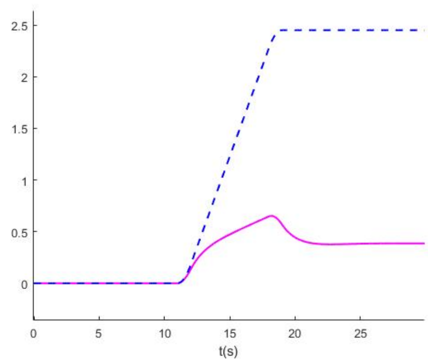

(b) *Test 4: posture orientation q_3 expressed in rad. The blue line is the nominal orientation $q_{3\mathrm{nom}}$ while the magenta line is the measured one on the Adams model $q_{3\mathrm{mis}}$.*

Figure 5.4: Test 4

To understand when the real trajectory starts moving away from the real one, Figures 5.5b and 5.5a, where the longitudinal and angular velocities nominal profile are compared with the measured ones, are analysed.

The measured angular acceleration $\dot{\omega}_{\mathrm{mis}}$ is smaller than the desired one $\dot{\omega}_{\mathrm{nom}}$, therefore at the end of the angular acceleration phase the angular velocity ω_{mis} is 0.24 rad/s instead of 0.35 rad/s. In addition, during the constant velocities phase,

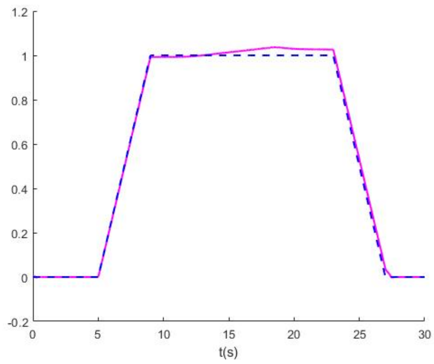

(a) *Test 3: longitudinal velocity v expressed in m/s. The blue line is the nominal longitudinal velocity v_{nom} while the magenta line is the measured one v_{mis}.*

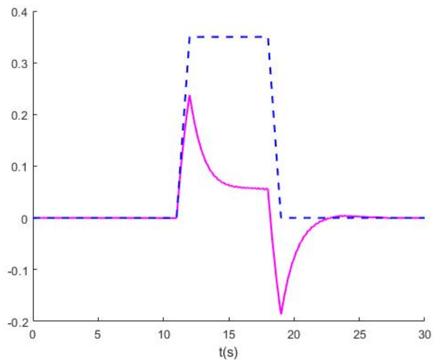

(b) *Test 3: angular velocity ω expressed in m/s. The blue line is the nominal angular velocity ω_{nom} while the magenta line is the measured one ω_{mis}.*

Figure 5.5: Test 4

the angular velocity ω_{mis} does not remain constant at the reached value but decreases and settles at the value of 0.055 rad/s. Always in the constant velocities phase, the longitudinal velocity v_{mis} increases instead of remaining constant. Therefore, the turn radius that should remain constant in the constant velocities phase increases and the motion transits toward a straight motion. The angular velocity reduction and longitudinal velocity increase occur at the same time. And, when the angular velocity settles to the value, the longitudinal velocity keeps increasing. The robot behaves as if it is constrained into a rail. Therefore, the torques applied result into a longitudinal acceleration since the possibility to turn is violated. Something has been not considered in the mathematical model. The mass centre of the upper volume is well placed as it is known from the previous tests, therefore it is not a problem of centrifugal force moment that opposes the robot turn. Probably the vertical friction torques at the driving wheels contact points must be introduced. Up to this test, the friction coefficient was set to zero. The torques and traction forces of Test 4 are shown respectively in Figures 5.6a and 5.6b. The vertical torque friction coefficient μ_v must depend on the robot angular velocity ω that is the relative angular velocity of each wheel with respect to the ground around the vertical axis passing though the wheel centre.

Test 5a The first relation exploited in the mathematical model between ω and μ_v is the Coulomb one as suggested by the tests performed in Adams Chapter 7. Since the transition from static to dynamic friction occurs at very low ω, the friction coefficient μ_v is practically always equal to the dynamic one $\mu_d = 0.1$. Therefore, this relation results into a constant $\mu_v = \mu_d$ that does not depend on ω. Performing a simulation, the mismatch of this friction model with respect to

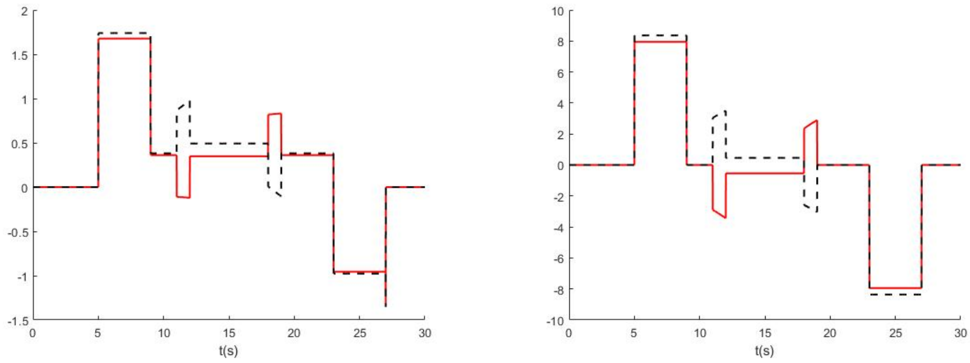

(a) *Test 4: driving torques at the wheel side computed by the mathematical model and expressed in $N*m$. The black line refers to the right wheel torque τ_2, while the red one to the left wheel torque τ_1.*

(b) *Test 4: traction forces computed by the mathematical model and expressed in N. The black line refers to the right wheel traction force f_{c2x}, while the red one to the left wheel traction force f_{c1x}.*

Figure 5.6: Test 4

the Adams one is found. The comparison between the measured angular velocity ω_{mis} and the nominal one ω_{nom} is shown in Figure 5.7b. At the beginning of the angular acceleration phase, the measured angular velocity ω_{mis} grows steeper than the nominal one ω_{nom}. This is probably because the vertical friction torques in the mathematical model are greater than the Adams ones at that low angular velocities. This results into higher driving torques and therefore into a higher angular acceleration of the Adams model. This is observable also in Figure 5.7a, where the Adams model turn has a lower radius at that low angular velocities. Then, the measured angular acceleration decreases during all the angular acceleration phase, probably because the Adams vertical friction torque increases becoming closer to the one present in the mathematical model. From this simulation, the fact that the Adams vertical friction coefficient increases with the velocity is discovered. In the next paragraph, the simplest proportional relation is exploited, that is the linear one. As in the previous test, the measured angular velocity ω_{mis} decreases during the constant velocities phase and settles to a value almost equal to 0.31 rad/s. The vertical friction torques at the wheels-ground contact points are shown in Figure 5.8a.

Test 5b The second relation exploited between ω and μ_v is the linear one. The slope c of the dependency $\mu_v = c \cdot \omega$ has been tuned with trial and error procedure finding $c = 0.009\ m$. The parameter c can be modelled as the product $c = \mu \cdot R_{\mathrm{contact}}$, where $R_{\mathrm{contact}} = 0.02\ m$ is the radius of each wheel contact surface that is supposed to be circular, while $\mu = 0.45$ is the constant friction coefficient that must be tuned. As can be seen in Figure 5.9d, the measured ω_{mis} coincides with the ideal

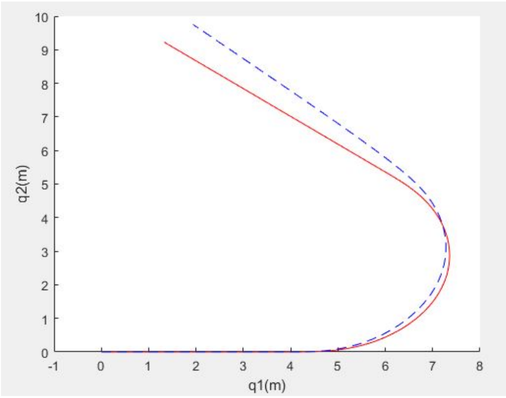

(a) *Test 5a: the red line is the nominal trajectory while the blue one the real trajectory that the Adams model makes.*

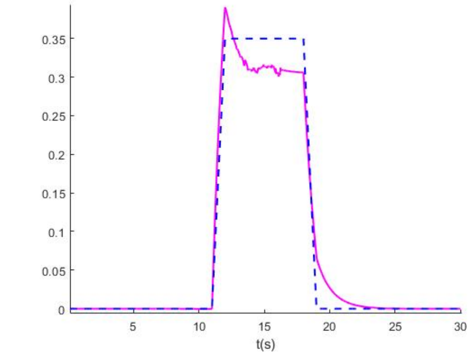

(b) *Test 5a: angular velocity ω expressed in m/s. The blue line is the nominal angular velocity ω_{nom} while the magenta line is the measured one ω_{mis}.*

Figure 5.7: Test 5a

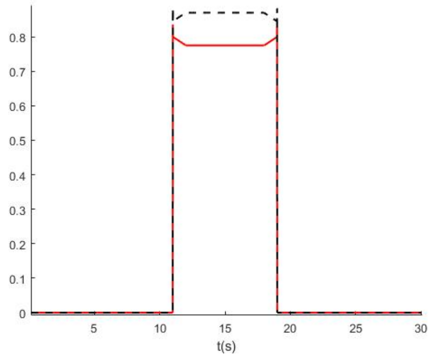

(a) *Test 5a: vertical friction torques at the wheels-ground contact points computed by the mathematical model and expressed in $N * m$. The black line refers to the right wheel vertical friction torque τ_{c2z} while the red one to the left wheel vertical friction torque τ_{c1z}.*

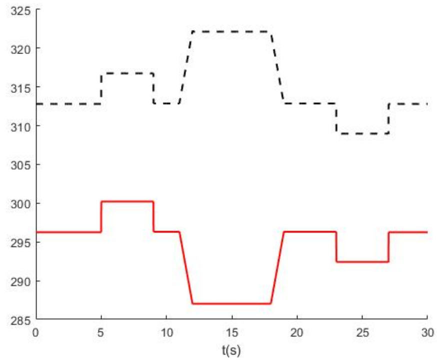

(b) *Test 5a: normal forces at the driving wheels computed by the mathematical model and expressed in N. The black line refers to the right wheel normal force f_{c2z}, while the red one to the left wheel normal force f_{c1z}.*

Figure 5.8: Test 5a

one in the angular acceleration phase. The desired velocity $\omega_{\max}$ is reached and kept almost constant during the constant velocities phase. In Figure 5.9c, the longitudinal velocity v stays more or less constant in the constant velocities phase at a value just a little lower than the desired one $v_{\max}$. In Figure 5.9a, the nominal and real trajectories are close to each other. The vertical friction torques are shown in Figure 5.10c.

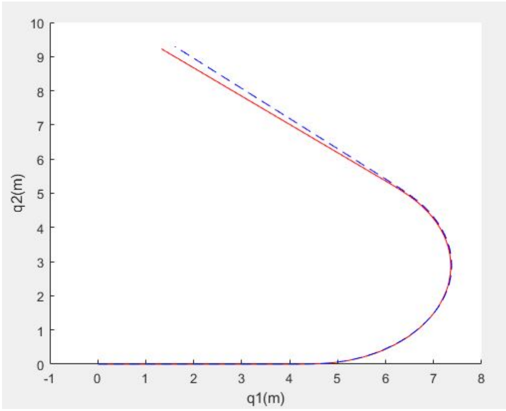

(a) *Test 5b: the red line is the nominal trajectory while the blue one the real trajectory that the Adams model makes.*

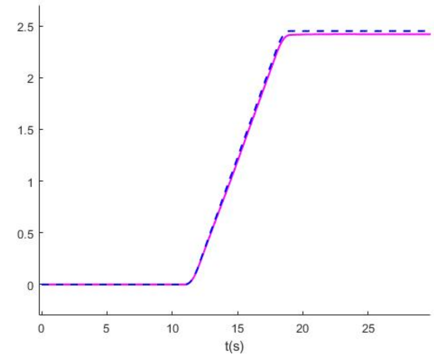

(b) *Test 5b: posture orientation q_3 expressed in rad. The blue line is the nominal orientation $q_{3\mathrm{nom}}$ while the magenta line is the measured one on the Adams model $q_{3\mathrm{mis}}$.*

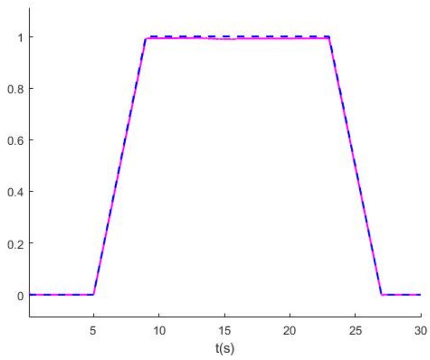

(c) *Test 5b: longitudinal velocity v expressed in m/s. The blue line is the nominal longitudinal velocity v_{nom} while the magenta line is the measured one v_{mis}.*

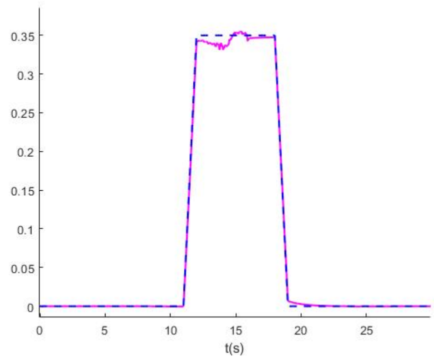

(d) *Test 5b: angular velocity ω expressed in m/s. The blue line is the nominal angular velocity ω_{nom} while the magenta line is the measured one ω_{mis}.*

Figure 5.9: Test 5b

Now that the friction model seems to behave similarly to the Adams one, its generality must be tested. Therefore new velocities profile are used in the simulations. The profile are always characterized by the subsequent nine phases described above, but the maximum velocities $v_{\max}$ and $w_{\max}$ and the accelerations $\dot{v}_{\max}$ and $\dot{w}_{\max}$ are changed.

Conclusions about test 5a and 5b From the two tests 5a and 5b, it becomes clear that the vertical torque friction coefficient at the wheels contact points has a linear dependency on the angular velocity ω because the stiction transition

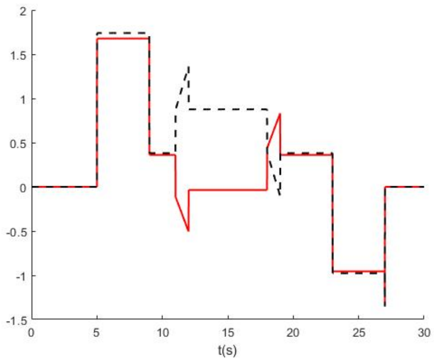

(a) *Test 5b: driving torques at the wheel side computed by the mathematical model and expressed in $N * m$. The black line refers to the right wheel torque τ_2, while the red one to the left wheel torque τ_1.*

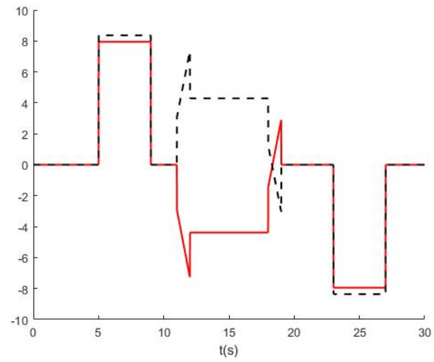

(b) *Test 5b: traction forces computed by the mathematical model and expressed in N. The black line refers to the right wheel traction force f_{c2x}, while the red one to the left wheel traction force f_{c1x}.*

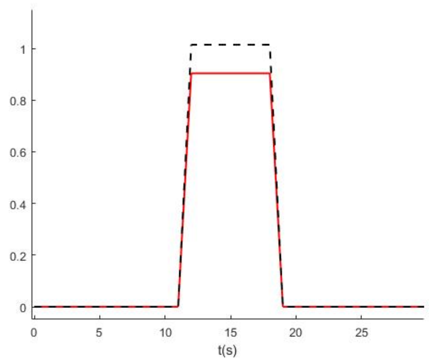

(c) *Test 5b: vertical friction torques at the wheels-ground contact points computed by the mathematical model and expressed in $N * m$. The black line refers to the right wheel vertical friction torque τ_{c2z} while the red one to the left wheel vertical friction torque τ_{c1z}.*

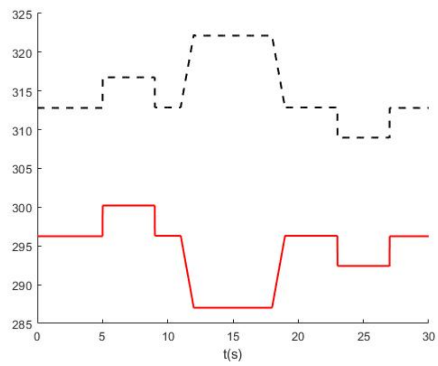

(d) *Test 5a: normal forces at the driving wheels computed by the mathematical model and expressed in N. The black line refers to the right wheel normal force f_{c2z}, while the red one to the left wheel normal force f_{c1z}.*

Figure 5.10: Test 5b

velocity set in Adams in the Coulomb friction approximation is too high. Therefore, the transition to the dynamic friction coefficient never occurs. Maybe, it has to be reduced but when the prototype robot will be ready, the friction parameters will be chosen thanks to measures on the real components.

Test 6a In test 6a (Figure 5.11a), the maximum angular velocity $\omega_{\max}$ is changed from 0.35 rad/s to 0.05 rad/s, while the other three parameters $v_{\max}$, $\dot{v}$ and $\dot{\omega}$ are equal to test 4.

Test 6b In test 6b (Figure 5.11b), the maximum longitudinal velocity $v_{\max}$ is changed from 1.0 m/s to 0.5 rad/s, while the other three parameters $\omega_{\max}$, $\dot{v}$ and $\dot{\omega}$ are equal to test 4.

Test 6c In test 6c (Figure 5.11c), the longitudinal acceleration $\dot{v}$ is greatly increased from 0.25 m/s^2 to 2 m/s^2, while the other three parameters are fixed equal to test 4.

Test 6d In test 6d (Figure 5.11d), the angular acceleration $\dot{\omega}$ is greatly increased from 0.35 rad/s^2 to 1.4 rad/s^2, while the other three parameters are fixed equal to the ones in test 4.

Test 7 One particular test is added to check the robot dynamic during a turn on itself. Indeed, in test 7, a trajectory that has the ICR in the robot logic centre is used so that the robot rotates on itself without translating.Therefore, the longitudinal velocity v is always equal to zero while the angular velocity has a trapezoidal shape described by a maximum velocity $\omega_{\max} = 0.35$ rad/s and a angular acceleration/deceleration $\dot{\omega} = 0.35$ rad/s^2. The robot orientation q_3 is shown in Figure 5.12.

Conclusions about tests 6a, 6b, 6c, 6d and 7 In all these tests, the results are acceptable, therefore the vertical friction torque modelling in the mathematical model, matches the one in Adams.

Up to now, the friction interaction forces between the castors and the ground were set to zero in the Adams model. This was done to check the behaviour of the mathematical model that does not have the castors equations. Castors are considered only to provide the mathematical model the third contact point in addition to the two driving wheels ones. But the longitudinal and lateral forces exerted by the ground on the wheel are not considered. They will be introduce in the Adams model exploited to test the motors control algorithm.

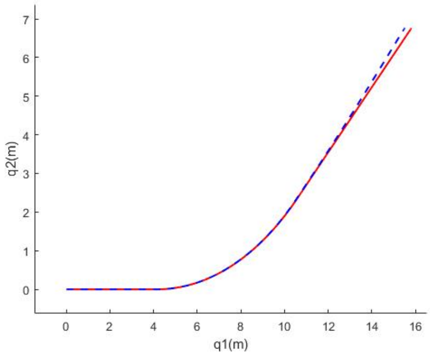

(a) *Test 6a: the red line is the nominal trajectory while the blue one the real trajectory that the Adams model makes.*

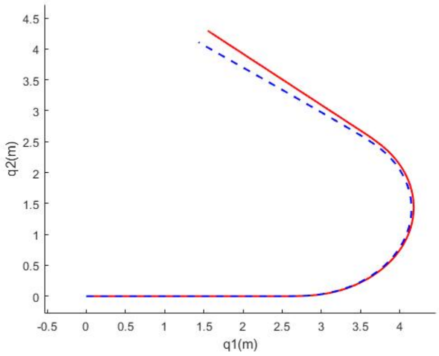

(b) *Test 6b: the red line is the nominal trajectory while the blue one the real trajectory that the Adams model makes.*

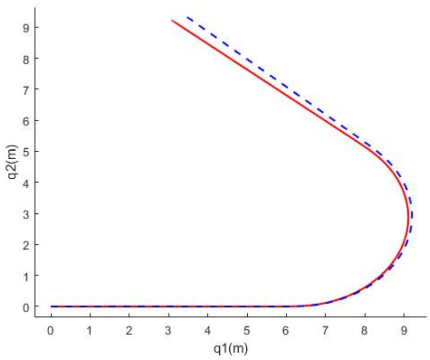

(c) *Test 6c: the red line is the nominal trajectory while the blue one the real trajectory that the Adams model makes.*

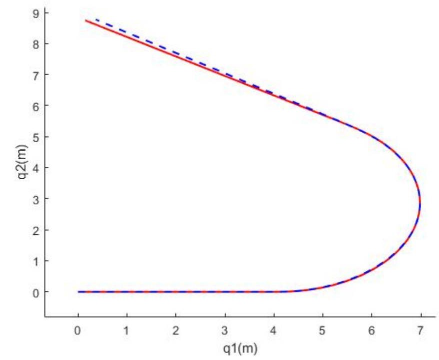

(d) *Test 6d: the red line is the nominal trajectory while the blue one the real trajectory that the Adams model makes.*

Figure 5.11: Tests 6

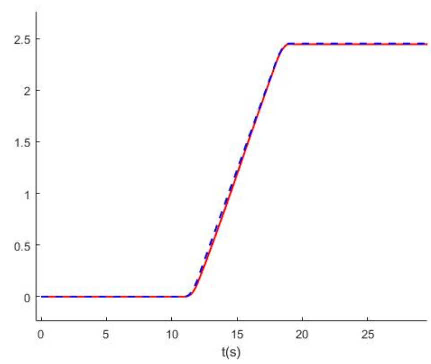

Figure 5.12: Test 7: posture orientation q_3 expressed in rad. The blue line is the nominal orientation $q_{3\text{nom}}$ while the magenta line is the measured one on the Adams model $q_{3\text{mis}}$.

Chapter 6

Comparison with prototype measures

In the previous Chapter, the refinement of the mathematical model with respect to the Adams model was performed. In this Chapter, a step forward is done since the robot prototype is ready. The robot is moved on a fixed path shown in Figure 6.1 at different velocities. To have a complete view of the robot dynamics, the chosen path is made of straight lines and turns.

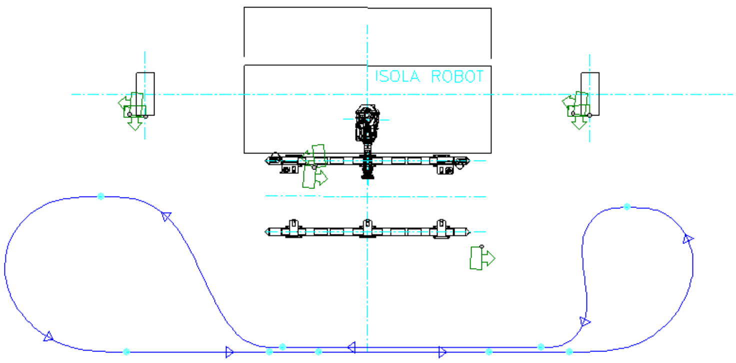

Figure 6.1: Path followed by the robot

While the robot moves along this path, the motors shafts angular velocities ($\dot{\theta}_{\mathrm{m1}}^{\mathrm{mis}}, \dot{\theta}_{\mathrm{m2}}^{\mathrm{mis}}$) and the motors armature currents ($I_{\mathrm{m1}}, I_{\mathrm{m2}}$) are measured. From these currents, the motors torques ($\tau_{\mathrm{m1}}^{\mathrm{mis}}, \tau_{\mathrm{m2}}^{\mathrm{mis}}$) are computed with the formulas of the brushless DC motor (6.1), where K_m is the torque constant that the data sheet provides equal to $K_m = 0.1156\ (N \cdot m)/A$.

$$\begin{cases} \tau_{\mathrm{m1}}^{\mathrm{mis}} = K_m \cdot I_{\mathrm{m1}} \\ \tau_{\mathrm{m2}}^{\mathrm{mis}} = K_m \cdot I_{\mathrm{m2}} \end{cases} \tag{6.1}$$

In order to check if the mathematical model matches the real robot dynamics, the inverse dynamic problem is solved. As inputs, it receives the trajectories expressed with respect to the wheels angular velocities ($\dot{\theta}_1, \dot{\theta}_2$) and with respect to the robot longitudinal v and angular ω velocities. As outputs, it returns the driving torques ($\tau_1^{\text{comp}}, \tau_2^{\text{comp}}$) at the reducers output shafts.

As it can be understood, the measures are related to the motor side while the equations variables belongs to the wheel side. In order to make them comparable, the formulas and equations that relate the wheel side variables to the motor side variables are exploited.

The total friction torques both in gear and rotor ($\tau_{\text{am}}, \tau_{\text{ag}}$) are expressed at the motor side due to the way measures have been taken. The measures set up and the data processing will be detailed in the following section.

Therefore, the torques returned by the mathematical model ($\tau_1^{\text{comp}}, \tau_2^{\text{comp}}$) are moved from the gearbox output shaft to the input shaft just dividing them by the gearbox ratio n. In this way they can be compared with the measured torques ($\tau_{\text{m1}}^{\text{mis}}, \tau_{\text{m2}}^{\text{mis}}$).

$$\begin{cases} \tau_{\text{m1}}^{\text{comp}} = \frac{\tau_1^{\text{comp}}}{n} \\ \tau_{\text{m2}}^{\text{comp}} = \frac{\tau_2^{\text{comp}}}{n} \end{cases} \tag{6.2}$$

Since the robot equations depend on the robot longitudinal (v) and angular (ω) velocities and on the wheels angular speeds ($\dot{\theta}_1, \dot{\theta}_2$), the following formulas are needed to compute them from the measured angular speeds ($\dot{\theta}_{\text{m1}}^{\text{mis}}, \dot{\theta}_{\text{m2}}^{\text{mis}}$) of the motors shafts.

$$\begin{cases} \dot{\theta}_1 = \frac{\dot{\theta}_{\text{m1}}^{\text{mis}}}{n} \\ \dot{\theta}_2 = \frac{\dot{\theta}_{\text{m2}}^{\text{mis}}}{n} \\ v = \frac{R \cdot (\dot{\theta}_1 + \dot{\theta}_2)}{2} = \frac{R \cdot (\dot{\theta}_{\text{m1}}^{\text{mis}} + \dot{\theta}_{\text{m2}}^{\text{mis}})}{2 \cdot n} \\ \omega = \frac{R \cdot (\dot{\theta}_2 - \dot{\theta}_1)}{2 \cdot b_1} = \frac{R \cdot (\dot{\theta}_{\text{m2}}^{\text{mis}} - \dot{\theta}_{\text{m1}}^{\text{mis}})}{2 \cdot n \cdot b_1} \end{cases} \tag{6.3}$$

6.1 Motors and reducers friction modelling

In the first part of the thesis, the total friction torque of the transmission line was modelled with the Coulomb approximation both in the Adams model and in the mathematical equations. To refine the friction model, measures have been taken on the prototype robot. For these measures, the robot was lifted so that the driving wheels were not in contact with the ground. In this way, when the motor shaft is rotating at constant angular speed, the motor torque τ_m coincides with the total friction torque at the motor side given by the sum of the motor friction torque τ_{am} with the gearbox one τ_{ag}. Indeed, when the angular acceleration is zero, the inertia torques are silent and since the wheels are lifted also the torque due to the traction force f_{cx} is null.

Therefore, the motors shafts angular velocities are brought to a desired value $\dot{\theta}_{\mathrm{m}}^{\mathrm{max}}$ and kept constant at that value for a significant period of time, while measuring the motors currents. From the motors currents, the motors torques are computed $\tau_m = \tau_a^{\mathrm{tot}} = \tau_{\mathrm{am}} + \tau_{\mathrm{ag}}$. The same test was performed with four different values of $\dot{\theta}_{\mathrm{m}}^{\mathrm{max}}$, since the goal was to find the dependency of the total friction torque τ_a^{tot} on the motor angular speed $\dot{\theta}_m$. The motor angular speeds and the corresponding currents and friction torques are listed in Table 6.1 for the left motor and Table 6.2 for the right one. The graphs shown in Figures 6.3a and 6.3b were created with $\dot{\theta}_m$ on the x axis and τ_a^{tot} on the y axis. Both show an almost linear dependency at the velocities of interest. The friction torque τ_a^{tot} is expected to settle at a constant value from a certain velocity on, but this behaviour can be neglected at the velocities the measures were performed. Therefore, the linear regression method was used to find the line that better approximates the four points of each graph. The regression lines of the left friction torque $\tau_{\mathrm{a1}}^{\mathrm{tot}}$ and of the right friction torque $\tau_{\mathrm{a2}}^{\mathrm{tot}}$ are listed below. The friction torques $(\tau_{\mathrm{a1}}^{\mathrm{tot}}, \tau_{\mathrm{a2}}^{\mathrm{tot}})$ are expressed in $N \cdot m$ and the motor angular velocities $(\dot{\phi}_{\mathrm{m1}}, \dot{\phi}_{\mathrm{m2}})$ in rad/s. It is important to underline that the model validity range spans from $-166.4\ rad/s$ to $166.4\ rad/s$.

$$\begin{cases} \tau_{\mathrm{a1}}^{\mathrm{tot}} = 0.0043 \cdot \dot{\phi}_{\mathrm{m1}} + 0.2065 \\ \tau_{\mathrm{a2}}^{\mathrm{tot}} = 0.0041 \cdot \dot{\phi}_{\mathrm{m2}} + 0.2082 \end{cases} \tag{6.4}$$

Since the two lines are very similar, an average line is going to be used for both the friction torques.

$$\tau_{\mathrm{a}}^{\mathrm{tot}} = 0.0042 \cdot \dot{\phi}_{\mathrm{m}} + 0.207 \tag{6.5}$$

Therefore, the friction model looks very similar to the one that combines the Coulomb friction with the viscous friction shown in Figure 6.2a. The step transition at null angular velocity will be substituted with a line having a high angular coefficient not to have a discontinuous model as the one in Figure 6.2b. The transition velocity $\dot{\theta}_t$ at which the friction torque is equal to the stiction torque $\tau_{\mathrm{stic}} = 0.207$ Nm is fixed equal to $\dot{\theta}_t = 0.01\ rad/s = 0.57\ deg/s$. Then the high angular coefficient m_{stic} is computed as the ratio of $m_{\mathrm{stic}} = \tau_{\mathrm{stic}}/\dot{\theta}_t = 20.7\ Nm/(rad/s)$.

$$\tau_a^{\mathrm{tot}} = \begin{cases} m_{\mathrm{as}} \cdot \dot{\phi}_{\mathrm{m}} & \text{if } -\dot{\phi}_t < \dot{\phi}_{\mathrm{m}} < \dot{\phi}_t \\ 0.0042 \cdot (\dot{\phi}_{\mathrm{m}} - \dot{\phi}_t) + 0.207 & \text{if } \dot{\phi}_{\mathrm{m}} > \dot{\phi}_t \\ 0.0042 \cdot (\dot{\phi}_{\mathrm{m}} + \dot{\phi}_t) - 0.207 & \text{if } \dot{\phi}_{\mathrm{m}} < -\dot{\phi}_t \end{cases} \tag{6.6}$$

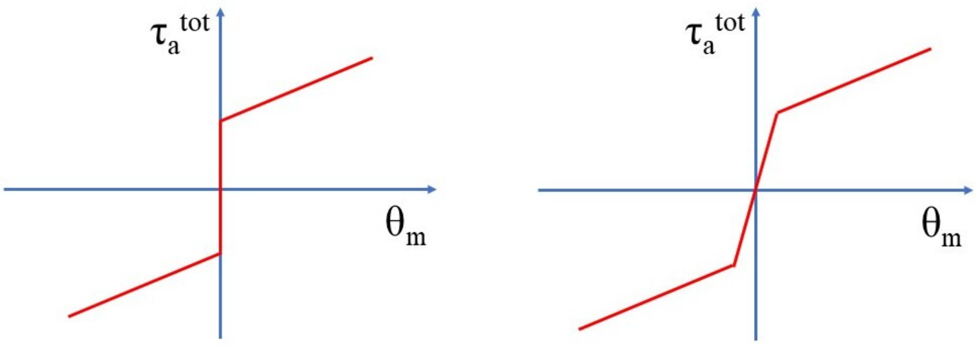

(a) *Discontinuous friction modelling* (b) *Continuous friction modelling*

Figure 6.2: Friction modelling

Table 6.1: Left friction torque $\tau_{\mathrm{a1}}^{\mathrm{tot}}$ at the motor side

$\dot{\theta}_{\mathrm{m1}}(rad/s)$	$I_{\mathrm{m1}}(A)$	$\tau_{\mathrm{a1}}^{\mathrm{tot}}(N \cdot m)$
160.3	7.65	0.884
99.6	5.68	0.657
33.2	3.12	0.361
16.8	2.25	0.260

6.2 Mass and inertia computations

Mass and inertia values computed in Chapter 3 are not equal to the one of the prototype. The previous computation have been performed using the Agilino CAD files referring to the last mechanical design that is slightly different from the prototype one.

The main difference regards the bearing structure that in the prototype robot is bigger and is made of MDF (Medium Density Fibreboard) instead of aluminium. The MDF volume density is equal to $\rho_{\mathrm{MDF}} = 680\ Kg/m^3$ while the aluminium one is $\rho_{\mathrm{AL}} = 2.7\ g/cm^3$, therefore the MDF bearing structure will be lighter. Another important difference is that the battery is not the right one though it cannot be inserted inside the bearing structure as the mechanical design envisages. For this reason, it is placed on top of the bearing structure, thus moving up the mass centre of the whole robot. Less relevant differences are the charging plates absence on the prototype and the presence of the motor drives that have negligible masses with respect to the whole one M_m. Another important difference regards the motors and gearboxes displacements. Indeed, the ones related to the left wheel and the ones related to the right wheel are symmetrical with respect to the vertical axis passing through the robot logic centre. The battery, motors and gearboxes new positions

Table 6.2: Right friction torque $\tau_{\mathrm{a2}}^{\mathrm{tot}}$ at the motor side

$\dot{\theta}_{\mathrm{m2}}(rad/s)$	$I_{\mathrm{m2}}(A)$	$\tau_{\mathrm{a2}}^{\mathrm{tot}}(N \cdot m)$
166.4	7.48	0.866
99.8	5.81	0.672
33.3	3.08	0.357
17.0	2.13	0.246

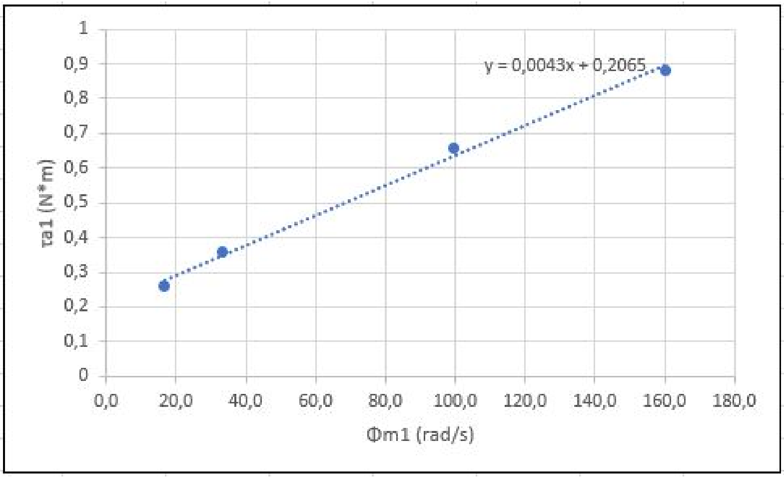

(a) *Left friction torque* $\tau_{\mathrm{a1}}^{\mathrm{tot}}(N \cdot m)$ *VS left motor angular speed* $\dot{\theta}_{\mathrm{m1}}(rad/s)$

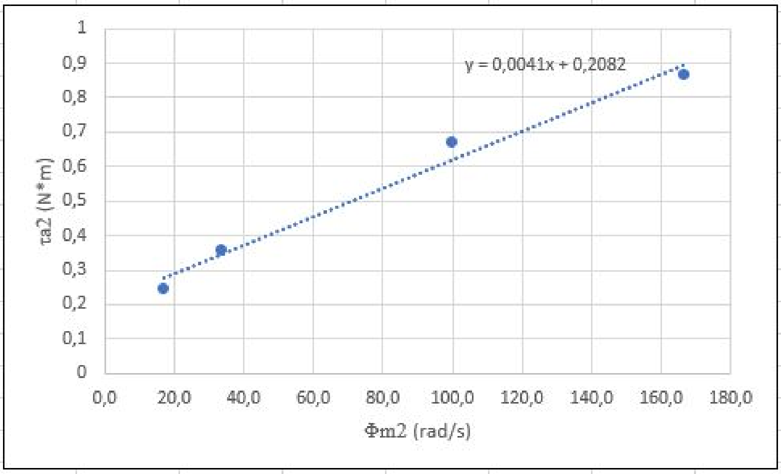

(b) *Right friction torque* $\tau_{\mathrm{a2}}^{\mathrm{tot}}(N \cdot m)$ *VS right motor angular speed* $\dot{\theta}_{\mathrm{m2}}(rad/s)$

Figure 6.3: Friction torques dependency on the motor angular velocities

allow to have the upper volume mass centre closer to the vertical line passing through the robot logic centre Indeed, its position with respect to the robot base mass centre moves to $[x_m, y_m, z_m] = [-4.3, 5.1, 332.8]mm$.

First, thanks to Adams, the mass m_{BS} and the vertical inertia moment I_{zBS} of the prototype bearing structure are found and listed below.

$$\begin{cases} m_{\mathrm{BS}} = 7.52Kg \\ I_{\mathrm{zBS}} = 4894.5Kg \cdot cm^2 \end{cases} \tag{6.7}$$

Then, the vertical inertia moment of the battery I_{zB} is computed easily from (6.8) since it has a parallelepiped shape with dimensions (LxHxP) = (540x260x250)mm and mass equal to $M_{\mathbf{B}} = 27\ Kg$.

$$I_{\mathrm{zB}} = M_B \cdot \frac{L^2 + P^2}{12} = 0.8Kg \cdot m^2 \tag{6.8}$$

The final parameters that describe the robot upper volume are listed in Table 6.3.

Table 6.3: Mechanical parameters of the prototype upper volume

Quantity	Symbol	Unit measure	Value
upper volume mass	M_m	Kg	62.22
upper volume vertical inertia moment	I_{zm}	$Kg \cdot m^2$	2.4
upper volume COM	r_{m}	mm	[-4.3, 5.1, 332.8]

6.3 Simulations

In this section, the simulation plots with some comments will be reported. The robot is moved along the path shown in Figure 6.1. The trajectory is characterized by a longitudinal velocity equal to $v = 0.3\ m/s$ on the two straights and the robot longitudinal and angular velocities are plotted in Figures 6.4a. The comparisons between the torques computed from the measured armature currents and the torques resulting from the inverse dynamic solution of the mathematical model are performed. The torques comparisons allow the friction model refinement (6.9) and are shown in Figures 6.5a and 6.5b.

$$\begin{cases} \tau_{\mathrm{a1}}^{\mathrm{tot}} = 0.0029 \cdot \dot{\phi}_{\mathrm{m1}} + 0.207 \\ \tau_{\mathrm{a2}}^{\mathrm{tot}} = 0.0032 \cdot \dot{\phi}_{\mathrm{m2}} + 0.207 \end{cases} \tag{6.9}$$

It's clear that for each simulation, the measured and computed torques evolve

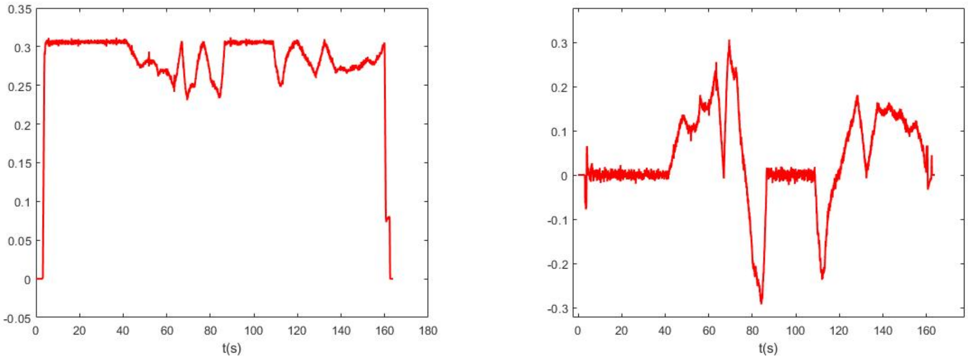

(a) *Robot longitudinal velocity v expressed in m/s.*

(b) *Robot angular velocity ω expressed in rad/s.*

Figure 6.4: Robot velocities profiles

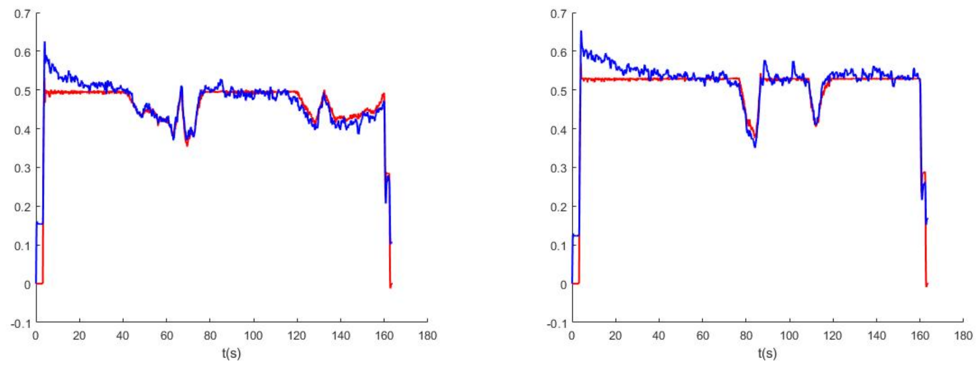

(a) *Left wheel torque in $N \cdot m$. The blue line refers to the measured torque, while the red line refers to the mathematical model torque.*

(b) *Right wheel torque in $N \cdot m$. The blue line refers to the measured torque, while the red line refers to the mathematical model torque.*

Figure 6.5: Torques comparison

similarly during the whole lap except for the first longitudinal acceleration. Indeed, during the first longitudinal acceleration the measured torques are a little bit greater than the ones expected by the mathematical model. Such a difference could be due to some non linearities in the transmission line not included in the model.

An important aspect that can be extracted from these simulations is the estimate of transmission line efficiency. It can be described as the percentage of the total motor torque that results into the traction force at the wheel-ground contact point. Indeed, the total motor torque can be divided into three components. The first one is wasted in the transmission line friction torques and is always present when the robot is moving. The second one provides the inertial torque needed to change the angular velocity of the total inertia moment of the transmission line.

The third one is the torque that results into the traction force at the wheel-ground contact point. The last two components are present only when the robot changes its motion state, therefore when the motor angular speed $\dot{\theta}_m$ has non null rate of change $\ddot{\theta}_m$. A simple estimate of this efficiency can be extracted comparing the motors torques with the friction torques shown in Figures 6.6a and 6.6b. Most of the motor torque is wasted due to friction effects.

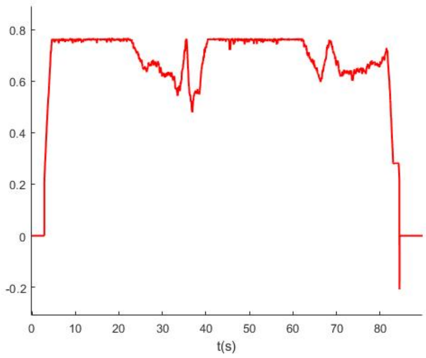

(a) *Friction torque of the left transmission line expressed in $N \cdot m$.*

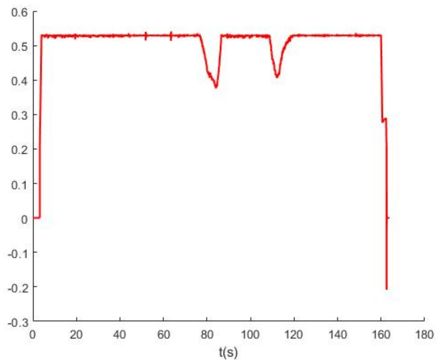

(b) *Friction torque of the right transmission line expressed in $N \cdot m$.*

Figure 6.6: Friction torques

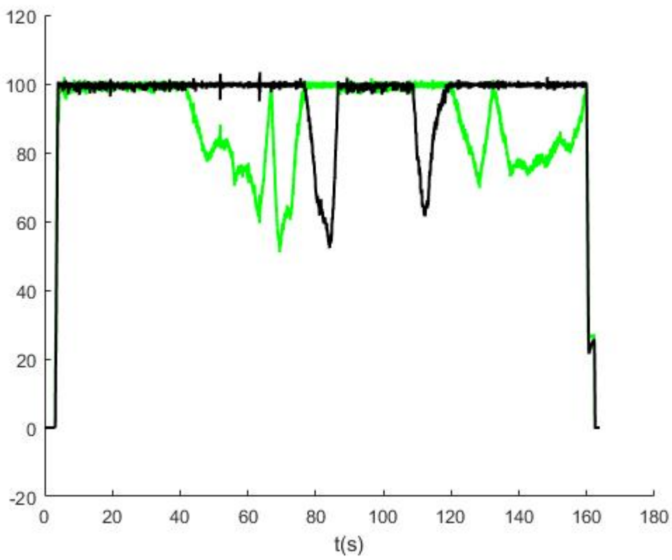

Figure 6.7: Motors shafts angular speeds expressed in rad/s. The green line refers to the left motor one while the black line to the right one.

Chapter 7

Control strategies

In this chapter, control strategies will be developed in order to drive the two brushless motors. The autonomous guided vehicles have two control layers in cascade. The high layer takes care of the robot position in space and returns as output the trajectory the robot has to follow. The trajectory is described through the motors angular velocities that act as the references of the low control layer. Though, the low control layer pilots the driving motors so that their speeds follow the references.

The higher layer control strategy takes into account the robot position in space, the position of the target the robot has to reach and the positions of the obstacles that laser scanners continuously detect. This whole information allows the high control layer to plan and continuously update the trajectories the robot has to follow to reach the target.

The low layer controller compares the reference speeds with the ones measured by the encoders at the motors shafts and returns the proper motors armature voltages. In this Chapter, this second control layer is developed.

From the control point of view, the AGV can be compared with the industrial manipulators since the high layer performs something similar to a task space control while the low one to a joint space control. Therefore, in this Chapter a joint space control will be developed. The possible joint space control architectures are two [13]:

- Decentralized control or independent joint control: Each joint motor has a local controller that takes into account only local variables. Therefore, the controller design is relative simple, since it is a SISO type but it considers only an approximated model of the joint. It is based on the equivalent model of an electrical motor and between the motor and the joint requires the presence of a gearbox. The gearbox presence reduces the effects of non linearities and coupling effects making the strategy of local controllers more effective.
- Centralized control: Only one MIMO controller is present. It receives all the joints variables and elaborates the control signals for all the motors. Its design is based on the robot complete model and it is used when no gearboxes are

present or when the disturbance torques are significant in the robot dynamics. The centralized control tries to cancel these disturbance torques with non linear compensation terms. The main architecture is the inverse dynamics one.

7.1 Robot model for control purposes

The first step, before choosing which is the best control strategy, is to find a simple robot model. In this model, the vertical dynamics is no more considered. Indeed, velocities and acceleration limits that keep the robot on safe trajectories have already been found offline thanks to the previous analysis. Then, instead of considering the robot base, the two driving wheels and the upper volume as different parts, in this model the robot is approximated with just one block characterized by a mass $M = 57.9\ Kg$ and a vertical moment of inertia $J = 3.78\ Kg \cdot m^2$. This simplification is suggested in [11]. The general mass centre position with respect to the logic centre reference frame R_a is located at $r_m = (x_m, y_m)$. Finally, the friction forces at the bearings are not considered. Due to the previous assumptions, the model includes only three equations written in (7.1): the two forces balances on the plane and the torques balance on the direction perpendicular to the plane. The first equation is the balance on the robot longitudinal direction, while the second one on the robot transversal direction.

$$\begin{cases} M \cdot (\dot{v} - x_m \cdot \omega^2 - y_m \cdot \dot{\omega}) = F_{\mathrm{c1x}} + F_{\mathrm{c2x}} \\ M \cdot (\omega \cdot v - y_m \cdot \omega^2 + x_m \cdot \dot{\omega}) = F_{\mathrm{c1y}} + F_{\mathrm{c2y}} \\ J \cdot \dot{\omega} = -x_m \cdot (F_{\mathrm{c1y}} + F_{\mathrm{c2y}}) - b_1 \cdot (F_{\mathrm{c1x}} - F_{\mathrm{c2x}}) + y_m \cdot (F_{\mathrm{c1x}} + F_{\mathrm{c2x}}) \end{cases} \tag{7.1}$$

Now, substituting in the third equation $F_{\mathrm{c1x}} + F_{\mathrm{c2x}}$ from the first equation and $F_{\mathrm{c1y}} + F_{\mathrm{c2y}}$ from the second equation, the following equation (7.2) is obtained.

$$(J + M \cdot (x_m^2 + y_m^2)) \cdot \dot{\omega} + x_m \cdot (M\omega v) - y_m \cdot (M\dot{v}) = b_1 \cdot (F_{\mathrm{c2x}} - F_{\mathrm{c1x}}) \tag{7.2}$$

Combining (7.2) with the first one of (7.1), the system without the transversal contact forces F_{c1y} and F_{c2y} is obtained.

$$\begin{cases} M \cdot (\dot{v} - x_m \cdot \omega^2 - y_m \cdot \dot{\omega}) = F_{\mathrm{c1x}} + F_{\mathrm{c2x}} \\ (J + M \cdot (x_m^2 + y_m^2)) \cdot \dot{\omega} + x_m \cdot (M\omega v) - y_m \cdot (M\dot{v}) = \\ = b_1 \cdot (F_{\mathrm{c2x}} - F_{\mathrm{c1x}}) \end{cases} \tag{7.3}$$

Since friction torques at the bearings are not considered and the wheel inertia around its main axis is neglected, the following equations (7.4) link the torques applied to the wheels (τ_L, τ_R) with the traction forces $(F_{\mathrm{c1x}}, F_{\mathrm{c2x}})$, where $R = 0.1$ m is the wheels radius.

$$\begin{cases} F_{\mathrm{c1x}} = \frac{\tau_L}{R} \\ F_{\mathrm{c2x}} = \frac{\tau_R}{R} \end{cases} \tag{7.4}$$

Substituting (7.4) into (7.3), the following equations are obtained:

$$\begin{cases} M \cdot (\dot{v} - x_m \cdot \omega^2 - y_m \cdot \dot{\omega}) = \frac{\tau_L + \tau_R}{R} \\ (J + M \cdot (x_m^2 + y_m^2)) \cdot \dot{\omega} + x_m \cdot (M\omega v) - y_m \cdot (M\dot{v}) = \\ = \frac{b_1 \cdot (\tau_R - \tau_L)}{R} \end{cases} \tag{7.5}$$

Now, the system (7.5) is translated from the longitudinal velocity v and angular speed ω variables to the wheels angular velocities $\dot{\phi}_L$ and $\dot{\phi}_R$, exploiting the formulas of the differential drive robot kinematic model.

$$\begin{cases} \{\frac{M \cdot R}{2} - \frac{M \cdot R \cdot y_m}{2 \cdot b_1}\} \cdot \ddot{\phi}_R + \{\frac{M \cdot R}{2} + \frac{M \cdot R \cdot y_m}{2 \cdot b_1}\} \cdot \ddot{\phi}_L - \{\frac{M \cdot R^2 \cdot x_m}{4 \cdot b_1^2}\} \cdot \dot{\phi}_R^2 + \\ -\{\frac{M \cdot R^2 \cdot x_m}{4 \cdot b_1^2}\} \cdot \dot{\phi}_L^2 + \{\frac{M \cdot R^2 \cdot x_m}{2 \cdot b_1^2}\} \cdot \dot{\phi}_L \cdot \dot{\phi}_R = \frac{\tau_L + \tau_R}{R} \\ \{\frac{R \cdot [J + M \cdot (x_m^2 + y_m^2)]}{2 \cdot b_1^2}\} \cdot \ddot{\phi}_R - \{\frac{R \cdot [J + M \cdot (x_m^2 + y_m^2)]}{2 \cdot b_1^2}\} \cdot \ddot{\phi}_L + \{\frac{M \cdot R^2 \cdot x_m}{4 \cdot b_1^2}\} \cdot \dot{\phi}_R^2 \\ -\{\frac{M \cdot R^2 \cdot x_m}{4 \cdot b_1^2}\} \cdot \dot{\phi}_L^2 - \{\frac{M \cdot R \cdot y_m}{2 \cdot b_1}\} \cdot (\dot{\phi}_R + \dot{\phi}_L) = \frac{\tau_R - \tau_L}{R} \end{cases} \tag{7.6}$$

Finally summing and subtracting the two equations of (7.6), it is possible to get the following equations referring respectively to the left and right joints.

$$\begin{cases} \{\frac{M \cdot R^2}{4} + \frac{M \cdot R^2 \cdot y_m}{4 \cdot b_1} + \frac{R^2 \cdot [J + M \cdot (x_m^2 + y_m^2)]}{4 \cdot b_1^2}\} \cdot \ddot{\phi}_L + \\ +\{\frac{M \cdot R^2}{4} - \frac{M \cdot R^2 \cdot y_m}{4 \cdot b_1} - \frac{R^2 \cdot [J + M \cdot (x_m^2 + y_m^2)]}{4 \cdot b_1^2}\} \cdot \ddot{\phi}_R - \{\frac{M \cdot R^3 \cdot x_m}{4 \cdot b_1^2}\} \cdot \dot{\phi}_R^2 + \\ +\{\frac{M \cdot R^3 \cdot x_m}{4 \cdot b_1^2}\} \cdot \dot{\phi}_L \cdot \dot{\phi}_R + \{\frac{M \cdot R^2 \cdot y_m}{4 \cdot b_1}\} \cdot (\dot{\phi}_R + \dot{\phi}_L) = \tau_L \\ \{\frac{M \cdot R^2}{4} - \frac{M \cdot R^2 \cdot y_m}{4 \cdot b_1} + \frac{R^2 \cdot [J + M \cdot (x_m^2 + y_m^2)]}{4 \cdot b_1^2}\} \cdot \ddot{\phi}_R + \\ +\{\frac{M \cdot R^2}{4} + \frac{M \cdot R^2 \cdot y_m}{4 \cdot b_1} - \frac{R^2 \cdot [J + M \cdot (x_m^2 + y_m^2)]}{4 \cdot b_1^2}\} \cdot \ddot{\phi}_L - \{\frac{M \cdot R^3 \cdot x_m}{4 \cdot b_1^2}\} \cdot \dot{\phi}_L^2 + \\ +\{\frac{M \cdot R^3 \cdot x_m}{4 \cdot b_1^2}\} \cdot \dot{\phi}_L \cdot \dot{\phi}_R - \{\frac{M \cdot R^2 \cdot y_m}{4 \cdot b_1}\} \cdot (\dot{\phi}_R + \dot{\phi}_L) = \tau_R \end{cases} \tag{7.7}$$

Writing (7.7) in matrix form as in (7.8) makes the equations more readable. The diagonal matrix J_b contains the joints main moments of inertia, while the vector τ_d includes all the non linear τ_n and coupling τ_c effects, where non linear effects refer to Coriolis and centrifugal torques. As it can be seen, the non linear effects τ_n are present only when the robot mass centre is not on the vertical axis passing through the robot logic centre, though when x_m and y_m are not zero. This result is meaningful and it was anticipated in the state of the art. Indeed, if the robot mass centre is on the logic centre, the centrifugal force during a turn has null arm, therefore it causes a null moment. In this way, the controller does not have to balance the centrifugal force moment to keep the robot in the turn.

$$\begin{bmatrix} J_{\mathrm{bL}} & 0 \\ 0 & J_{\mathrm{bR}} \end{bmatrix} \cdot \begin{bmatrix} \ddot{\phi}_L \\ \ddot{\phi}_R \end{bmatrix} + \begin{bmatrix} 0 & J_{\mathrm{cLR}} \\ J_{\mathrm{cRL}} & 0 \end{bmatrix} \cdot \begin{bmatrix} \ddot{\phi}_L \\ \ddot{\phi}_R \end{bmatrix} + \begin{bmatrix} \tau_{\mathrm{nL}} \\ \tau_{\mathrm{nR}} \end{bmatrix} = \begin{bmatrix} \tau_{\mathrm{L}} \\ \tau_{\mathrm{R}} \end{bmatrix} \tag{7.8}$$

$$J_{\mathrm{b}} \cdot \ddot{\phi} + J_{\mathrm{c}} \cdot \ddot{\phi} + \tau_n = \tau \tag{7.9}$$

$$J_{\mathrm{b}} \cdot \ddot{\phi} + \tau_d = \tau \tag{7.10}$$

7.2 Control strategy

Agilino mechanical design tries to place the mass centre exactly on the vertical axis passing through the logic centre, therefore x_m and y_m are close to zero. With $x_m = y_m = 0$, the disturbance torques have a small influence on the robot behaviour because the non linear effects disappear while the coupling effects are negligible. Thanks to these considerations, it is possible to choose the decentralized control as the best architecture to drive the motors when Agilino moves on its own. As explained before, the robot task is to pull libraries and tracks. In these working conditions, the mass centre of the whole system including both the robot and the library could be no more on the robot logic centre. Therefore, the non linear effects could become relevant and the decentralized control ineffective. The non linear effects enhancement could require a more effective centralized control strategy. This thesis looks for a control strategy focused on the robot moving on its own. Therefore, the decentralized control is the best one. The assumption $x_m = y_m = 0$ is close to the real mechanical design. Even though they are not precisely equal to zero, this is not a problem because one of the controller goals is to be robust enough to deal also with the mechanical approximations. The updated equations (7.12) with null x_m and y_m are listed below.

$$\begin{bmatrix} J_{\mathrm{bL}} & 0 \\ 0 & J_{\mathrm{bR}} \end{bmatrix} \cdot \begin{bmatrix} \ddot{\phi}_L \\ \ddot{\phi}_R \end{bmatrix} + \begin{bmatrix} 0 & J_{\mathrm{cLR}} \\ J_{\mathrm{cRL}} & 0 \end{bmatrix} \cdot \begin{bmatrix} \ddot{\phi}_L \\ \ddot{\phi}_R \end{bmatrix} = \begin{bmatrix} \tau_{\mathrm{L}} \\ \tau_{\mathrm{R}} \end{bmatrix} \tag{7.11}$$

$$\begin{cases} \{\frac{M\cdot R^2}{4} + \frac{R^2\cdot J}{4\cdot b_1^2}\} \cdot \ddot{\phi}_L + \{\frac{M\cdot R^2}{4} - \frac{R^2\cdot J}{4\cdot b_1^2}\} \cdot \ddot{\phi}_R = \tau_L \\ \{\frac{M\cdot R^2}{4} + \frac{R^2\cdot J}{4\cdot b_1^2}\} \cdot \ddot{\phi}_R + \{\frac{M\cdot R^2}{4} - \frac{R^2\cdot J}{4\cdot b_1^2}\} \cdot \ddot{\phi}_L = \tau_R \end{cases} \tag{7.12}$$

In this case, the main inertia moments, computed with (7.13), are equal to $J_{\mathrm{bL}} = J_{\mathrm{bR}} = 0.3\ Kg \cdot m^2$. Instead, the coupling inertia moments, computed with (7.14), are equal to $J_{\mathrm{cLR}} = J_{\mathrm{cRL}} = -6.45 \cdot 10^{-3}\ Kg \cdot m^2$. Therefore, the coupling inertia moments are negligible with respect to the main ones.

$$J_{\mathrm{bL}} = J_{\mathrm{bR}} = \frac{M \cdot R^2}{4} + \frac{R^2 \cdot J}{4 \cdot b_1^2} = \frac{R^2}{4} \cdot \left(M + \frac{J}{4 \cdot b_1^2}\right) \tag{7.13}$$

$$J_{\mathrm{cLR}} = J_{\mathrm{cRL}} = \frac{M \cdot R^2}{4} - \frac{R^2 \cdot J}{4 \cdot b_1^2} = \frac{R^2}{4} \cdot \left(M - \frac{J}{4 \cdot b_1^2}\right) \tag{7.14}$$

At this point, to bring the main inertia moments from the wheel side ($J_{\mathrm{bL}}, J_{\mathrm{bR}}$) to the motor side ($J'_{\mathrm{bL}}, J'_{\mathrm{bR}}$), they are divided by the square of the gearbox ratio $n = 25$. The computation returns $J'_{\mathrm{bL}} = J'_{\mathrm{bR}} = 4.8 \cdot 10^{-4}\ Kg \cdot m^2$.

$$\begin{cases} J'_{\mathrm{bL}} = \frac{J_{\mathrm{bL}}}{n^2} \\ J'_{\mathrm{bR}} = \frac{J_{\mathrm{bR}}}{n^2} \end{cases} \tag{7.15}$$

To find the total inertia moment at the motor side ($J_{\mathrm{tL}}, J_{\mathrm{tR}}$), both the inertia moments of the gearbox $J_{\mathrm{GB}} = 1.387 \cdot 10^{-4}\ Kg \cdot m^2$ and of the motor $J_{\mathrm{M}} = 1.89 \cdot 10^{-4}\ Kg \cdot m^2$ have to be added to the robot main inertia moments ($J'_{\mathrm{bL}}, J'_{\mathrm{bR}}$). The computation returns $J_{\mathrm{tL}} = J_{\mathrm{tR}} = 8.077 \cdot 10^{-4}\ Kg \cdot m^2$.

$$\begin{cases} J_{\mathrm{tL}} = J'_{\mathrm{bL}} + J_{\mathrm{GB}} + J_{\mathrm{M}} \\ J_{\mathrm{tR}} = J'_{\mathrm{bR}} + J_{\mathrm{GB}} + J_{\mathrm{M}} \end{cases} \tag{7.16}$$

Since the total moments of inertia are equal and also the two motors, the two local controller will be the same. Therefore, only one will be developed in the following.

As said at the beginning of this Chapter about the decentralized control, it considers only an approximated model of the joint. This model includes the mechanical equation of the joint at the motor side and the electrical equations describing the behaviour of the equivalent electric circuit of a brushless DC motor that is shown in Figure 7.1. The mechanical and electrical equations are listed in (7.17). The

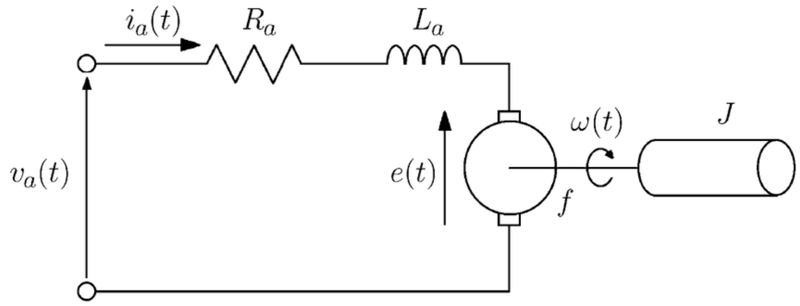

Figure 7.1: Equivalent electric circuit of a brushless DC motor [14].

first equation is the joint mechanical one at the motor side. As it can be seen, the disturbance torque τ_d appears at the motor side divided by the gearbox ratio n. This shows the gearbox positive effect of reducing the impact of non linear and coupling terms on the robot behaviour. The second equation relates proportionally the motor torque τ_m to the armature current I_a. The third equation shows the proportional dependency between the back electromotive force E and the motor angular speed $\dot{\phi}$. The fourth and last equation is the electrical armature one. The total friction coefficient at the motor side β_t is null since the friction was not considered.The required motor parameters values are extracted from its data sheet and are listed in Table 7.1.

$$\begin{cases} J_{\mathrm{t}} \cdot \ddot{\phi}' + \beta_{\mathrm{t}} \cdot \dot{\phi}' + \frac{\tau_d}{n} = \tau_m \\ \tau_m = K_{\mathrm{m}} \cdot I_a \\ E = K_w \cdot \dot{\phi} \\ V_a - R_a \cdot I_a - L_a \cdot \frac{dI_a}{dt} - E \end{cases} \tag{7.17}$$

Table 7.1: Motors parameters

Parameters	Symbol	Unit measure	Value
equivalent terminal resistance	R_a	Ω	0.055
equivalent terminal inductance	L_a	mH	0.150
torque constant	K_m	$(N \cdot m)/A$	0.1156
speed constant	K_w	$V/(rad/s)$	0.095

Moving from the time domain to the Laplace domain, the transfer function (7.18) that links the motor shaft angular velocity $\dot{\phi}$ to the motor armature voltage V_a can be found, where τ_{arm} is the armature time constant and τ_{mec} is the mechanical time constant. The two time constants are computed as in (7.19) and are equal to $\tau_{\text{mec}} = 4ms$ and $\tau_{\text{arm}} = 2.73ms$.

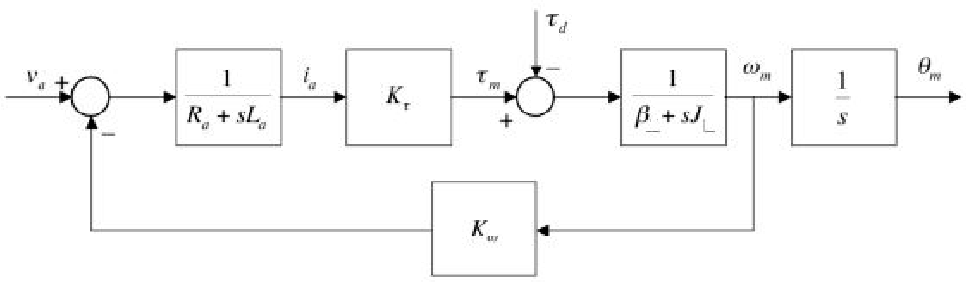

Figure 7.2: DC motor diagram in open loop [15].

$$\frac{\dot{\phi}}{V_a} = \frac{\frac{1}{K_w}}{1 + \tau_{\text{mec}} \cdot s + \tau_{\text{mec}} \cdot \tau_{\text{arm}} \cdot s^2} \tag{7.18}$$

$$\begin{cases} \tau_{\text{mec}} = \frac{J_t \cdot R_a}{K_w \cdot K_m} \\ \tau_{\text{arm}} = \frac{L_a}{R_a} \end{cases} \tag{7.19}$$

The decentralized control architecture of the industrial manipulators is usually a nested control loop. The most general configuration shown in Figure 7.3 includes one loop for the position, one loop for the velocity and the last loop for the torque. The torque loop has to be much faster than the other two and it is used to cancel the mechanical pole of the motor transfer function in order to increase the motor bandwidth and to control the motor directly with the current. The use of the torque loop requires a current sensor that allows to know the motor torque τ_m just multiplying the measured current for the torque constant K_m. Position and velocity loops require an encoder on the motor shaft to measure the motor shaft position and velocity. For an industrial manipulator the position loop can be very

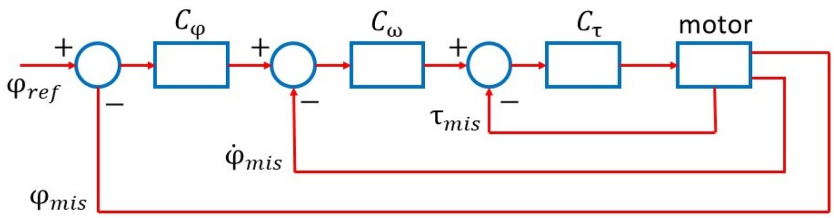

Figure 7.3: General control scheme with nested loops.

important at each joint, since the position accuracy at each joint results into a better accuracy of the end effector position. In Agilino robot, the position loop is useless since motors just have to rotate the robot driving wheels. About the torque loop, it is not necessary since the output of the velocity loop controller can be the armature voltage V_a. If the centralized control architecture would have been used, the current loop should have been introduced since the output of the controller is a torque. Therefore, the torque loop is needed to translate the control torque into the motor armature voltage V_a. Finally, only the velocity loop will be used. The velocity loop controller receives the error between the reference angular speed and the measured one and returns the armature voltage to drive the motor. In order to develop this controller, the loop shaping design technique is used and studied in [16]. This technique allows to work directly on the loop transfer function $L(s)$, instead of dealing with the complete transfer function $W(s)$.

7.3 Control requirements

The controller design considers both the steady state and transients requirements, assuring the system stability. Starting with the steady state requirements:

- The steady state error of a step reference must be zero.
- The steady state error of a ramp reference $r(t) = R_0 \cdot t$, having the constant acceleration equal to $R_0 = -250\ rad/s^2$, has to be lower than $\bar{e} = 1\ rad/s$. Ramp references occur every time the robot trajectory changes, therefore the error must be small since the trajectory variation can be related to emergency situations. The chosen acceleration/deceleration correspond to a quite fast brake. Supposing that the robot is moving straight, the two motors angular speeds are equal $\dot{\phi}_{\mathrm{mR}} = \dot{\phi}_{\mathrm{mL}} = \dot{\phi}_{\mathrm{m}}$. If the robot has to brake with a deceleration of $\dot{v} = -1m/s$, this results into a motor shaft angular deceleration of $\ddot{\phi}_m = -250\ rad/s^2$.

$$v = \frac{v_R + v_L}{2} = \frac{R \cdot (\dot{\phi}_R + \dot{\phi}_L)}{2} = \frac{R \cdot (\dot{\phi}_{\mathrm{mR}} + \dot{\phi}_{\mathrm{mL}})}{2 \cdot n} = \frac{R \cdot \dot{\phi}_{\mathrm{m}}}{n} \tag{7.20}$$

$$\dot{\phi}_{\mathrm{m}} = \frac{v \cdot n}{R} \quad \Rightarrow \quad \ddot{\phi}_m = \frac{\dot{v} \cdot n}{R} = \frac{-1(m/s^2) \cdot 25}{0.1(m)} = -250\frac{rad}{s^2} \tag{7.21}$$

The step reference requirement allows to fix the system type, that is the number of poles the loop function $L(s)$ has in the origin. It is equal to $\nu + p$, where ν is the number of poles the controller has in the origin while p the one of the plant. The ramp reference requirement allows to fix the controller steady state gain K_{cw}. To respect the step reference requirement, the system type has to be equal to $\nu+p = 1$. Since the motor transfer function has $p = 0$, the controller transfer function must have $\nu = 1$. To respect the ramp reference requirement, the controller steady state gain has to be greater than the value below, where the plant steady state gain is equal to $K_{\mathrm{pw}} = 1/K_w$.

$$\bar{e} \leq \frac{R_0}{K_{\mathrm{pw}} \cdot K_{\mathrm{cw}}} \rightarrow K_{\mathrm{cw}} \geq \frac{R_0}{\bar{e} \cdot K_{\mathrm{pw}}} = \frac{R_0 \cdot K_w}{\bar{e}} = \frac{250 \cdot 0.095}{1} = 23.75 \tag{7.22}$$

Moving to transients requirements, they are expressed in time domain. The maximum overshoot is fixed small and equal to $\hat{s} = 1\%$, so that the motor shaft angular speed never exceeds the reference value. Indeed, it is better to have a slower but safer controller with no overshoot. Then, the maximum rise time t_r and settling time $t_{\mathrm{s2\%}}$ must be chosen taking into account the following two parameters.

- The sampling period T_s, that mostly depends on the hardware limitations, is fixed equal to $T_s = 50\ ms$. Therefore, the corresponding sampling frequency is $\omega_s = 2\pi/T_s = 125.7\ rad/s$.
- A suitable number of samples N for the description of the transient phase, whose duration is the settling time. It is fixed equal to $N = 10$.

Therefore, the settling time is chosen equal to $t_{\mathrm{s2\%}} = T_s \cdot N = 500\ ms$ and the rise time to $t_r = 0.2s$.

$$\begin{cases} \hat{s} \leq 1\% \\ t_r \leq 0.2s \\ t_{\mathrm{s2\%}} \leq 0.5s \end{cases} \tag{7.23}$$

Supposing that the complementary sensitivity function $T(s) = L(s)/(1 + L(s))$ is a second order prototype transfer function as in (7.24), the transient requirements can be translated from time domain to frequency domain with the relations (7.25).

$$T(s) = \frac{1}{1 + \frac{2\cdot\zeta}{\omega_n} \cdot s + \frac{s^2}{\omega_n^2}} \tag{7.24}$$

$$\begin{cases} \zeta \geq \frac{|\ln(\hat{s})|}{\sqrt{\pi^2+\ln^2(\hat{s})}} \\ \omega_{\mathrm{nr}} \geq \frac{\pi-\arccos(\zeta)}{t_r\cdot\sqrt{1-\zeta^2}} \\ \omega_{\mathrm{ns}} \geq -\frac{\ln(\alpha)}{t_s\cdot\zeta} \\ \omega_n \geq \max(\omega_{\mathrm{nr}}, \omega_{\mathrm{ns}}) \end{cases} \Rightarrow \begin{cases} \zeta \geq 0.82 \\ \omega_{\mathrm{nr}} \geq 22.56 rad/s \\ \omega_{\mathrm{ns}} \geq 9.47 rad/s \\ \omega_n \geq 22.56 rad/s \end{cases} \tag{7.25}$$

Then, the requirements are related to the resonance peaks of the sensitivity function S_p and of the complementary sensitivity function T_p and to the crossover frequency ω_c of the loop function $L(s)$, using relations (7.26). The values of the resonance peaks T_p and S_p can be used to draw on the Nichols plane the corresponding constant magnitude loci that act as constraints that the frequency response of the loop function $L(s)$ must not violate to assure robust stability.

$$\begin{cases} T_p \leq \frac{1}{2\cdot\zeta\cdot\sqrt{1-\zeta^2}} \\ S_p \leq \frac{2\cdot\zeta\cdot\sqrt{2+4\cdot\zeta^2+2\cdot\sqrt{1+8\cdot\zeta^2}}}{\sqrt{1+8\cdot\zeta^2}+4\cdot\zeta^2-1} \\ \omega_c \geq \omega_n\cdot\sqrt{\sqrt{1+4\cdot\zeta^4}-2\cdot\zeta^2} \end{cases} \Rightarrow \begin{cases} T_p \leq 1.074 = 0.62dB \\ S_p \leq 1.2117 = 1.668dB \\ \omega_c \geq 12.9rad/s \end{cases} \tag{7.26}$$

The final passage in order to design the controller with the loop shaping design is to translate the requirements of S_p and T_p into the ones of phase (PM) and gain (GM) margins, using the following formulas.

$$\begin{cases} GM_S \geq \frac{S_p}{S_p-1} \\ PM_S \geq 2\cdot\arcsin\left(\frac{1}{2\cdot S_p}\right) \\ GM_T \geq 1+\frac{1}{T_p} \\ PM_T \geq 2\cdot\arcsin\left(\frac{1}{2\cdot T_p}\right) \end{cases} \Rightarrow \begin{cases} GM_S \geq 5.72 = 15.15dB \\ PM_S \geq 48.74° \\ GM_T \geq 1.93 = 5.72dB \\ PM_T \geq 55.49° \end{cases} \tag{7.27}$$

$$\begin{cases} GM \geq \max(GM_S, GM_T) \\ PM \geq \max(PM_S, PM_T) \end{cases} \Rightarrow \begin{cases} GM \geq 5.72 = 15.15dB \\ PM \geq 55.49° \\ \omega_c \geq 12.9rad/s \end{cases} \tag{7.28}$$

The sampling frequency $\omega_s = 125.7\ rad/s$ is greater than twice the required crossover frequency $\omega_c = 12.9\ rad/s$, therefore the Shannon sampling theorem is respected and the rise time requirements is acceptable.

7.4 Control development

The loop function $L(s)$ is plotted on the Nyquist graph with the T_p and S_p constant magnitude loci in order to check in first approximation the transients requirements fulfilment. The loop function $L(s)$ is the product of the controller transfer function G_{cw} with the motor transfer function G_w. In the next steps, the evolution of the controller design is analysed. The controllers are checked in the situation the robot starts moving straight with a constant longitudinal acceleration of $\dot{v} = 1\ m/s^2$ that results into a linear increase of the longitudinal velocity v starting from zero. When v reaches the value of 0.5 m/s, the acceleration goes to zero and the robot keeps moving at constant longitudinal velocity. This longitudinal velocity ramp results into a ramp of each motor shaft angular speed with constant angular acceleration equal to $\ddot{\phi}_m = 250 \ rad/s^2$, that is exactly the one considered in the steady state requirements definition. The simulations are performed exploiting three programs:

- Adams allows to build a robot model that takes care of the robot mechanical description. It can be exported in Simulink.
- Simscape allows to realize intuitively the equivalent electric circuits of the two brushless DC motors.
- Simulink allows to build the controller feedback structure and to implement the controller algorithms.

The Agilino Adams model takes care of the robot mechanical description, where also the rotational inertia moments of the motors and gearboxes around their axes are included. Their values are moved from the motor side to the wheel side and assigned to Adams parts. The rotational inertia moment of each couple made of one motor and one gearbox is approximated with a cylinder block that is integral to the corresponding wheel and has its longitudinal axis coincident with the wheel main axis. This cylinder mass is fixed almost null, since the motor and gearbox masses have already been considered with the point mass approximation. The Adams model, exported in Simulink, receives the torques that result from the difference brought at the wheel side (multiplied by the gearbox ratio n) between the total motors torques proportional to the armature currents and the friction torques. The friction torque is modelled in Simulink while the total torque is obtained multiplying the motor speed constant for the current measured in the Simscape motor equivalent electric circuit. The electric circuit was built exploiting four Simscape blocks:

- One resistor,
- One inductor, and
- Two driven voltage sources. The first one refers to the armature voltage and is driven by the armature voltage value V_a coming out of the controller. The second one refers to the back electromotive force and is driven by the back EMF value E computed multiplying the motor speed constant for the motor shaft angular speed. The latter is computed dividing the wheel angular speed measured in the Adams model by the gearbox ratio n.

Steps of the controller design:

1. The controller transfer function that comes out of the steady state requirements is G_{cw1}, that has one pole in the origin and the steady state gain at least equal to $K_{\mathrm{cw}} = 23.75$. The system is too fast as it can be seen in Figure 7.4b, where the system response to a unitary step is investigated. The system must be slow down due to the hardware limitations and the overshoot requirement. The crossover frequency is equal to $\omega_c = 181 \ rad/s$, while the hardware limitations require a value around $\omega_c = 12.9 \ rad/s$. The overshoot

requirement requires an almost null value, while this controller limits it at $\hat{s} = 51.7\%$. Moreover, the loop function frequency response violates the relative margin constraints, as shown in the Nichols plot of Figure 7.4a. To solve these problems, lag compensation terms must be introduced.

$$G_{\text{cw1}} = \frac{K_{\text{cw}}}{s} = \frac{23.75}{s} \tag{7.29}$$

Table 7.2: First controller results

Parameters	Symbol	Values
overshoot	$\hat{s}$	51.7%
rise time	t_r	0.009 s
settling time	$t_{s2\%}$	0.122 s
sensitivity function resonance peak	S_p	8.54 dB
complementary function resonance peak	T_p	6.86 dB
crossover frequency	ω_c	181 rad/s
gain margin	GM	7.8 dB
phase margin	PM	27.5 deg

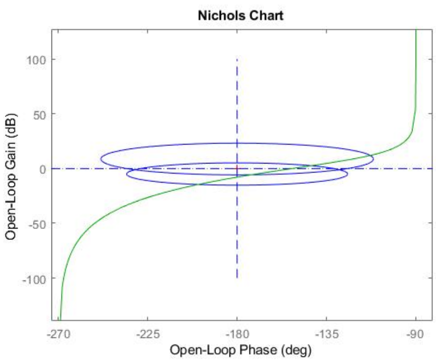

(a) *Nichols plot of the loop function.*

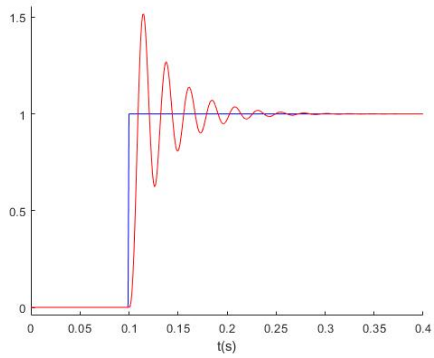

(b) *System response to a step reference. The blue line is the angular speed reference and the red one the measured motor angular speed, both expressed in rad/s.*

Figure 7.4: First controller attempt

2. To slow down the system, two lag functions R_{a1} and R_{a2} are added to the previous controller. The crossover frequency reduces to $\omega_c = 15.6$ rad/s (Figure 7.5b), that is coherent with the hardware limitations and results into a negligible overshoot of $\hat{s} = 0.02\%$ (Figure 7.6a). On the other hand, the

lower crossover frequency makes the system slow in recovering the error when a ramp reference is applied (Figure 7.7a), even though the controller steady state gain is set high enough to get a small ramp error. The loop function frequency response respects the relative stability constrains fixed by the resonance peaks of the sensitivity and complementary functions (Figure 7.5a). The step and ramp tests are performed simulating the controller with the simplified mathematical model described previously. Therefore, the controller validation with the Adams model must be done (Figures 7.8a, 7.8b and 7.8c).

$$G_{\mathrm{cw2}} = \frac{K_{\mathrm{cw}}}{s} \cdot R_{\mathrm{a1}} \cdot R_{\mathrm{a2}} = \frac{23.75}{s} \cdot \frac{1+\frac{s}{0.004}}{1+\frac{s}{0.001}} \cdot \frac{1+\frac{s}{0.0004}}{1+\frac{s}{0.0001}} \tag{7.30}$$

Table 7.3: Second controller results

Parameters	Symbol	Values
overshoot	$\hat{s}$	0.02%
rise time	t_r	0.511 s
settling time	$t_{\mathrm{s2\%}}$	0.237 s
sensitivity function resonance peak	S_p	0.71 dB
complementary function resonance peak	T_p	0.0018 dB
crossover frequency	ω_c	15.6 rad/s
gain margin	GM	31.9 dB
phase margin	PM	83.9 deg

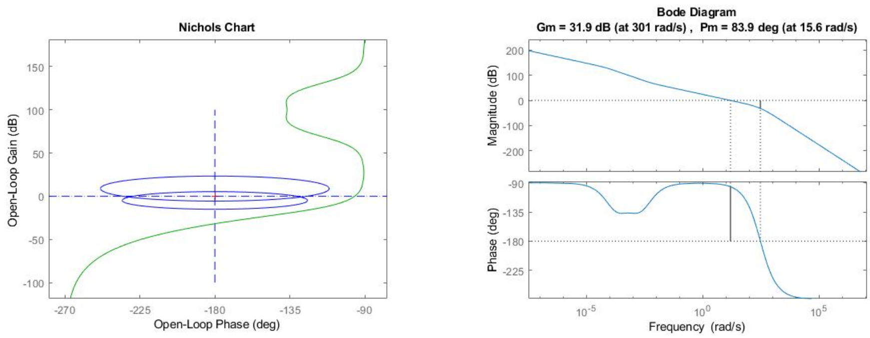

(a) *Nichols plot of the loop function.* (b) *Bode plots of the loop function.*

Figure 7.5: Second controller loop function frequency analysis.

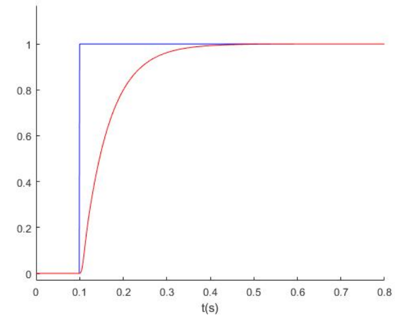

(a) *System step response. Blue reference speed and red measured motor angular speed expressed in rad/s.*

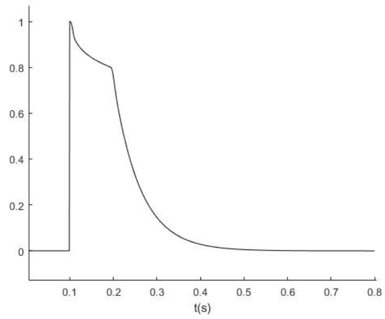

(b) *Error between reference and measured speeds in rad/s.*

Figure 7.6: Second controller step analysis.

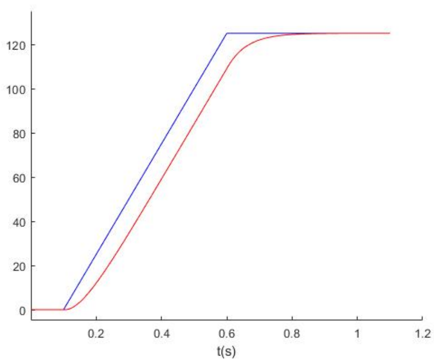

(a) *System ramp response. Blue reference speed and red measured motor angular speed expressed in rad/s.*

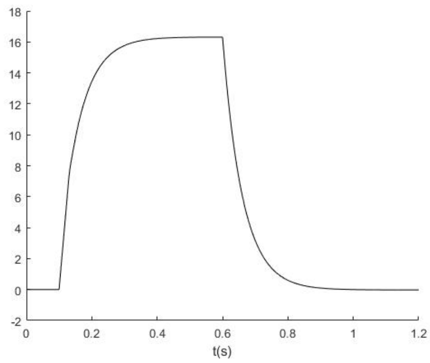

(b) *Error between reference and measured speeds in rad/s.*

Figure 7.7: Second controller ramp analysis.

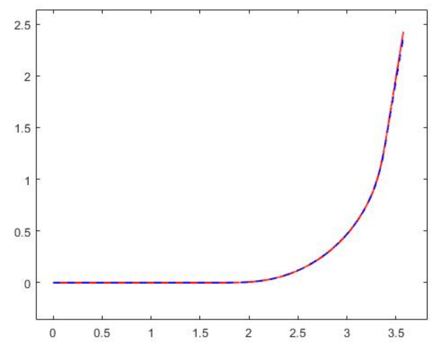

(a) *Trajectories comparison. The blue line refers to the reference trajectory and the red one to the real trajectory. The axes unit measure is meter m.*

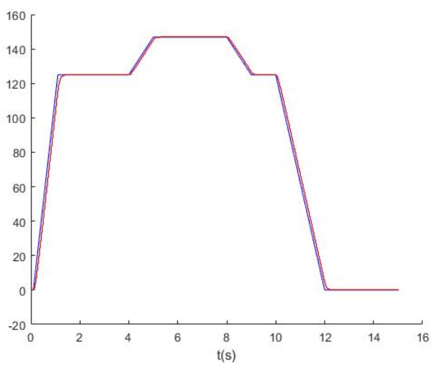

(b) *System response with the Adams model. Blue reference speed and red measured motor angular speed expressed in rad/s.*

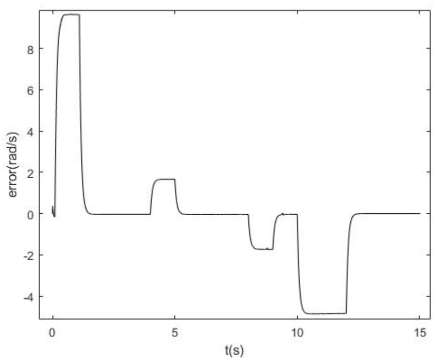

(c) *Error between reference and measured speeds in rad/s.*

Figure 7.8: Second controller tested with the Adams model exported in Simulink.

Chapter 8

Conclusions and Future works

8.1 Conclusions

This thesis work investigates the instruments for wheeled mobile robot simulations and control. In particular, it focuses on the differential drive robots category. The first researched instrument is a multi body programme that allows to build easily a robot model exploiting the CAD files coming from the mechanical design. The chosen programme is Adams. The second instrument refers to the dynamic modelling techniques that can be used in order to write the equations that describe the robot behaviour. The chosen technique is the Newton-Euler approach. Two mathematical models have been found: the first one for simulation purposes, while the second one for control strategies development. The first mathematical model is validated with respect to the Adams model, while the second model results from the first one by striking dynamical aspects that have been considered negligible for control purposes. Therefore, the Adams model was fundamental to provide a first validation of the mathematical model when the robot prototype was still not ready. While, the second mathematical model allowed to investigate the control strategies that could be used in order to control the robot motors.

The first mathematical model and the developed control strategy are the instruments that allow the control engineer to guarantee the safe autonomous motion of the robot.

1. First, thanks to the mathematical model, the engineer can compute offline safe trajectories of the robot in different motion situations. Indeed, the robot can move on its own or with a loaded truck both on a horizontal or inclined plane. From the safe trajectories study, the engineer can find the robot longitudinal and angular velocities and accelerations limits in order to keep the robot on safe trajectories. In this way, the high level controller, that elaborates the robot trajectories, will never provide to the low level ones, that pilot the

motors, trajectories out of these bounds.

2. Second, thanks to the developed control algorithm, the control engineer assures that the motors will follow the desired trajectories and will be able to deal with unpredictable situations, such as a sudden reduction of the friction coefficient at the wheels-ground contact points.

The first mathematical model can support also the design work of the mechanical engineer.

1. First, the mathematical model can help the mechanical engineer choosing the robot mass centre position and its mass value. Indeed, these two choices cannot be done without considering the possible trajectories the robot will follow, the possible loads it will pull and the possible inclined planes it will move on. Indeed, in order to guarantee the robot safe motion, two main aspects have to be considered.
   (a) The normal force at each driving wheel contact point must be greater than a minimum value to assure that neither longitudinal slip nor lateral slide occur during the robot normal working conditions.
   (b) The wheels supposed to be in contact with the ground must always be in contact with the ground. This is an issue of three wheels differential drive robots that have two driving wheels and only one castor wheel either in the front or in the back.

   Knowing in first approximation where the robot mass centre should be and the value the robot mass should have, the mechanical engineer decides the displacement of the robot parts and the eventual addition of concentrated masses whose unique goal is to increase the robot mass and move the mass centre taking up a small volume.
2. Second, the mathematical model provides to the mechanical engineer the torques values that motors should deliver in desired working conditions. Therefore, this helps the engineer during the choice of motors and eventually of gearboxes.
3. Third, the mathematical model provides to the mechanical engineer the force and torque values that the robot exchanges with the truck it is pulling. This information can be helpful for the choice of the docking structure between them. For example, a squared rod that from the robot goes up and enters the corresponding squared hole in the truck can be inappropriate to transmit the torque, since it could require a huge section not to brake after few fatigue cycles.
4. Fourth, the mathematical model helps the mechanical engineer choosing the distance that castor wheels should have from the driving wheels axis. Indeed, the goal of a compact robot requires a reduced distance, while the robot task of pulling heavy trucks requires the opposite. A trade off must be reached.

The distance reduction increases the weight transfer from the driving wheels to the rear castor wheel during the acceleration phases. The same occurs during the deceleration phases, but with the weight transfer to the front castor wheel. In both cases, the normal reaction forces at the driving wheels reduces, limiting the available traction force before slip occurs.

5. The robot model together with the truck model helps the mechanical engineer during the truck mechanical design. Indeed, the truck dimensions define where the load it carries can be placed, therefore the possible distance of the loaded truck mass centre from the robot logic centre. This distance deeply influence the trajectories the robot with the truck will be able to follow safely. In particular, the distance component on the robot longitudinal axis is the arm of the loaded library centrifugal force that appears when the system is performing a turn. The resulting moment deeply influences the robot motion.

Summarizing, the mathematical model can be used in two of the three steps of the robot design procedure.

1. First step. Engineers must define the robot working conditions including the possible trajectories the robot will follow, the possible loads it will pull and the possible inclined planes it will move on. Therefore, an estimate of the robot maximum velocities, accelerations, loads and inclined plane angles must be done.
2. Second step. Mechanical engineers design the robot starting from the limits defined in step one. As explained before, they can exploit the mathematical model to discover in first approximation both the mass centre position, the total mass value and the wheels displacement.
3. Third step. Control engineers upload the mathematical model, studying the mechanical design and computing the mass and inertia values required by the model. From the uploaded model, the real and final limits of velocities, accelerations, loads and inclined plane angles can be found. They should be similar to the first estimations but some differences can be present due to the mechanical design. When the limits have been defined, control engineers develop a controller to pilot the motors and deal with unpredictable working situations.

This thesis work can be set in the third step, since the robot mechanical design was ready and the goal of simulating and controlling the robot motion was required.

The idea of using the normal forces at the driving wheels to study the robot safe trajectories limits come from the automotive world. Of course, the robot velocities and accelerations are much smaller than the ones characterizing a car motion. Indeed, here is the difference. The need of studying robot safe trajectories does not come from its velocities and accelerations but from the fact that it will pull trucks whose weight can be five-six times the robot weight.

8.2 Future works

Future works are related to the part of the thesis on the motor controller. Indeed, two main simplifications have been done in the controller design:

1. The first one is related to the system whose motion is controlled by the motors control algorithms. In this thesis, the robot moving on its own is considered. In future works, the robot that is pulling a loaded truck could be investigated. The track is integral to the robot due to the docking structures exploited. Therefore, the dynamic model of the robot with the library and of the robot on its own are equal from a mathematical point of view since both systems can be schematized with just one body moving on a plane. The planar motion assumption allows to reduce the body description to three parameters that are the body mass, the vertical inertia and the mass centre position. Of course, these three parameters values change from one system to the other. It's straightforward that both the total mass and vertical inertia of the robot with a loaded truck are greater than the ones of the robot on its own. From a control point of view, the most important aspect is the mass centre position with respect to the line perpendicular to the ground and passing through the robot logic centre. Indeed, as it can be seen in the mathematical model equations, the non linear effects due to Coriolis and Centrifugal forces are linearly proportional to x_m and y_m, that are its distance components on the robot longitudinal axis and on the robot transversal axis, respectively. In addition, also the coupling effects expressed by the non-diagonal elements of the inertia matrix are proportional to this distance. In order to reduce these disturbance torques, the mass centre should be placed ideally on the vertical logic centre line. The robot on its own has the mass centre close to the line, since this was the mechanical design goal to have the highest normal forces at the wheel-ground contact points. The reduction of non linear and coupling effects due to the mass centre position and due to the gearbox presence between each motor and the corresponding wheel allows to choose a decentralized control strategy that is the one implemented in this thesis. When the robot is moving a loaded track that is four times its weight and that has its mass centre outside the robot footprint depending on the truck length, the total mass centre moves to the back of the logic centre vertical line. This enhances the non linear and coupling effects that could become relevant, with the gearbox no more able to make them negligible. The control strategy developed in this thesis could be checked with this system to understand its limits. Starting from this limits, new control strategies could be investigated in the centralized architecture group. Indeed, if non linear effects become no more negligible also with the gearbox presence, the attempt of cancelling them with compensation terms could be taken into account. Of course this strategy introduces complexity since the controller

must receive at least two pieces of information. The first one is relative to the connection or not of the truck to the robot. The second one refers to the weight of the truck load. This would require a scale on the truck base where materials are placed and continuously weighted. This solution seams to be not economically convenient, therefore other control strategy could be investigated. They should be robust enough to deal with non linear and coupling effects treated as non modelled disturbances. Another way to limit these disturbances keeping using the decentralized control strategy could be implemented by placing the truck above the robot so that its mass centre is on the robot vertical logic centre line.

2. The second simplification refers to the motors angular references that have been used to design the controller. The steady state requirements have been chosen considering step and ramp references. The system type is fixed equal to one to have zero steady state error when the angular speed reference is constant. Instead, the steady state gain of the controller is chosen so that the steady state error is lower than a fixed value when ramp references are used. Therefore, this thesis work assumes that ramp references are used to drive electric motors even though they are not. Indeed, a ramp reference stresses a lot the motors that must provide a constant acceleration for the whole ramp duration. To change the angular speed, profiles with greater degrees are used. A common one is the third degree shown in Figure 8.1a. The corresponding acceleration and jerk profiles are shown respectively in Figure 8.1b and Figure 8.1c. The velocity profile shows the transition from a lower velocity value to a higher one. The corresponding acceleration is zero both at the beginning and at the end of the transition, passing through a maximum value. This profile is one of the real profiles used since it is less stressful for the motors. For such a profile, maybe a different controller could be used. Of course, before improving the controller, the thesis controller could be checked with the order 3 velocity profile.

3. Another future work could be the development of the high level controller that plans and continuously updates the trajectories the robot has to follow to reach the target. For the trajectory planning, it takes into account the robot position in space, the position of the target the robot has to reach, the positions of the obstacles that laser scanners continuously detect and the safe trajectories boundaries that have been computed offline.

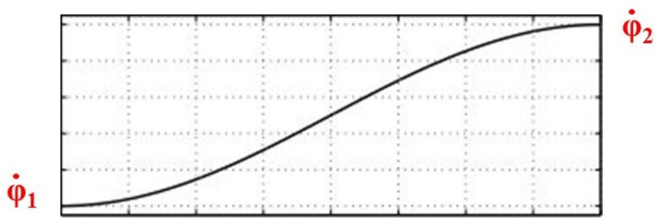

(a) *Velocity profile.*

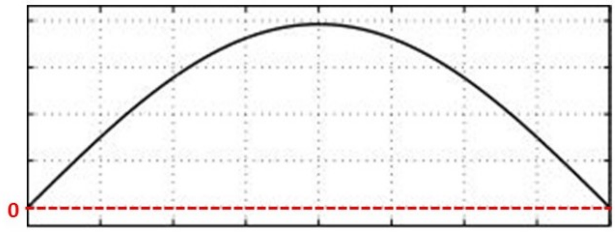

(b) *Acceleration profile.*

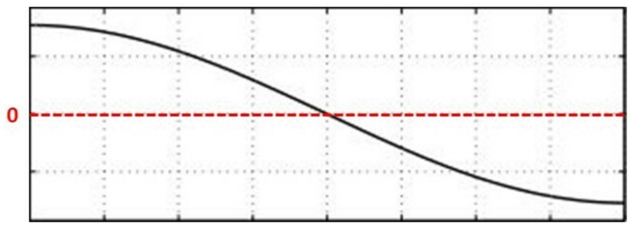

(c) *Jerk profile.*

Figure 8.1: Third degree velocity profile and its derivatives

Appendix A

Table A.1: Robot reference frames list

R_0	Absolute reference frame on the ground.
R_a	Reference frame with the origin in the robot logic centre, the x axis on the robot longitudinal direction and the y axis on the driving wheels main axis.
R_b	Reference frame with the origin in the centre of mass of the robot base and the axes parallel to the ones of R_a.
R_m	Reference frame with the origin in the centre of mass of the upper volume and the axes parallel to R_a.
R_1	Reference frame with the origin in the left wheel centre and axes parallel to R_a.
R_2	Reference frame with the origin in the right wheel centre and axes parallel to R_a.
R_3	Reference frame with the origin in the point where the castor wheel connects to the robot base and axes parallel to R_a.
R_L	Reference frame with the origin in the point where the robot is in contact with the eventual library or truck it is pulling. It is the tip of the robot rod in charge of connecting it to the library or truck. The axes are parallel to R_a.

Table A.2: Forces exchanged among the robot parts and external forces acting on the robot

$f_{\mathbf{tm}}^{\mathbf{Ra}}$	$= [f_{\mathrm{tmx}}, f_{\mathrm{tmy}}, f_{\mathrm{tmz}}]$ is the force applied by the upper volume to the robot base.
$\tau_{\mathbf{tm}}^{\mathbf{Ra}}$	$= [0{,}0, \tau_{\mathrm{tmz}}]$ is the torque applied by the upper volume to the robot base.
$f_{\mathbf{t1}}^{\mathbf{Ra}}$	$= [f_{\mathrm{t1x}}, f_{\mathrm{t1y}}, f_{\mathrm{t1z}}]$ is the force applied by the left wheel to the robot base.
$\tau_{\mathbf{t1}}^{\mathbf{Ra}}$	$= [\tau_{\mathrm{t1x}}, \tau_{\mathrm{t1y}}, \tau_{\mathrm{t1z}}]$ is the torque applied by the left wheel to the robot base.
$f_{\mathbf{c1}}^{\mathbf{Ra}}$	$= [f_{\mathrm{c1x}}, f_{\mathrm{c1y}}, f_{\mathrm{c1z}}]$ is the force applied to the left wheel from the ground at the contact point.
$\tau_{\mathbf{c1}}^{\mathbf{Ra}}$	$= [0{,}0, \tau_{\mathrm{c1z}}]$ is the torque applied to the left wheel from the ground. τ_{c1z} is the vertical friction torque at the contact point.
$\tau_{\mathbf{b1y}}^{\mathbf{Ra}}$	$= [0, \tau_{\mathrm{b1y}}, 0]$ is the friction torque at the left wheel horizontal bearings.
$f_{\mathbf{t2}}^{\mathbf{Ra}}$	$= [f_{\mathrm{t2x}}, f_{\mathrm{t2y}}, f_{\mathrm{t2z}}]$ is the force applied by the right wheel to the robot base.
$\tau_{\mathbf{t2}}^{\mathbf{Ra}}$	$= [\tau_{\mathrm{t2x}}, \tau_{\mathrm{t2y}}, \tau_{\mathrm{t2z}}]$ is the torque applied by the right wheel to the robot base.
$f_{\mathbf{c2}}^{\mathbf{Ra}}$	$= [f_{\mathrm{c2x}}, f_{\mathrm{c2y}}, f_{\mathrm{c2z}}]$ is the force applied to the right wheel from the ground at the contact point.
$\tau_{\mathbf{c2}}^{\mathbf{Ra}}$	$= [0{,}0, \tau_{\mathrm{c2z}}]$ is the torque applied to the right wheel from the ground. τ_{c2z} is the vertical friction torque at the contact point.
$\tau_{\mathbf{b2y}}^{\mathbf{Ra}}$	$= [0, \tau_{\mathrm{b2y}}, 0]$ is the friction torque at the right wheel horizontal bearings.
$f_{\mathbf{tL}}^{\mathbf{Ra}}$	$= [f_{\mathrm{tLx}}, f_{\mathrm{tLy}}, 0]$ is the force applied by a library or a truck the robot is pulling to the robot base.
$\tau_{\mathbf{tL}}^{\mathbf{Ra}}$	$= [0{,}0, \tau_{\mathrm{tLz}}]$ is the torque applied by a library or a truck to the robot base.
$f_{\mathbf{t3}}^{\mathbf{Ra}}$	$= [0{,}0, f_{\mathrm{t3z}}]$ is the force applied by the castor wheel to the robot base.

Table A.3: Robot equations

$$
\begin{cases}
m_b * (\dot{v} - d * \omega^2) = f_{\text{t1x}} + f_{\text{t2x}} + f_{\text{tLx}} + f_{\text{tmx}} + g_1 * m_b \\
m_b * (v * \omega + d * \dot{\omega}) = f_{\text{t1y}} + f_{\text{t2y}} + f_{\text{tLy}} + f_{\text{tmy}} + g_2 * m_b \\
f_{\text{t1z}} + f_{\text{t2z}} + f_{\text{t3z}} + f_{\text{tmz}} + g_3 * m_b = 0 \\
\tau_{\text{t1x}} + \tau_{\text{t2x}} + b_1 * f_{\text{t1z}} - b_1 * f_{\text{t2z}} - h_b * f_{\text{t1y}} - h_b * f_{\text{t2y}} + y_m * f_{\text{tmz}} + \\
-z_L * f_{\text{tLy}} - z_m * f_{\text{tmy}} = 0 \\
-R * f_{\text{c1x}} - R * f_{\text{c2x}} + L_1 * f_{\text{t3z}} + d * f_{\text{t1z}} + d * f_{\text{t2z}} + h_b * f_{\text{t1x}} + h_b * f_{\text{t2x}} + \\
-x_m * f_{\text{tmz}} + z_L * f_{\text{tLx}} + z_m * f_{\text{tmx}} = 0 \\
I_{\text{bzz}} * \dot{w} = \tau_{\text{t1z}} + \tau_{\text{t2z}} + \tau_{\text{tLz}} + \tau_{\text{tmz}} - b_1 * f_{\text{t1x}} + b_1 * f_{\text{t2x}} - d * f_{\text{t1y}} + \\
-d * f_{\text{t2y}} + x_L * f_{\text{tLy}} + x_m * f_{\text{tmy}} - y_L * f_{\text{tLx}} - y_m * f_{\text{tmx}} \\
m_w * (\dot{v} - b_1 * \dot{\omega}) = f_{\text{c1x}} - f_{\text{t1x}} + g_1 * m_w \\
m_w * (v * \omega - b_1 * \omega^2) = f_{\text{c1y}} - f_{\text{t1y}} + g_2 * m_w \\
f_{\text{c1z}} - f_{\text{t1z}} + g_3 * m_w = 0 \\
-I_{\text{wyy}} * \omega * \dot{\theta}_1 = R * f_{\text{c1y}} - \tau_{\text{t1x}} \\
\{(J_{\text{mot}} + J_{\text{rid}}) * n^2 + I_{\text{wyy}}\} * \ddot{\theta}_1 = -\tau_{\text{a1y}} - \tau_{\text{t1y}} - R * f_{\text{c1x}} \\
I_{\text{wxx}} * \dot{\omega} = -\tau_{\text{c1z}} - \tau_{\text{t1z}} \\
m_w * (\dot{v} + b1 * \dot{\omega}) = f_{\text{c2x}} - f_{\text{t2x}} + g_1 * m_w \\
m_w * (v * \omega + b_1 * \omega^2) = f_{\text{c2y}} - f_{\text{t2y}} + g_2 * m_w \\
f_{\text{c2z}} - f_{\text{t2z}} + g_3 * m_w = 0 \\
-I_{\text{wyy}} * \omega * \dot{\theta}_2 = R * f_{\text{c2y}} - \tau_{\text{t2x}} \\
\{(J_{\text{mot}} + J_{\text{rid}}) * n^2 + I_{\text{wyy}}\} * \ddot{\theta}_2 = -\tau_{\text{a2y}} - \tau_{\text{t2y}} - R * f_{\text{c2x}} \\
I_{\text{wxx}} * \dot{\omega} = -\tau_{\text{c2z}} - \tau_{\text{t2z}} \\
M_m * (\dot{v} - y_m * \dot{w} - d * \omega^2 - x_m * \omega^2) = M_m * g_1 - f_{\text{tmx}} \\
M_m * (v * \omega - y_m * \omega^2 + d * \dot{\omega} + x_m * \dot{w}) = M_m * g_2 - f_{\text{tmy}} \\
M_m * g_3 - f_{\text{tmz}} = 0 \\
I_{\text{mzz}} * \dot{\omega} = -\tau_{\text{tmz}} \\
f_{\text{c1y}} - f_{\text{c2y}} = 0
\end{cases}
$$

Table A.4: Transformation matrix

$$R_a^0 = \begin{bmatrix} \cos(\theta) & -\sin(\theta) & 0 \\ \sin(\theta) & \cos(\theta) & 0 \\ 0 & 0 & 1 \end{bmatrix} \tag{A.1}$$

$$t_b^a = \begin{bmatrix} d \\ 0 \\ -h_b \end{bmatrix} \quad t_m^b = \begin{bmatrix} x_m \\ y_m \\ z_m \end{bmatrix} \quad t_L^b = \begin{bmatrix} x_L \\ y_L \\ z_L \end{bmatrix} \tag{A.2}$$

$$t_1^a = \begin{bmatrix} 0 \\ b \\ 0 \end{bmatrix} \quad t_2^a = \begin{bmatrix} 0 \\ -b \\ 0 \end{bmatrix} \quad t_3^b = \begin{bmatrix} L \\ 0 \\ h_3 \end{bmatrix} \tag{A.3}$$

$$R_b^a = R_m^b = R_L^b = R_1^a = R_2^a = R_3^b = \begin{bmatrix} 1 & 0 & 0 \\ 0 & 1 & 0 \\ 0 & 0 & 1 \end{bmatrix} \tag{A.4}$$

Table A.5: Masses and inertia moments values used in the equations

Quantity	Symbol	Unit measure	Value
upper volume mass	M_m	Kg	57.9
upper volume vertical inertia moment	I_{mzz}	$Kg * m^2$	3.78
robot base mass	m_b	Kg	5.72
robot base vertical inertia moment	I_{bzz}	$Kg * m^2$	0.338
wheel mass	m_w	Kg	0.8
wheel radial inertia moment	I_{wxx}	$Kg * m^2$	0.004
wheel axial inertia moment	I_{wyy}	$Kg * m^2$	0.0022

Table A.6: Robot geometric parameters values

Symbol	Unit measure	Value
d	m	0.0
b_1	m	0.25
L_1	m	0.2275
x_m	m	0.012
y_m	m	-0.007
z_m	m	0.123
$h_a = R$	m	0.1
h_b	m	0.053
z_L	m	0.4

Bibliography

[1] www.pitsco.com/TETRIX-Omni-Wheel-Packs

[2] robu.in/product/100mm-aluminium-mecanum-wheels-bush-type-rollers-left/

[3] www.indiamart.com/proddetail/castor-wheel-17093681473.html

[4] Campion G., Bastin G., D'Andrea-Novel B. *Structural properties and classification of kinematic and dynamic models of wheeled mobile robots*, in "*IEEE Transactions on Robotics and Automation*", vol. 12, n. 1, pages 47-62, 1996.

[5] Kelly A. *A Vector Algebra Formulation of Kinematics of Wheeled Mobile Robots*, in *Robotics Institute Technical Report CMU-RI-TR-10–33*, 2010.

[6] grabcad.com/library/robot-omni-3-wheel-1

[7] MT200S Omni wheel Robot Car

[8] Qian J.,Zi B., Wang D., Ma Y., Zhang D. *The design and development of an omni-directional mobile robot oriented to an intelligent manufacturing system*, in "*Sensors*", vol. 17, n. 9, pages 2073, 2017.

[9] Matteucci M. *Mobile robots kinematics*, slides, Politecnico di Milano.

[10] MSC Software Corporation *Adams Tutorial Kit for Mechanical Engineering Courses*, Third Edition.

[11] Dhaouadi R., Hatab A. A. *Dynamic Modelling of Differential-Drive Mobile Robots using Lagrange and Newton-Euler Methodologies: A Unified Framework*, in "*Advances in Robotics* & *Automation*", vol. 2, n. 2, pages 1-7, 2013.

[12] Genta G., Morello L., *The Automotive Chassis*, Volume 1, chapter *Wheels and Tires*, 2009.

[13] Bona B., *Slides of the Robotic course at Mechatronic Engineering - Politecnico di Torino.*

[14] Basilio J. C., Moreira M. V. *State–Space Parameter Identification in a Second Control Laboratory*, in "*IEEE Transactions on Education*", vol. 47, n. 2, pages 204-210, 2004.

[15] Pesce S. *Simulation and advanced control of a professional manipulator*, thesis, Politecnico di Torino, 2018.

[16] Cerone V., *Slides of the Modern Design of Control Systems course at Mechatronic Engineering - Politecnico di Torino.*

[17] Muir P.F. *Modelling and control of wheeled mobile robots*, Carnegie mellon university, 1988.

[18] Eka Maulana, M. Aziz Muslim, Akhmad Zainuri. *Inverse Kinematics of a Two-Wheeled Differential Drive and Autonomous Mobile Robot*, in "*Electrical Power, Electronics, Communicatons, Control and Informatics Seminar (EEC-CIS)*, pages 93-98, 2014.